MAX-PLANCK-INSTITUT FÜR POLYMERFORSCHUNG

JOHANNES GUTENBERG UNIVERSITÄT MAINZ

Intracellular Self-Assembly of Platinum-based Nanofibers

A Thesis submitted in partial Fulfilment of
the Requirements for the degree of

Master of Science

in the Faculty 09 – Chemistry, Pharmacy,
Geography and Geosciences

of the Johannes Gutenberg-Universität Mainz
by

Julian Link

Subject of Study: Biomedical Chemistry

1st Reviewer: Prof. Dr. Tanja Weil

2nd Reviewer: Prof. Dr. Pol Besenius

Mainz, 2022

This Thesis was written between August 2020 and March 2021 at the Max-Planck-Institute for Polymer Research under the supervision of Prof. Dr. Tanja Weil. Further Review was contributed by Prof. Dr. Pol Besenius.

I, Julian Link, Matriculation Number 2733742

hereby declare, that I have composed my master's thesis independently on my own and without any other resources than the ones indicated. All statements that are taken literally or analogously from different sources I indicated as such.

Mainz, 10.03.2022
(Place, Date)

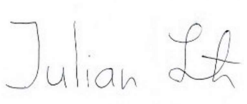

(Julian Link)

Acknowledgements

First and foremost, I would like to thank Prof. Dr. Tanja Weil for taking the time of meeting and discussing my research interests before the start of this project and in general for the opportunity to do my master's thesis in her research group.

Furthermore, I would like to thank Prof. Dr. Pol Besenius for providing further review of the thesis.

I would also like to express my great thanks to my group leader Dr. David Ng for conveying this topic to me and for always having an open door (quite literally) to discuss anything.

My special thanks to Dr. Zhixuan Zhou, who introduced me to platinum-based peptide chemistry and has consistently provided me with advice and support. I have rarely met a person who always expresses such a cheerful and optimistic atmosphere. It has been a pleasure to work with you and I am looking forward to continuing this later this year.

Moreover, I want to thank Sarah Chagri for helping me a lot with the disulfide based isopeptide chemistry that will also be partially reported in her Ph.D. thesis. Yong Ren kindly provided additional help for the synthesis of the coumarin derivative. These findings may also be partially reported within his Ph.D. thesis.

I also would like to say thank you to the members of AK Weil for the warm welcome, the fruitful discussions and in summary for the friendly environment. Among others, I would like to mention by name Konrad Maxeiner, Patrick Roth and Raphael Meyer and thank them for all the conversations of scientific and private context and for integrating me into the group in an amicable way (although they made me feed the piggy bank for my bad jokes a lot).

Lastly, I want to thank my friends and family for always having my back and supporting me even when I had little time for them in the past months.

Abbreviations

AIE	aggregation-induced emission
DCM	dichloromethane
DIC	diisopropylcarbodiimide
DIPEA	diisopropylethylamine
DMF	*N,N*-dimethylformamide
DMF-DMA	*N,N'*-dimethylformamide dimethyl acetal
DNA	deoxyribunucleic acid
Fmoc	9-fluorenylmethoxycarbonyl
GDP	guanosine diphosphate
GTP	guanosine triphosphate
ISA	isoleucine-serine-alanine
KFN	lysine-phenylalanine-asparagine
LLCT	ligand-to-ligand charge-transfer
MLCT	metal-to-ligand charge-transfer
MMLCT	metal-metal-to-ligand charge-transfer
mRNA	messenger ribonucleic acid
NIR	near-infrared
on	over night
OSU	oxy-succinimid
PPG	photoprotecting group
PyBop	(benzotriazol-1-yloxy)tripyrrolidinophosphonium hexafluorophosphate
RNA	ribonucleic acid
ROS	reactive oxygen species
rt	room temperature
SHA	salicylhydroxamate
SPPS	solid-phase peptide synthesis
TAT	transactivator of transcription
TEM	transmission electron microscopy
TFA	trifluoroacetic acid
TIPS	triisopropylsilane
tpy	terpyridine

Table of Contents

List of Figures and Schemes

Figures

Schemes

Abstract

Kurzfassung

Intrazelluläre Selbstassemblierung stellt einen zentralen Prozess in der Natur und eine Inspiration für die synthetische supramolekulare Chemie dar. Um die komplexe Dynamik der Selbstassemblierung kontrollieren zu können, ist die Implementierung stimulusabhängiger chemischer Gruppen in das molekulare Design der Monomereinheiten weitgehend unabdingbar. Darüber hinaus verspricht die Verwendung von Aminosäuren, und damit von Peptiden, als Untereinheiten eine gute Biokompatibilität im Hinblick auf Anwendungsgebiete in der synthetischen Biologie und der Nanomedizin. In dieser Arbeit wurden daher peptidbasierte Systeme, die auf äußere Reize (z.B. Licht) oder auf körpereigenes Glutathion reagieren, hergestellt und auf ihre Selbstassemblierung hin untersucht. Zusätzlich wurde ein NIR-emittierender Platin(II)-Terpyridin-Komplex an die Peptidsequenz gekoppelt, um sowohl Fluoreszenz als auch kooperative Effekte bei der Assemblierung zu erzielen. Mit Hilfe der Konfokalmikroskopie konnte die Aufnahme des Metallo-Peptids in Zellen in ersten Zellstudien nachgewiesen werden. Diese Ergebnisse verdeutlichen die vielfältigen Möglichkeiten, die der Einsatz solcher platinbasierten Peptidkonjugate im Hinblick auf die intrazelluläre supramolekulare Chemie bietet.

Abstract

Intracellular self-assemblies are pivotal processes in nature and has been an inspiration for synthetic supramolecular chemistry. To provide control over the complex dynamics of self-assembly, the implementation of stimulus-responsive chemical groups in the molecular design of monomer units is largely mandatory. Additionally, the use of amino acids, and thus peptides, as subunits promises good biocompatibility with respect to areas of application in synthetic biology and nanomedicine. In this work, therefore, peptide-based systems responding to external stimuli (e.g. light) or to endogenous glutathione were prepared and analyzed with respect to their self-assembly. Additionally, an NIR emitting platinum (II) terpyridine complex was conjugated to the peptide sequence to provide both fluorescence and cooperative effects towards the assembly. Aided by confocal microscopy, uptake of the metallo-peptide into cells was proven in first cell studies. These results illustrate the multitude of possibilities offered by using such platinum-based peptide conjugates with respect to intracellular supramolecular chemistry.

1 Introduction

Self-assembly describes the spontaneous organization of smaller building blocks into structures without human intervention and is widespread in nature and technology.[1] On a molecular scale, usually non-covalent, reversible interactions provide the base of the self-assembly process as the components must remain unchanged during the progress. Furthermore, the individual units themselves often exhibit directionality, ultimately leading towards a well-defined structure in thermodynamic equilibrium.[2,3] This thermodynamic consideration discloses the main difference between the terms self-assembly and self-organization, which implies a non-equilibrium process accompanied by energy dissipation. Additionally, the monomer building blocks for self-organization often lack the directionality for structure formation.

For the most part, self-assembly and self-organization operate on different spatiotemporal scales, but together they generate complex architectures. For instance, self-assembly of tubulin represents an energy-independent process, whereas disassembly requires energy from the hydrolysis of guanosine triphosphate (GTP).[4] In general, the dovetailing of these two concepts becomes especially clear when looking at natural examples. Therefore, in the following sections the biological background of self-assembly is clarified with suitable examples. Subsequently, synthetic approaches towards generating assemblies and controlling their kinetics are presented.

1.1 Self-Assembly in Nature

Self-assembly is essential for life. Therefore, nature offers a variety of highly complex nanostructures generated by dynamic self-assembly. Ranging from nucleic acids and proteins, micelles and membranes to viruses, a highly precise organization derived from the molecular interactions is observed.[5]

Starting with one of the simplest yet probably most pivotal monomeric units: the pairing of nucleotides. Four different nucleobases, attached to deoxyribose and a phosphate group, align into a polymeric backbone with an alternating phosphate-sugar sequence. Complementary pairs of nucleobases from two antiparallel DNA (deoxyribonucleic acid) strands then assemble into a double helix structure, mainly held together by hydrogen bonding and π-π-interactions (Figure 1B).[6]

Beyond the central dogma of molecular biology, the focus falls on proteins and their manifold structures. While the primary structure is just a linear polymer constructed by covalent peptide bonds between the 20 proteinogenic amino acids, the secondary, tertiary, and quaternary structure is predetermined by precise self-assembly processes. α-helices and β-sheets represent the typical secondary motifs. They are stabilized by intramolecular hydrogen bonds between carbonyl oxygen atoms and amide groups four residues away (α-helix), respectively, between several β-strands. The individual stacking of the secondary structures into domains is driven by hydrogen bonding, hydrophobic and ionic interactions, and bears function to the polypeptide. Lastly, the assembly of multiple subunits results in the quaternary structure and ultimately, the final, thermodynamically stable[7] protein (Figure 1A). The association of proteins into functional aggregates is also a widespread theme in biology. From the tetrameric structure of hemoglobin[8] or cluster formation of heat shock proteins[9], to highly complex assemblies like the ribosome[10] or the pyruvate dehydrogenase[11].

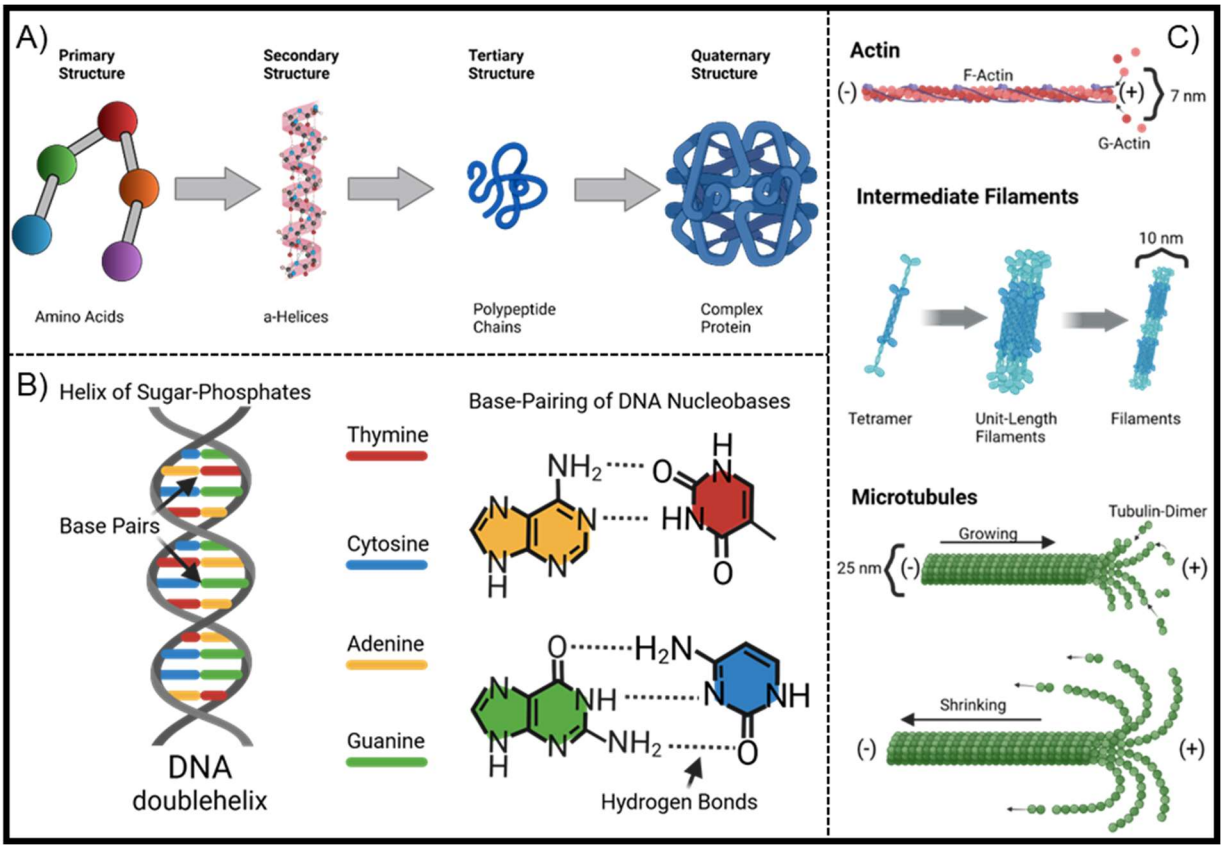

Figure 1: Overview of natural self-assemblies. A) Peptide structure from primary to quaternary structure (adapted from[12]), B) Nucleobases, DNA-double helix and ribonucleic acid (RNA)-strand (adapted from[13]), C) Different Fibers of the eukaryotic cytoskeleton. Created with Biorender.com.

Moving from peptides and nucleotides to lipids, the most compelling example is the self-assembly of phospholipids to bilayers that create confined spaces (the cell, membranous organelles) isolated from the external environment. The individual phospholipids are arranged in a conserved pattern so that the polar (glycerol/phosphate) head group of the molecules forms the outermost and innermost segment of the membrane, while the nonpolar (fatty acid) segments face the inside of the bilayer.[5] The further incorporation of cholesterols, glycolipids, and membrane proteins turns the cell membrane into a dynamic environment that is yet to be understood completely.

Further stabilization of the eukaryotic cell is provided by the cytoskeleton, namely the actin and intermediary filaments, as well as microtubule. They compose a highly dynamic network of interlinking structures that express a multitude of functions, ranging from mechanical resistance over cell signaling to cellular division.[11] The different types of filaments differ in their relative size but share conserved features: they consist of monomeric building blocks that can self-assemble non-covalently into fibrous formations and disassemble upon intrinsic stimuli (Figure 1C).[4]

A closer look at the microtubule reveals that these fibers consist of two different monomeric building blocks: α- and β-tubulin. In their dormant form, they do not self-assemble. Only after α-tubulin binds to a GTP molecule, they build stable heterodimers that now display a polarity ((+) and (–)-End) and assemble into fibrous networks. They grow towards the (+)-end, where a GTP cap prevents the hydrolysis of GTP to guanosine diphosphate (GDP). When this GTP cap is hydrolyzed, the so-called catastrophe causes rapid shrinkage of the microtubule. This process of rapid growth and hydrolysis is highly dynamic and influenced by a multitude of auxiliary proteins that support either of the processes. With the help of these proteins, as well as with the regulation of the GTP concentration the cell can organize the structure formation with high precision.[11]

1.2 Synthetic Self-Assembly

Inspired by the aforementioned naturally occurring structures, research towards integrating self-assembling nanostructures in a biological environment gained great importance in supramolecular chemistry, as these systems generate opportunities for both nanomedicine and synthetic biology.[14] In general, the desired biological application requires the fulfillment of certain criteria like biocompatibility, responsiveness to the specific environment, and the ability to self-assemble within crowded, complex settings.[14] For this purpose, four material classes are commonly used: peptides, polyaromatic compounds, polymers and metal nanoparticles (Figure 2). Particularly, polyaromatic and peptide-based materials are scrutinized regarding their potential therapeutic or diagnostic application.[14] The former compounds show interesting photochemical properties as the π-π-stacking-induced aggregation of the aromatic cores facilitates the emergence of light emission. This phenomenon is the subject of ongoing discussion[15] and widely purported as aggregation-induced emission[16] (AIE). Possible applications include tumor imaging agents[17] and drugs for photodynamic therapy[18].

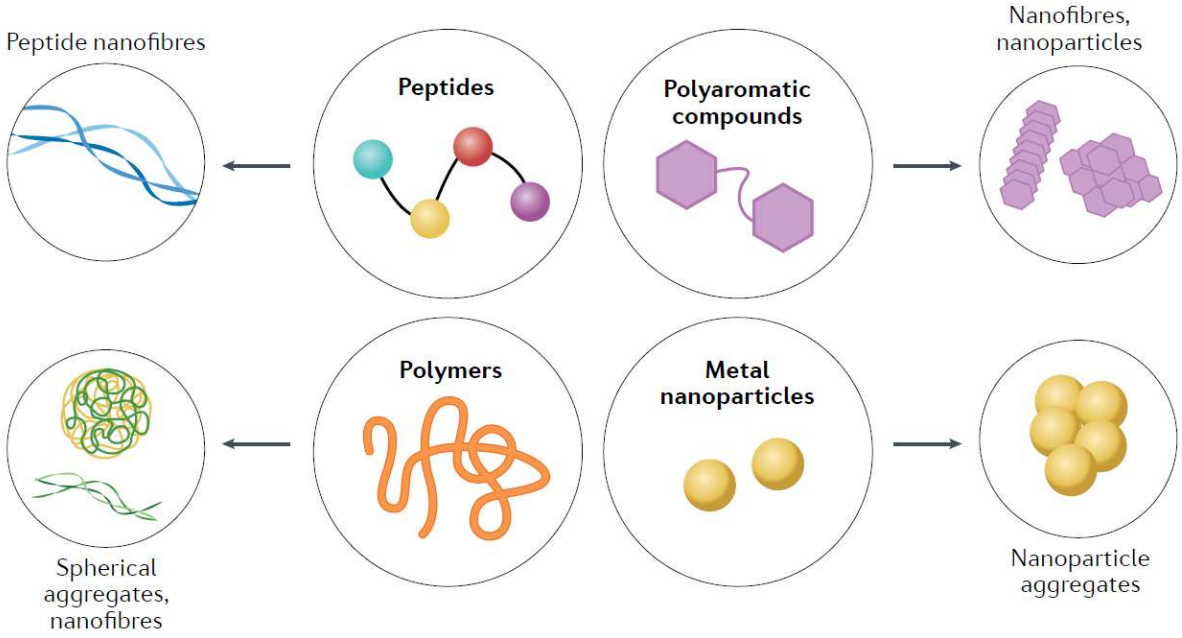

Figure 2: Material classes for intracellular self-assembly. Taken from[14].

Application wise, bottom-up synthesis approaches of supramolecular assembly inside cells could not only help investigating the foundation of cellular processes but also expand the portfolio of therapeutic applications.[19] Small molecule drugs usually face limitations regarding drug resistance and pharmacokinetics.[20] Systems capable of

intracellular self-assembly however can be tailored towards cancer cell specificity or improved pharmacokinetics due to accumulation at the target site.[21] The mechanical stress that results from the self-assembly can ultimately lead to cell death.

To achieve this medicinal use, the assembly-precursors must include a bioresponsive chemical group that interacts with the specific microenvironment in order to solely operate at the target site. These stimuli-responsive triggers include intrinsic stimuli like pH[22,23], redox-environment[24–26], or enzyme activity[27] as well as extrinsic counterparts like light[28] to ultimately achieve spatiotemporal control of the intracellular self-assembly.

Beyond the π-π stacking, peptides display intermolecular hydrogen bonding to promote self-assembly. In addition to that, the commonly utilized building blocks are the 20 proteinogenic amino acids, and therefore these systems often exhibit great biocompatibility. When amphiphilicity is introduced in the design of the molecules, an alternating pattern of polar and nonpolar side chains on the peptide backbone supports this assembly propensity even further. These β-sheet forming sequences are inspired by the naturally occurring amyloid structures that are linked to neurodegenerative diseases like Alzheimer's and Parkinson.[29] The implementation of aromatic side chains or additionally attached fluorophores can further enhance this tendency of self-assembly.

1.3 Stimuli-Responsive-Assembly

In general, there are three categories of molecular design concepts for bioresponsive self-assembly (Figure 3):

a) Structures going through purely morphological transformations
b) Pro-assembling monomers that become active upon cleavage of a hydrophilic group
c) Precursors undergoing a multistep reaction cascade after bioresponsive deprotection

The former category includes fewer examples like *cis-trans*-isomerization of double bonds or protonation caused by pH change.[30] The most common strategy for intracellular assembly is the removal of a hydrophilic subunit to decrease the solubility of the remaining fragment and therefore promote self-assembly. Category c) describes the more sophisticated systems as the interaction with the surrounding environment causes both the cleavage and reorganization of the precursor. The advantage of this complex mechanism is the higher specificity and temporal control towards self-assembly.

Oftentimes these trigger systems are tailored to distinct cellular environments. The most prominent example is the tuning towards cancer cell specificity. Even though different cancer cells show varying biochemical behavior, there are common characteristics among these highly proliferative cells: the tumor's extracellular surroundings show a decrease in pH because of the enhanced glycolytic rate, a maladjusted redox environment due to elevated levels of glutathione[31] and reactive oxygen species[32] (ROS) respectively, or the overexpression of certain proteases that can control the bioavailability of angiogenic activators and inhibitors[33], among others.

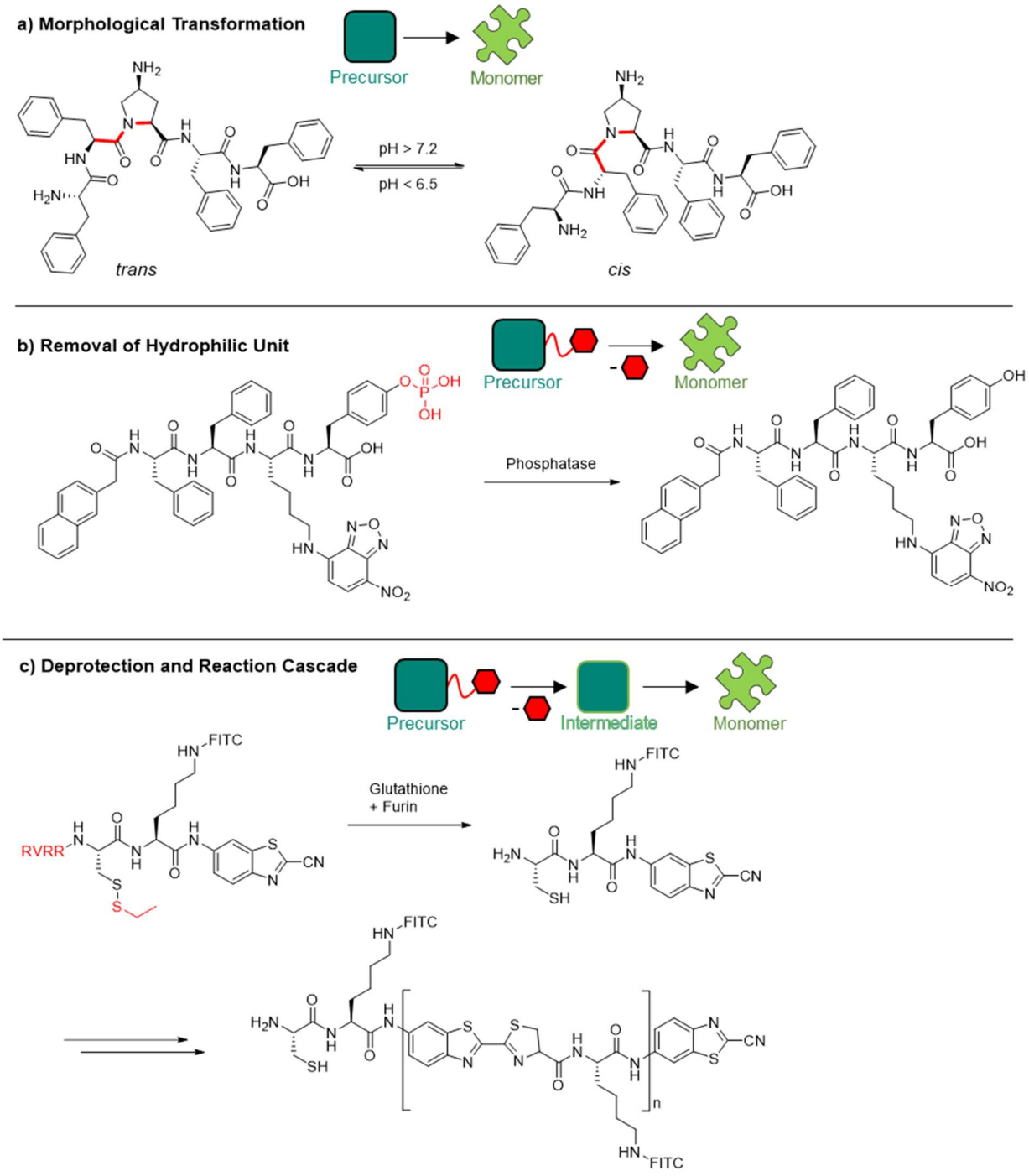

Figure 3: Differences in complexity of the chemical transformation for intracellular self-assembly. a) Morphology transformation due to trans/cis-amide isomerization. b) Removal of hydrophilic group in a phosphotyrosine containing peptide. c) Deprotection of a bioresponsive cyclization precursor and following reaction cascade, FITC = fluorescein isothiocyanate. Adapted from[14].

In the following subchapters, the stimuli-responsive systems are further discussed individually. From the extrinsic approach of photoprotecting groups (PPGs) up to pH- and redox-responsive systems that exploit the tumor microenvironment, interesting examples are showcased.

1.3.1 Photochemistry

The sheer complexity of highly dynamic networks in chemistry and biology demands an external control element that can be addressed without interfering with the system itself. As such, light displays an appealing option for an external trigger that can be delivered with high spatiotemporal precision and control in a non-invasive way.[34] In general, two molecular approaches have been reported for the light-directed control of chemical and biological systems. The first one is based on photoisomerization resulting in a change of the molecular structure and the corresponding chemical or biological effect. The foundation of visual perception serves as a prominent example of this method. The initiating step of phototransduction is the isomerization of 11-*cis*-retinal to all-*trans*-retinal, which then activates Rhodopsin *via* several intermediate steps.[4] The latter strategy is the caging of a functional group with a photoprotecting group (PPG). This approach enables a multitude of possibilities as researchers can literally switch on functionalities.

The requirements for wavelength-selective cleaving groups are a distinct and narrow absorption maximum, high quantum yield, and suppressed intra- and intermolecular energy transfer. With the introduction of PPGs that display a bathochromic shift to their maximum absorbance, external control of biological processes with non-toxic and deep-tissue-penetrating visible light are feasible.[35]

In the context of self-assembly, the caging group can provide steric hindrance to impede intermolecular interactions. For instance, introducing a PPG to an antisense agent inactivates the hybridization with messenger ribonucleic acid (mRNA). Upon irradiation, this interaction is facilitated again, which results in the blocking of translation and therefore controlled gene silencing.[36] Besides the demand for lower energy light in the visible spectrum, PPGs for biological applications require the byproduct of the uncaging to be biologically inactive. A class of molecules that display such biocompatibility are coumarin derivatives. Depending on their substitution pattern, their absorption maximum varies from ca. 300–500 nm (compare Figure 4). Replacing the carbonyl oxygen in the coumarin core with a sulfur atom increases the polarizability resulting in a bathochromic shift towards visible blue light (470–500 nm).[37]

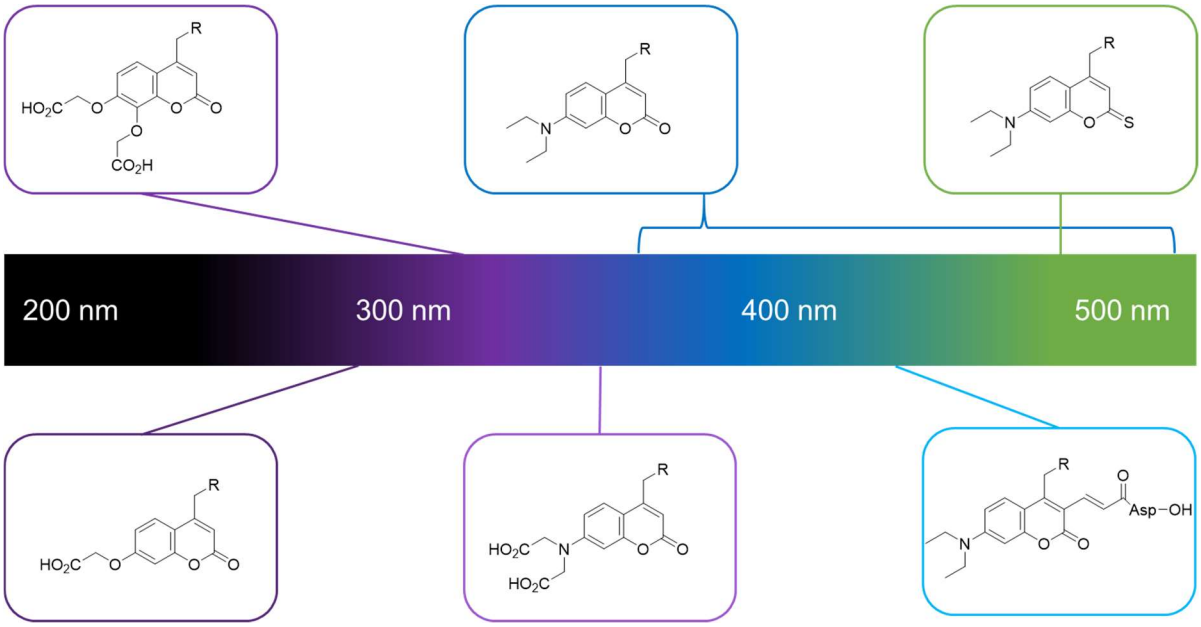

Figure 4: Coumarin derivatives used as photoprotective groups and their corresponding absorption maximum. Adapted from[34].

Schwalbe *et al*. utilized this thio-coumarin in combination with an orthogonal *ortho*-nitrophenylalanine in a Two-PPGs-One-Molecule strategy to construct a photoprotected puromycin derivative that can be first activated and later deactivated by irradiation with different wavelengths of light.[38] Their data exemplifies the facile caging and subsequent uncaging of an amine group with the coumarin. Upon irradiation with light suitable for biological application (470 nm), they detect the formation of CO_2 release from the carbamate linker with IR experiments within a few minutes.[38]

1.3.2 pH

The pH value inside living cells is fundamental to their function and survival. Under physiological conditions, the cytosol displays a pH of 7.2, while organelles in the endocytic pathway show a gradient from 6.3 in early endosomes to 4.7 in lysosomes.[39] The gradient acidic environment in these vesicles enables activation of proteases, uncoupling of ligands from receptors, and even the directed transport in the endocytic subcompartments. This knowledge, in combination with the acidification of the extracellular matrix of tumor cells, can be utilized to design pH-responsive sequences that only self-assemble in an acidic environment. Suitable candidates for this controlled pH-driven assembly are peptides, as some amino acid side chains are susceptible to protonation or deprotonation within the bioavailable pH ranges. As such, a block co-polypeptide consisting of a hydrophilic polyarginine part and an amphiphilic FKFE segment changes its morphology upon endocytosis. Glutamic acid (E) residues are protonated in the acidified environment of late endosomes, which decreases the hydrophilicity of the peptide leading to aggregation into distinct structures inside of the cell.[40] In addition to the implementation of ionizable groups, structural elements prone to pH-induced isomerization can also facilitate the controlled formation of intracellular assemblies. For instance, a pentapeptide with a central 4-amino-proline isomerizes pH-dependent from *cis*- to *trans*-amide resulting in a change from β-sheet dominated helices at neutral pH to random-coil nanoparticles at slightly acidic pH (Figure 3a).[41]

1.3.3 Redox Environment

Glutathione

A key player in the redox environment of cells is the tripeptide glutathione (GSH). It is the most abundant non-protein peptide in eukaryotes and is synthesized from the three amino acids glutamate (E), cysteine (C), and glycine (G). The glutamate is attached to the CG dipeptide *via* a γ-peptide linkage. GSH has multiple crucial physiological roles, highlighted by its high concentration of 1–10 mM in mammalian cells in comparison to the 1000 times lower concentration outside the cells.[31] Because of its nucleophilic thiol residue, it is important for detoxification as it reacts with pollutants, drug metabolites or heavy metals. Furthermore, glutathione is the major cellular antioxidant ensuring redox homeostasis by reacting with ROS or lipid peroxides.[42] Many cancer types display elevated GSH concentrations, what correlates with multidrug resistance due to

glutathionylation and therefore inactivation of chemotherapeutics.[43] Therefore, GSH represents an attractive intrinsic stimulus for controlled intracellular self-assembly.

By the reduction and subsequent cleavage of a disulfide bond, a hydrophilic unit can be removed from a precursor molecule resulting in a self-assembling sequence. Wang and coworkers developed a disulfide bridged cyanine-pyrene with an inert optical property that is cleaved by GSH, whereby the free bispyrene can self-assemble into fluorescent *J*-aggregates.[17] This technique can be used for tumor imaging *in vivo*.

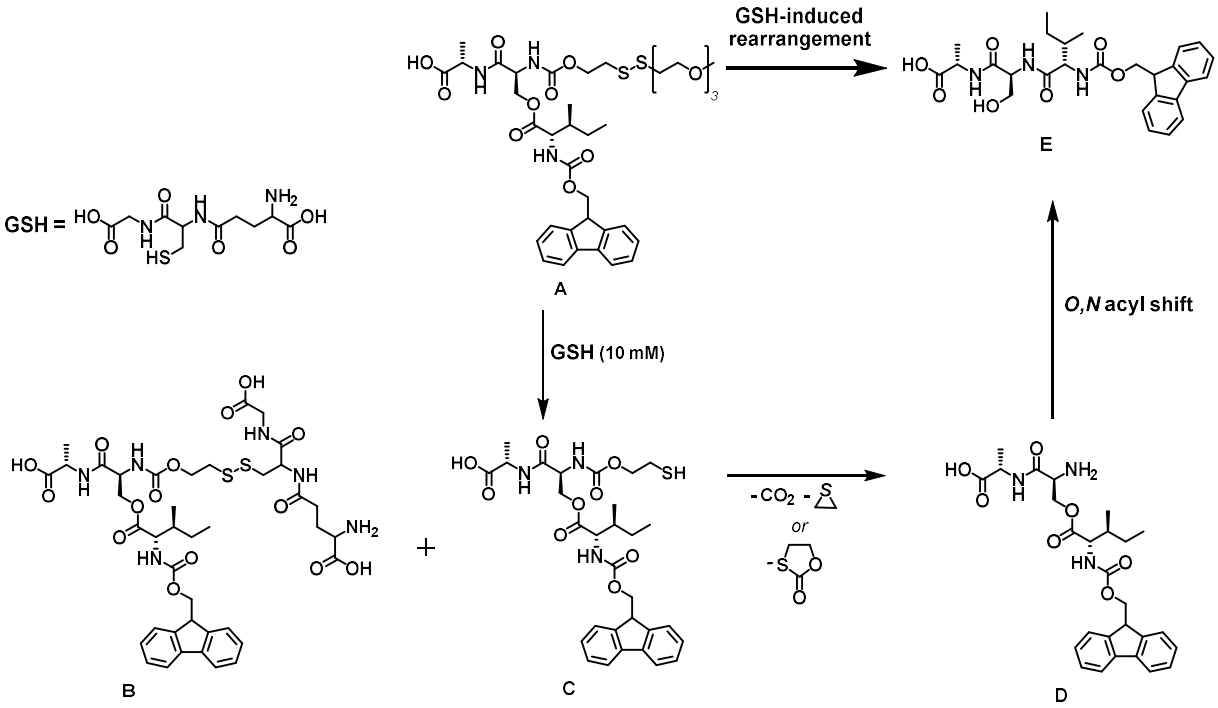

Scheme 1: GSH-mediated disulfide oxidation and subsequent *O,N*-acyl shift of an disulfide containing isopeptide. First, the starting material A reacts with GSH resulting in the intermediates B and C. Subsequent self-immolation of the linker leads to the formation of D that then rearranges into the linear sequence E.[44]

Other interesting precursor candidates for the bottom-up design of GSH-responsive compounds are isopeptides. The amino acids of these peptides are connected *via* one or more amide or ester functions in the side chain, in addition to the polyamide backbone. As a result, isopeptides display a “kink” in their molecular structure, which prevents aggregation and the formation of supramolecular structures. The stimulus-responsive deprotection of the amino group next to the adjacent ester bond causes the peptide to undergo a rearrangement reaction (*O,N*-acyl shift) resulting in a linear sequence that can self-assemble into nanostructures. With the coupling of such an isopeptide to a cell-penetrating sequence, intracellular self-assembly can be achieved in a controlled pre-programmed way. For instance, the 9-fluorenylmethoxycarbonyl

(Fmoc)-protected tripeptide isoleucine-serine-alanine (ISA) readily assembles to fibers in an aqueous solution, whereas the isopeptide with isoleucine coupled to serine *via* an ester bond, does not show this behavior. By linking this isopeptide to the cell-penetrating peptide TAT (trans-activator of transcription) using a disulfide linker, cellular uptake followed by a multi-step transformation is achieved. First, GSH reduces the disulfide bond to the free thiol of the linker. Nucleophilic attack of this thiol on the carbamate carbon or on an adjacent methylene unit then induces the self-immolation of the linker, leaving the *N*-terminus of the serine unprotected. Subsequent *O*,*N*-acyl shift results in the linearization and self-assembly of the tripeptide motif (Scheme 1).[44]

ROS

Reactive oxygen species are produced in the conventional metabolism of the mitochondria and can be further enhanced as a response to cytokines and growth factors. They play an important role in the regulation of eukaryotic signal transduction.[45] Despite the beneficial aspects, ROS, and their overproduction is linked to oxidative stress and diseases like cancer.[32] Using the elevated concentration of ROS in cancer cells for drug targeting is a relatively new approach in nanomedicine. Phenyl boronic acids are an example of ROS-responsive functionality. They can be oxidized by hydrogen peroxide (H_2O_2) at physiological pH to produce phenol and borate. This redox-sensitivity bears the possibility of controlled self-assembly. The Weil and Ng group presented an elegant example by combining ROS- and pH-responsiveness in a peptide-based phenyl boronic acid precursor (Figure 5).[24] Here, the boronic acid group functions as both the ROS-sensitive cage for the amino group of an esterified serine, and as an anchor for the attachment of a cell-penetrating peptide *via* an acid-labile dynamic covalent bond.

The TAT sequence mediates the cellular uptake in the endocytic pathway. The acidic pH within the intracellular vesicles releases the pro-assembling motif. Upon reaction with cytosolic hydrogen peroxide, the boronic acid caging group is removed, whereby the subsequent *O*,*N*-acyl shift is enabled. The generated linear isoleucine-serine-alanine sequence then self-assembles into fibrillary structures inside the cell, causing mechanical stress and ultimately cell death. The incorporation of an Coumarin343-unit in the sequence allows for accessory fluorescence imaging of the structures.[24]

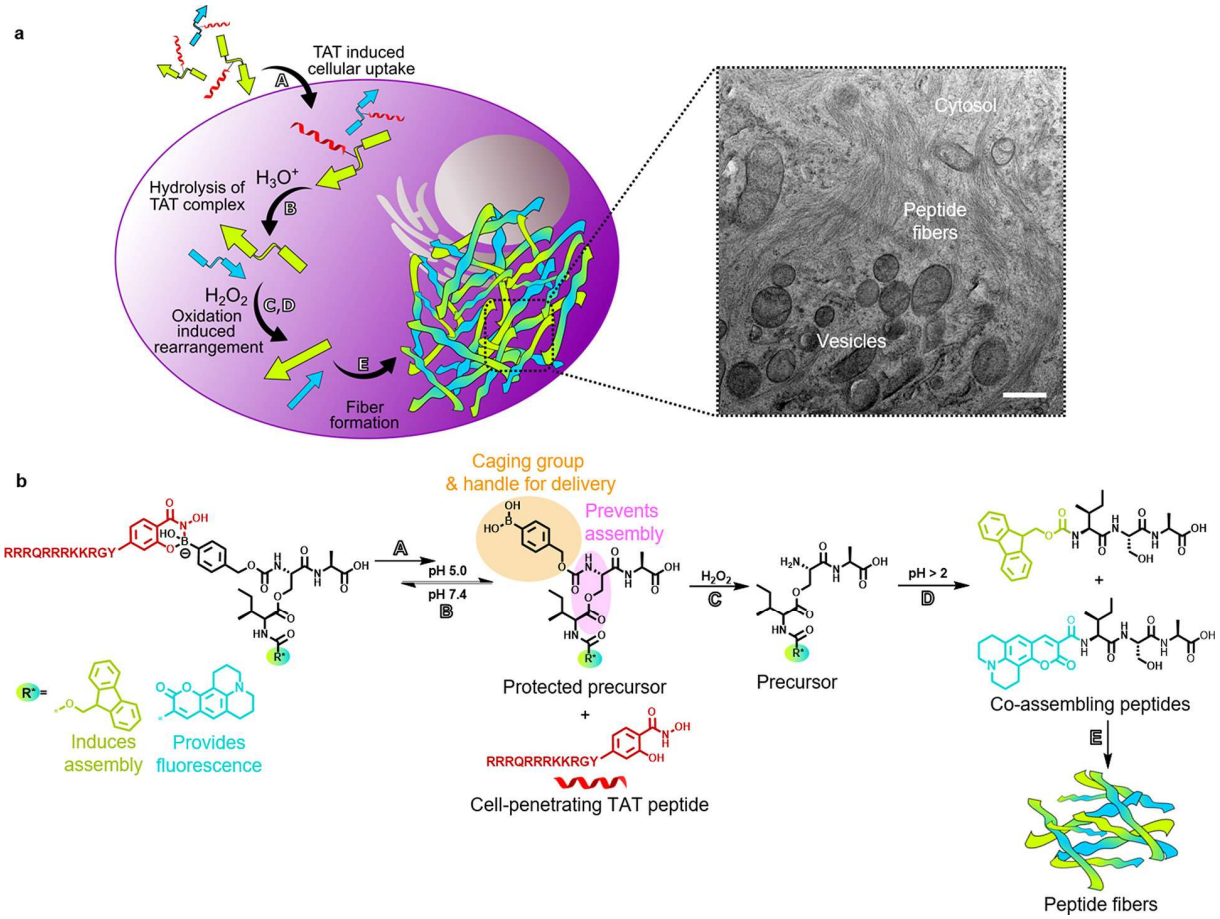

Figure 5: Intracellular coassembly of peptides. (a) Isopeptides (kinked arrows) are uptaken by cells due to dynamic covalently bound salicylhydroxamate-TAT (SHA-TAT, red coil, step A). After hydrolysis of the complex in an acidic environment (step B), the boronic acid headgroup of the isopeptides is cleaved by intracellular hydrogen peroxide (step C). Subsequent O,N-acyl shift forms the linear coassembling peptides (step D). Linear peptides (straight arrows) generate fibrillar networks inside A549 cells (step E), which are visible by transmission electron microscopy (TEM, scale bar 500 nm). (b) Chemical reactions that lead to cellular uptake, peptide linearization, and peptide coassembly of Fmoc (green) and coumarin 343 (blue) functionalized ISA. Taken from[24].

In future studies, the Weil group refined that system with the replacement of the fluorescent dye with a near-infrared (NIR) emitting platinum (II) terpyridine (tpy) complex, while functional modules for cellular uptake and self-immolation of the trigger group are conserved.[26] The Pt-tpy moiety shows absorption of visible blue light and corresponding NIR-emission at 770 nm for the kinked isopeptide and 792 nm for the linear sequence. The emission of the latter one exhibited an increase in intensity due to enhanced metal-metal-to-ligand charge-transfer (MMLCT) transition, which provides insight into the H_2O_2-derived degradation and subsequent assembly into nanofibers.

1.4 Platinum (II) and Peptides

Platinum is the heaviest representative of a group of catalytically active transition metals, which are summarized in the group of platinum metals. In complex compounds, it is mostly present in the +2 (d^8) and +4 (d^6) oxidation states in the form of diamagnetic low-spin complexes in square-planar coordination. Due to the large ligand field splitting of the 5*d* orbitals, other coordination geometries are largely avoided.[46] This makes the relatively simple example of $[PtCl_2(NH_3)_2]$ an excellent demonstration of the trans effect, which describes the kinetic effect that ligands have on the rate of substitution of their opposite (trans-positioned) counterpart. When $[Pt(NH_3)_4]^{2+}$ is treated with chloride ions, the trans isomer is formed because the chlorido ligand has a larger trans effect than NH_3. Therefore, it is necessary to start from the $[Pt(Cl)_4]^{2-}$ complex to isolate the corresponding cis-complex, called cisplatin, after exposure to ammonia (Scheme 2). Cisplatin is a small complex that can add to DNA by ligand exchange and thus crosslink it. Because of that, it is used as a potent chemotherapeutic drug in the treatment of different types of cancer. The comparable trans complex, on the other hand, shows insufficient activity.[47,48]

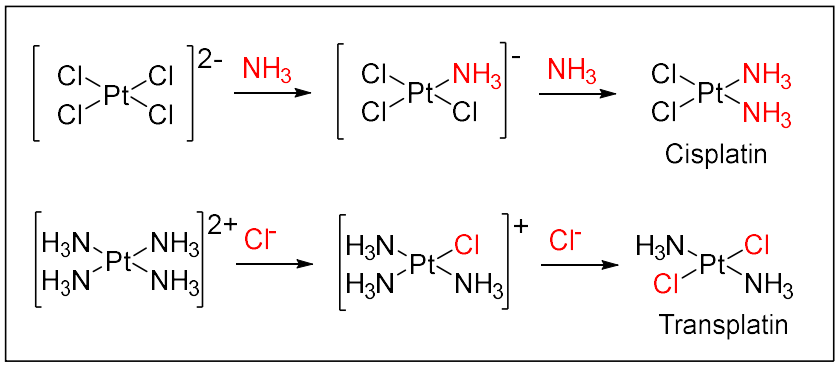

Scheme 2: Synthesis and structure of Cisplatin and Transplatin. [46]

Moving on to more complex coordination systems, the class of tridentate *N*-donor ligands is of great importance. Especially terpyridine ligands have shown interesting behavior with the formation of Pt(II)–Pt(II) and π–π interactions.[49] Depending on the nature of the ligands and the corresponding counter ion, metal–metal distances of 2.9–3.4 Å were reported, pointing out the importance of these interactions for molecular organization and self-assembly (Figure 6b).[50,51] Early studies in this field mainly utilized solid-state polymorphism to conduct photophysical experiments.[51–53] However, these complexes displayed insufficient photophysical properties in solution as triplet *d*–*d* exited states were lower-lying or thermally accessible.[51–53] Moreover, the solubility of

platinum (II) polypyridines were often poor, precluding the preparation of suitable analyte solutions.[51–53]

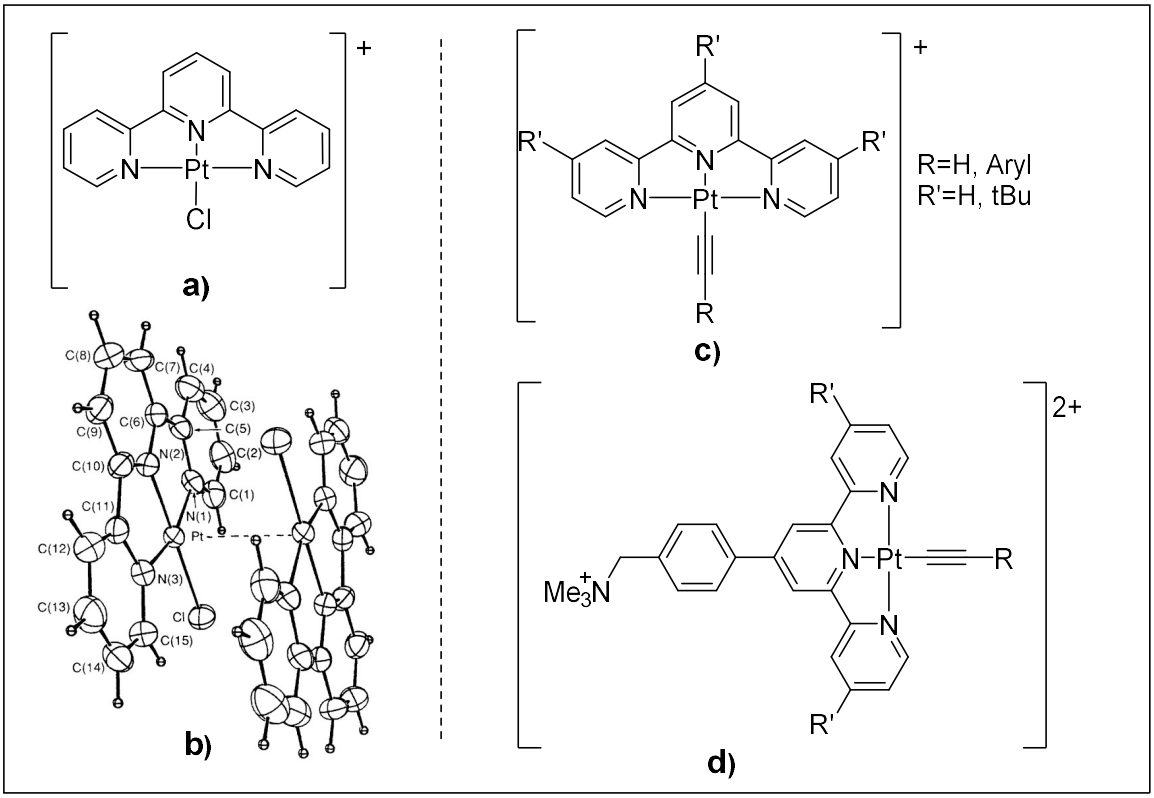

Figure 6: Structures of different Pt(II)(tpy) complexes. $[PtCl(tpy)]^+$ cation (a) as an example for intermolecular metal-metal interactions displayed in the perpective drawing (b) of the crystal structure.[53] Structures of luminescent Pt(II)(alkynyl) complex (c)[54] and water-soluble pendant (d)[55].

In 2001, Yam and coworkers used the strong σ- and π-donor behavior of alkynyl ligands to provide a Pt (II) (tpy) complex with luminescence at the visible spectrum of light (Figure 6c).[54] The emission origin was assigned to a mixture of [*d*π(Pt)→π*(tpy)] triplet metal-to-ligand charge-transfer (^{3}MLCT) and [π(alkynyl)→π*(Pt) triplet ligand-to-metal charge-transfer (^{3}LMCT).[54] Here, the σ-donating character of the alkynyls raises the energy of the *d*σ* orbitals. In combination with the destabilization of the HOMO due to *p*π(alkynyl)–*d*π(Pt) interactions, they achieved an increased *d*–*d* orbital splitting. Summarized, they tailored the system towards increased triplet ligand field excited state and decreased ^{3}MLCT/LLCT state, leading to enhanced luminescence properties.[56] In addition, the introduction of the alkynyl ligand increased the solubility of the complexes in organic solvents[56], which enabled aggregation-related studies.

The solvent-induced formation of Pt–Pt and π–π stacking interactions lead to the emergence of metal-to-metal-to-ligand charge transfer (MMLCT) transitions, exhibiting a red-shifted absorbance and a NIR emission band.[57] Further tuning of the system allowed for water-soluble complexes for applications in a biological context (Figure

6d).[55] The combination of the biologically interesting NIR emission of the complexes with their water solubility furthermore enables bioimaging. Hence, de Cola and coworkers achieved luminescent nanostructures in cellular compartments with localization in the cytosol and nucleus.[58,59] Recently, Weil *et al.* incorporated this NIR-emitting Pt-core (compare Figure 7) into their ROS-responsive multistep cascade isopeptide system[26].

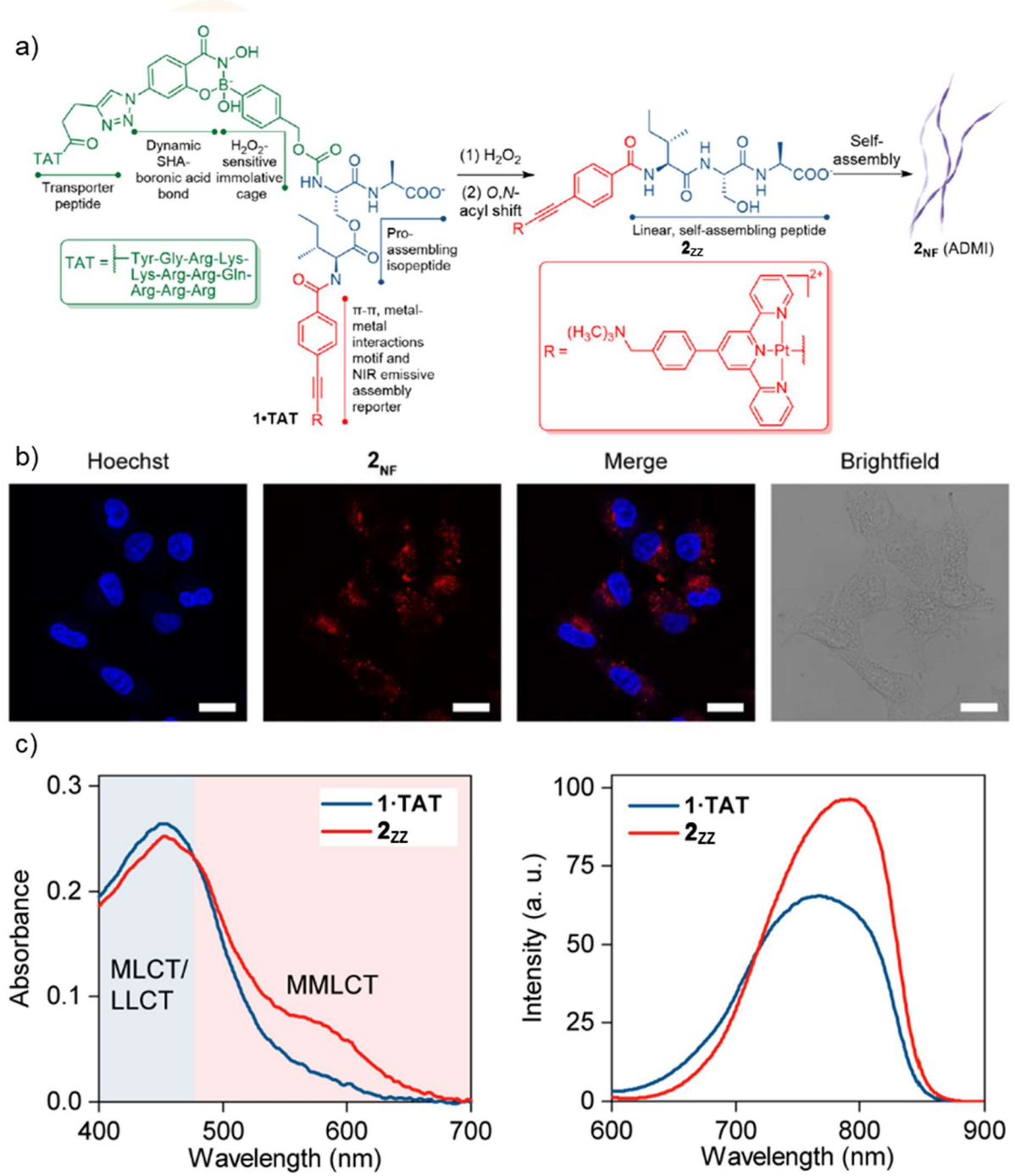

Figure 7: Boronic acid containing Pt (II) peptides. a) Schematic representation of ROS-responsive platinum (II) peptide conjugate with H_2O_2 induced uncaging and linearization. b) Confocal laser scanning micrographs of A549 cells treated for 4 h with 1·TAT (25 µM) and Hoechst dye. Scale bars, 20 µm. c) Absorption (left) and emission (right) spectra of TAT-containing boronic acid Pt (II) complex (1-TAT, blue) and linearized Pt (II) complex (2_{ZZ}, red).[26]

Scrutinizing the effect of this complex on cell metabolism, they found a strong inhibition of the metabolism, in particular the aerobic glycolysis and oxidative phosphorylation, of aggressive metastatic MDA-MB-231 and A549 cells.
The presented findings show that square-planar complexes of platinum (II) coordinated by an alkyne and a tpy moiety can function as a platform for combining two functional molecules (Figure 8).

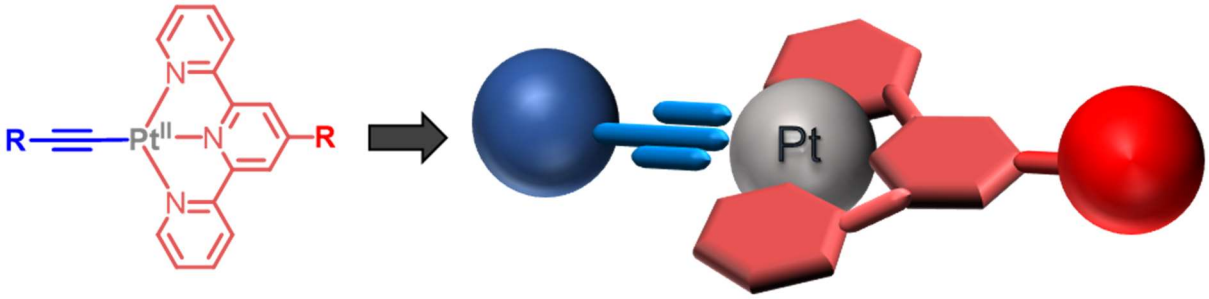

Figure 8: Schematic representation of the complex core. Platinum (II) ion (grey) coordinated by alkyne (light blue) with attached functionality (blue) and terpyridine ligand (light red) with attached functionality (red).

In the context of intracellular self-assembly, this entails the advantageous opportunity to track the distribution and assembly process with the emerging NIR-emission. Furthermore, both sides of the molecule can provide orthogonal functionalities, providing the potential for a higher spatiotemporal control over the intracellular assembly. When peptides are used conjured to the platinum core, the resulting molecule additionally expresses suitable biocompatibility and convenient ways to achieve cellular uptake of the compound.

2 Aim and Objective

Inspired by a multitude of natural examples, intracellular self-assembly moved into the focus of supramolecular research within the last decade. These studies generate fundamental insights for synthetic biology and nanomedicine. Particular attention is paid to the spatiotemporal control of the assembly behavior within the dynamic cellular environment. From high-precision photodynamic approaches to systems tailored towards the exploitation of the tumor microenvironment, numerous examples can be found in the literature.[14,17,24,26,34,36] However, typical challenges include insufficient control and tracking of the intracellular assembly-process. Recently, Weil *et. al.* investigated the formation of nanofibers of platinum (II) based peptide conjugates upon stimulus-response to ROS and pH. Here, the platinum core represents a promising platform to provide both stimuli-responsive control and potential tracking of the intracellular structure formation.

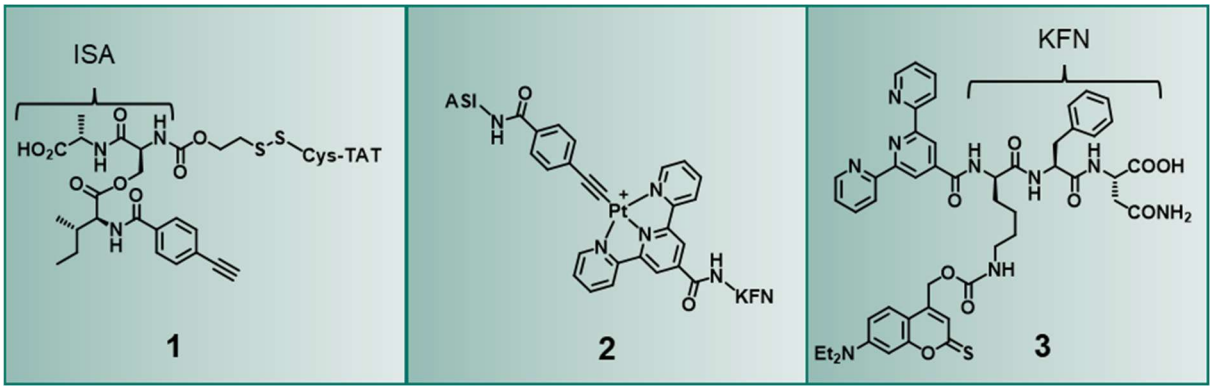

Figure 9: Target molecules of this project. Alkyne bearing ISA-isopeptide with disulfide linker connected to Cys-TAT (TAT = GRKKRRQRRRPQ) (**1**), Pt (II) complex with linear tripeptide ligands (**2**) and coumarin functionalized tpy-KFN (**3**).

Therefore, within this thesis, the combination of stimuli-responsive systems and the NIR-emitting platinum complex shall be investigated. Firstly, a sequence of tripeptides combined *via* Pt (II) (tpy) shall be synthesized to verify not only the emission-profile but also the self-assembly propensity of the motif. To exemplify the amplitude of sequences suitable for the presented platform, two different tripeptides shall be utilized. Ile-Ser-Ala (ISA) represents an interesting representative as it bears the option for implementing an isopeptide bond *via* the serine hydroxy group that can linearize when combined with fitting stimuli-responsive chemical groups. On the other hand, a more hydrophilic sequence needs to be introduced to offer water solubility to the hydrophobic platinum core. Among others, lysine-phenylalanine-asparagine (KFN) is

a suitable candidate that combines satisfactory hydrophilicity with an anchor point to attach functionalities later. To prepare platinum binding sites on these sequences, terpyridine carboxylic acid shall be coupled to the *N*-terminus of KFN and ISA shall be equipped with an alkyne moiety. After the synthesis of this linear peptide complex ASI-Pt (II)-KFN, its self-assembly shall be analyzed with transmission electron microscopy (TEM) and the corresponding absorption and emission spectra, shall be recorded.

Subsequently, the introduction of stimuli-responsive groups into the molecular design of the tripeptide ligands shall be investigated. The most precise control over functionalities can be achieved with photoprotective groups. Upon irradiation the caged structures can literally be switched on or off. Among others, coumarin derivatives display appropriate PPGs for biological applications as the byproducts of photoinduced cleavage do not interfere severely with the living system and their absorption band can be red-shifted away from cytotoxic UV-light. Therefore, the literature-known thio-coumarin **13** shall be prepared and attached to the amine residue of tpy-KFN. After the verification of the absorption maximum, the photoinduced cleavage of the photoprotective group shall be investigated with UV/Vis spectroscopy supported by LCMS analysis of the kinetics of degradation and rearrangement.
As mentioned before, the ISA motif bears the possibility of introducing an isopeptide bond into the design. This results in a kinked molecular architecture prohibiting self-assembly until the structure linearizes. When the *N*-terminus is caged by a stimulus-responsive group, this concept displays an elegant example of a multistep cascade controlling the self-assembly behavior of a structural element. To generate an orthogonality to the extrinsic light stimulus on the KFN peptide, a responsive group is implemented that exploits the tumor microenvironment intrinsically. As such, a GSH-responsive self-immolative disulfide linker fits the criteria optimally. It capitalizes on the elevated concentration of the reducing agent glutathione in various cancer types, while offering an additional binding site for a cell-penetrating sequence (e.g. TAT) that enables cellular uptake. Therefore, the caged isopeptide **21** shall be synthesized and coupled to a TAT sequence that was prolonged by an additional cysteine. To generate a model complex for analyzing the complexation behavior, GSH-induced degradation kinetics and cellular uptake of this intricate peptide conjugate, it shall be bound to a water soluble Pt (II) (tpy) precursor (**23**).

Having established these two responsivities in the context of platinum-peptide conjugates, the last step shall be the combination of both elements with the Pt (II) (tpy) platform, ultimately leading to a dual-responsive, NIR-emitting platinum (II) complex that can form self-assembled architectures within living cells.

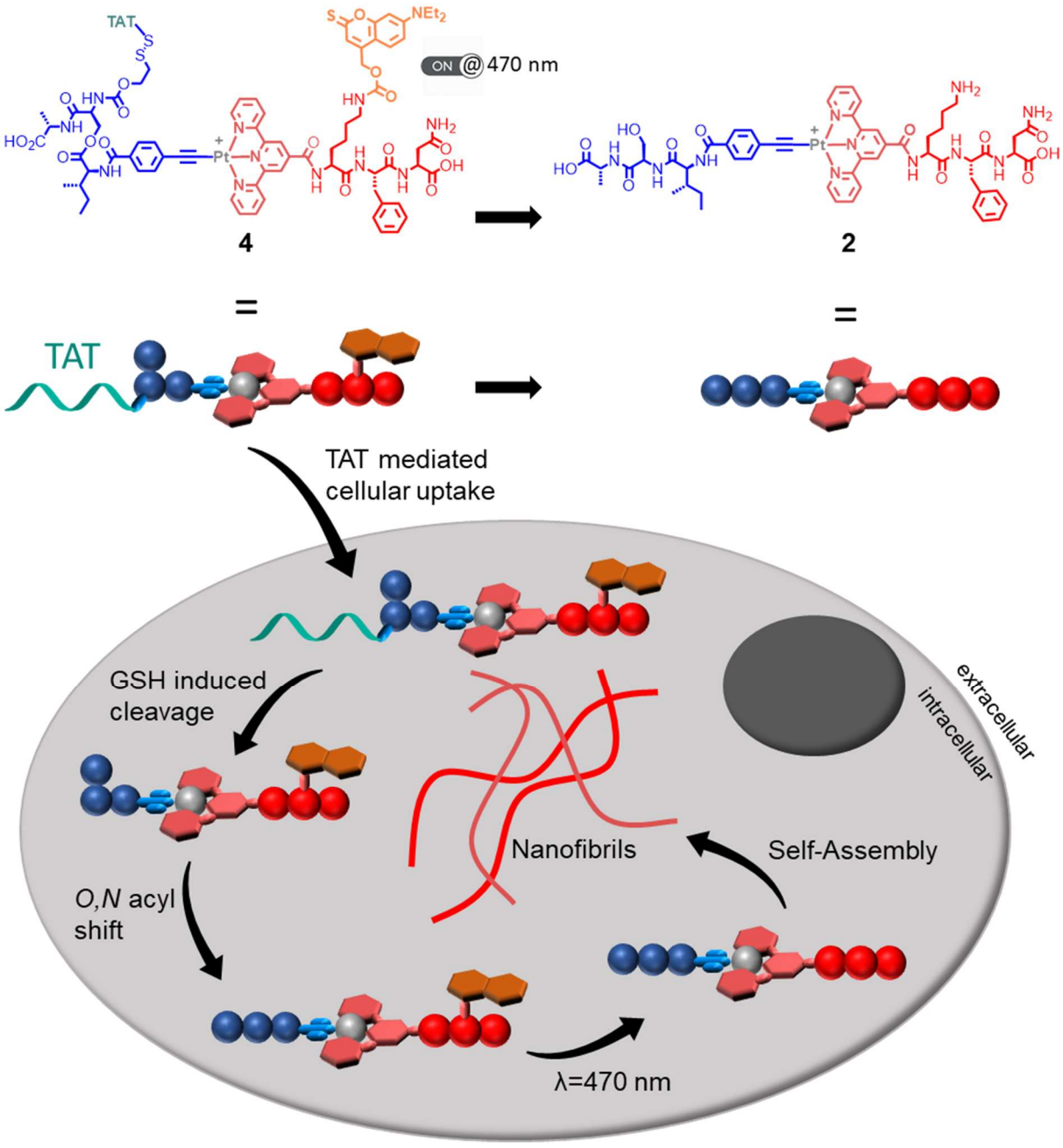

Figure 10: Intracellular self-assembly of platinum (II) based peptides. Dual-responsive starting material is uptaken by cells due to cell-penetrating Cys-TAT sequence attached covalently *via* disulfide bond. GSH-induced reduction in the cytosol enables subsequent self-immolation of the linker. Following *O,N*-acyl shift forms the linear tripeptide. Upon irradiation (470 nm) of the PPG, the completely linearized complex is obtained that can then generate fibrillary networks inside living cells.

3 Results

The preparation of the dual-responsive Pt (II) peptide conjugate is based upon the synthesis of two functionalized peptides. On the one hand, there is the linear tripeptide KFN with a thio-coumarin as photoprotective group on the lysine side chain, and on the other hand, the ISA isopeptide functionalized with the cell-penetrating sequence TAT *via* a disulfide linker. Furthermore, this includes the linear Pt (II) conjugate as a control of self-assembly behavior after the cleavage of the caging groups and subsequent rearrangement reactions.

3.1 Linear Peptide Platinum Conjugate ASI-Pt (II)-KFN

As a proof of concept for the self-assembly behavior of the designed sequence, the linear complex ASI-Pt (II)-KFN (**2**) was synthesized. This sequence represents the final product of the GSH- and light-induced reaction cascade and is therefore subsequently analyzed with TEM regarding its assembling behavior.

The ISA motif was chosen, as it provides the opportunity to introduce an isopeptide bond *via* the serine hydroxyl group. This modification results in a kinked structure with low propensity of self-assembly. Upon decaging of the *N*-terminal linker, the system self-immolates into the linear motif with increased tendency towards self-assembly. On the other hand, the KFN sequence was designed to provide satisfactory water solubility and the possibility to attach a PPG to the lysine side chain.

3.1.1 Synthesis of Peptide Platinum Conjugate

The actual synthesis of **2** started with the solid-phase peptide synthesis (SPPS) of ISA and KFN, respectively. ISA was prepared using alanine loaded Wang resin at 0.5 mM scale with final deprotection of the *N*-terminus. Subsequently, 4-ethynyl-benzoic acid was coupled to the free amino group on resin with Oxyma® and *N,N'*-diisopropylcarbodiimide (DIC). The functionalized peptide was then cleaved off the solid support with 95% trifluoroacetic acid (TFA), resulting in the linear peptide **5**. KFN was similarly prepared using asparagine loaded Wang resin at 0.5 mM scale. After deprotection of the *N*-terminus, it was further reacted with [2,2':6',2''-terpyridine]-4'-carboxylic acid and cleaved off the resin. As complexation experiments with a free amino group on the lysine side chain showed deficient results, the base-labile Fmoc protecting group was introduced with Fmoc-OSU resulting in Fmoc-protected tpy-

KFN (**6**). After this, the platinum (II) precursor was inserted in the terpyridine moiety on the KFN sequence and subsequently complexed to the alkyne residue on the ISA motif. This coordination sphere provides not only high stability, but also appropriate water solubility and interesting photophysical properties.

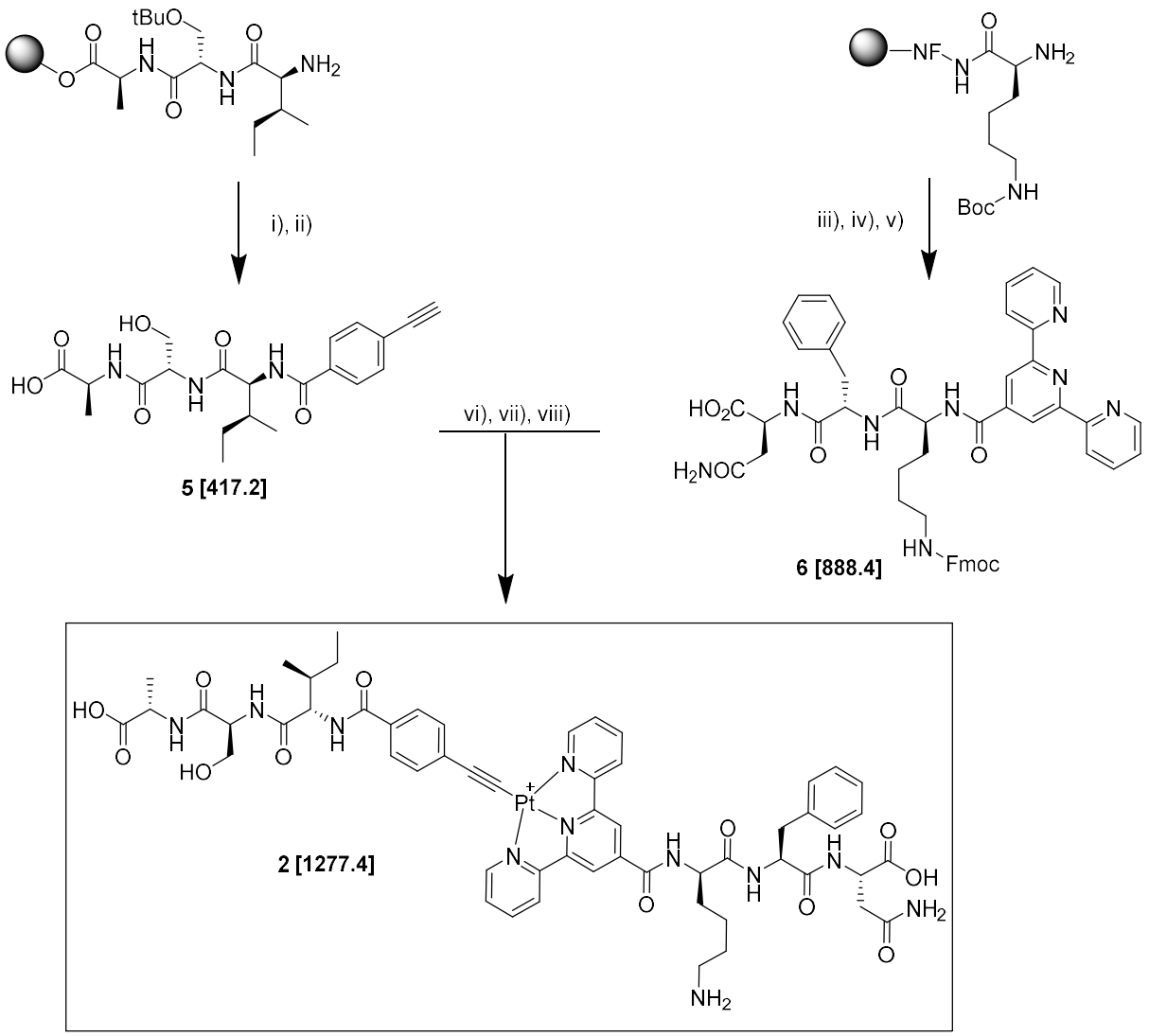

Scheme 3: Synthesis of linear peptide Pt (II) conjugate (2). i) 4-ethynylbenzoic acid, Oxyma®, DIC, *N,N'*-dimethylformamide (DMF), room temperature (rt), over night (on); ii) TFA (95%), triisopropylsilane (TIPS) (2.5%), water (2.5%), rt, 2 h; iii) [2,2':6',2''-terpyridine]-4'-carboxylic acid, (Benzotriazol-1-yloxy)tripyrrolidinophosphonium hexafluorophosphate (PyBOP), diisopropylethylamine (DIPEA), DMF, rt, on; iv) trifluoroacetic acid (TFA) (95%), triisopropylsilane (TIPS) (2.5%), water (2.5%), rt, 2 h; v) Fluorenylmethoxycarbonyl-oxysuccinimid (Fmoc-OSU), dioxane/water (1:1), rt, 2 d; vi) $PtCl_2(DMSO)_2$, DMF, reflux, on; vii) CuI, DIPEA, DMF, 50°C, on; viii) piperidine in DMF (20%), rt, 30 min.

3.1.2 TEM Analysis of Self-Assembly Behavior of linear ASI-Pt (II)-KFN

The linear peptide platinum conjugate **2** represents the endpoint of the multistep reaction cascade and was designed to self-assemble inside living cells. Therefore, transmission electron microscopy (TEM) studies were conducted to analyze the assembly behavior. To stay closer to the biological model, the measurements were performed with minimal amounts of DMSO in aqueous buffer solution (DPBS or HEPES). Because of the insufficient solubility of the complex in pure buffer, 2% DMSO content was necessary. The samples were stained with uranyl acetate after incubation on the TEM grid. Concentrations of 100, 50, 25 and 10 µM with 2% DMSO content were analyzed. The two higher concentrations showed the formation of nanofibers, while for the lower two concentrations no structure formation was observed. The reason for this lack of structure formation could be based on solubility. On the one hand the 2% DMSO content can change the behavior in comparison to cellular studies that are subject of future research. On the other hand the free amine group could increase the critical aggregation concentration to higher concentrations. Lastly, the interactions of the peptide with the surface of the vial during sample preparation could be problematic. Therefore, vessels with low protein interactions are scrutinized in near future.

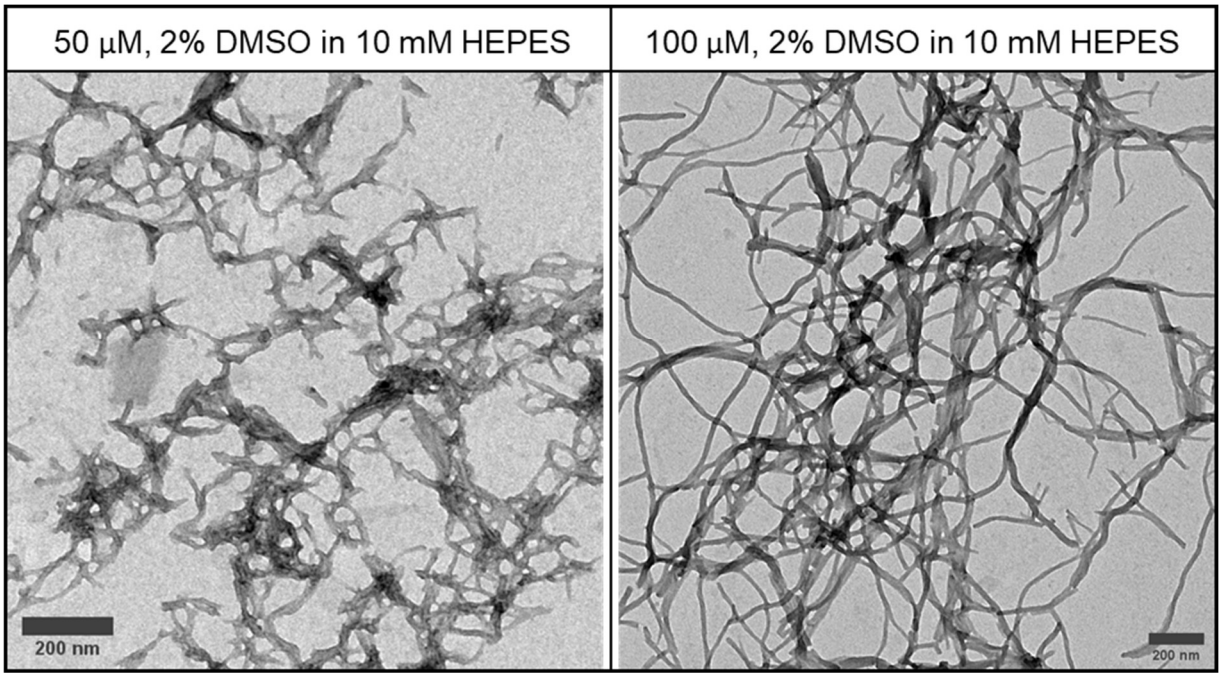

Figure 11: TEM images of compound 2. Peptides were dissolved in DMSO and diluted with HEPES buffer (10 mM) resulting in concentrations of 100, 50, 25 and 10 µM (2%DMSO). Grids were stained with uranyl acetate. Scale bars = 200 nm.

3.1.3 Absorption and Emission of Pt (II) complex

The square-planar platinum (II) complex exhibits intrinsic optical properties that allows visualization within bio experiments. As such, complex **2** (JL35) displays an absorption band at ca. 460 nm in DPBS buffer that can be attributed to a combination of *d*π(Pt)→π*(tpy) MLCT and LLCT interactions between the alkynyl and the terpyridine ligands. Additionally, an absorption shoulder at lower energies (broad ca. 590 nm) due to metal-metal-to-ligand charge-transfer (MMLCT) transitions can be observed.[26,60] Upon excitation at 488 nm, the complex shows a NIR emission centered at 800 nm originating from MMLCT excited states. These findings are in accordance with the results of earlier research that was discussed in chapter 1.4.

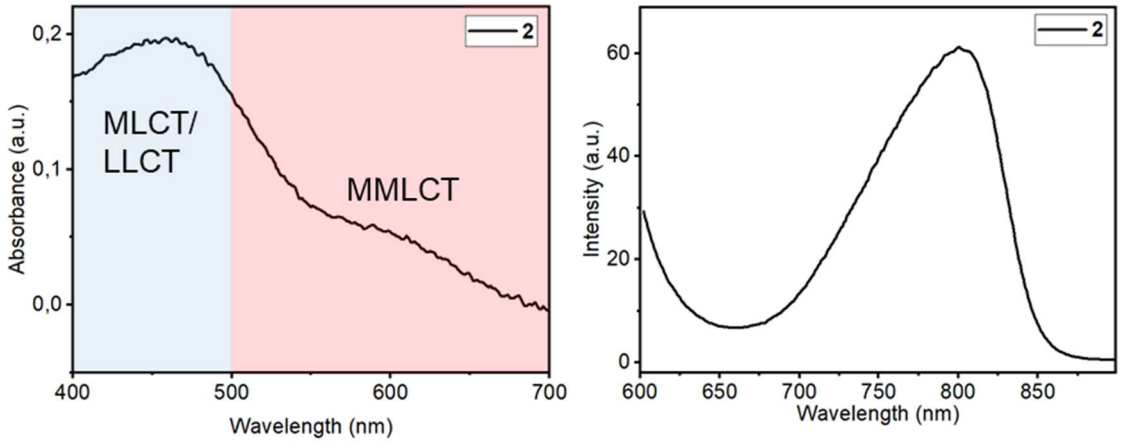

Figure 12: UV/Vis absorption and luminescence emission spectra of linear peptide platinum (II) complex 2. 50 µM in DPBS (1% DMSO). Excitation wavelength for emission 488 nm.

3.2 Photoresponsive Peptide System

To gain precise control over the self-assembling behavior the extrinsic stimulus of light should be introduced in the molecule. Regarding the photoprotecting group (PPG) different biocompatible groups are suitable. The thio-coumarin **13** was chosen, because it shows an absorption maximum in the range of visible blue light (470 nm) to circumvent the use of cytotoxic UV light. Furthermore, the side product of the uncaging does not interfere severely with the biological system and offers the option for further modification later on.[61]

The PPG can be attached to a nucleophile side chain of a peptide *via* activation as a reactive carbonate. For the peptide sequence, a rather polar tripeptide with a lysine to attach the PPG was chosen. Lastly, a terpyridine ligand was connected to the *N*-terminus of the peptide to achieve a platinum binding site.

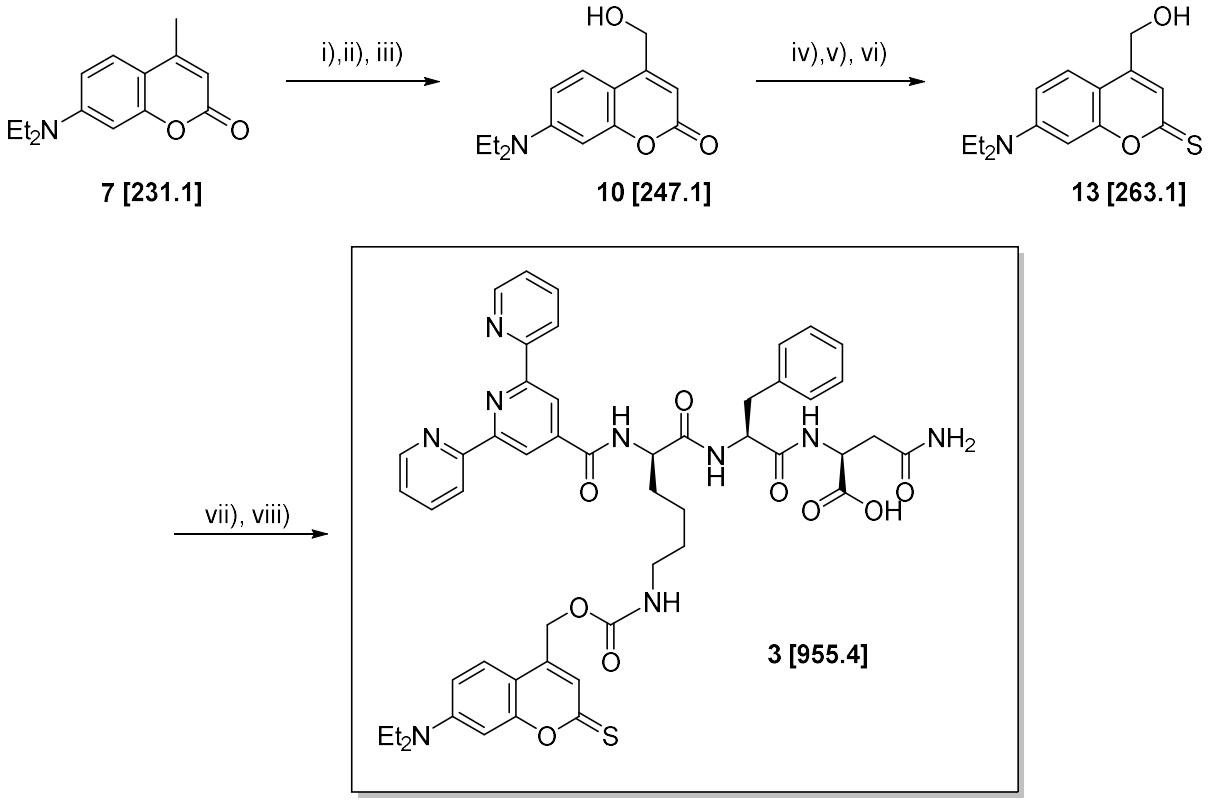

Scheme 4: Synthesis of coumarin attached tpy-KFN (3). i) DMF-DMA, DMF, reflux, on; ii) $NaIO_4$, THF/water, rt, on; iii) $NaBH_4$, THF, rt, 6 h; iv) HOAc, DIC, DMAP, DCM, rt, on; v) lawesson's reagent, toluene, reflux, on; vi) HCl in ethyl acetate (1 M), EtOH, reflux, on; vii) 4-nitrophenyl carbonochloridate, DIPEA, DMAP, DCM, rt, on; viii) **15**, DIPEA, DMAP, rt, on.

3.2.1 Synthesis of photolabile coumarin

The thio-coumarin alcohol **13** was prepared from the methyl precursor **7** in six steps (Scheme 5)[37,38,62]. Firstly, the CH-acid methyl coumarin **7** was condensed with *N,N'*-dimethylformamide dimethyl acetal (DMF-DMA) to the corresponding enaminone in 56% yield. Some of the products hydrolyzed resulting in the corresponding coumarin aldehyde and therefore decreasing the yield. The next step was the oxidation of the enaminone **8** to the aldehyde **9** with $NaIO_4$ as the oxidizing agent in 83% yield. Subsequently, the Aldehyde was reduced with sodium borohydride resulting in the coumarin alcohol **10** (35% yield). The mediocre yield of the last step was unexpected as reductions with $NaBH_4$ typically lead to good yields. Furthermore, the reaction control by LCMS indicated good conversion (compare Figure 55). That is why, the purification by manual column chromatography over silica gel was identified as the main reason for the yield loss. Currently, the coumarin was purified by manual column (different solvent mixtures were tried) with reduced exposure to light. For future synthesis, HPLC approaches or shorter columns with exclusion of light can be investigated.

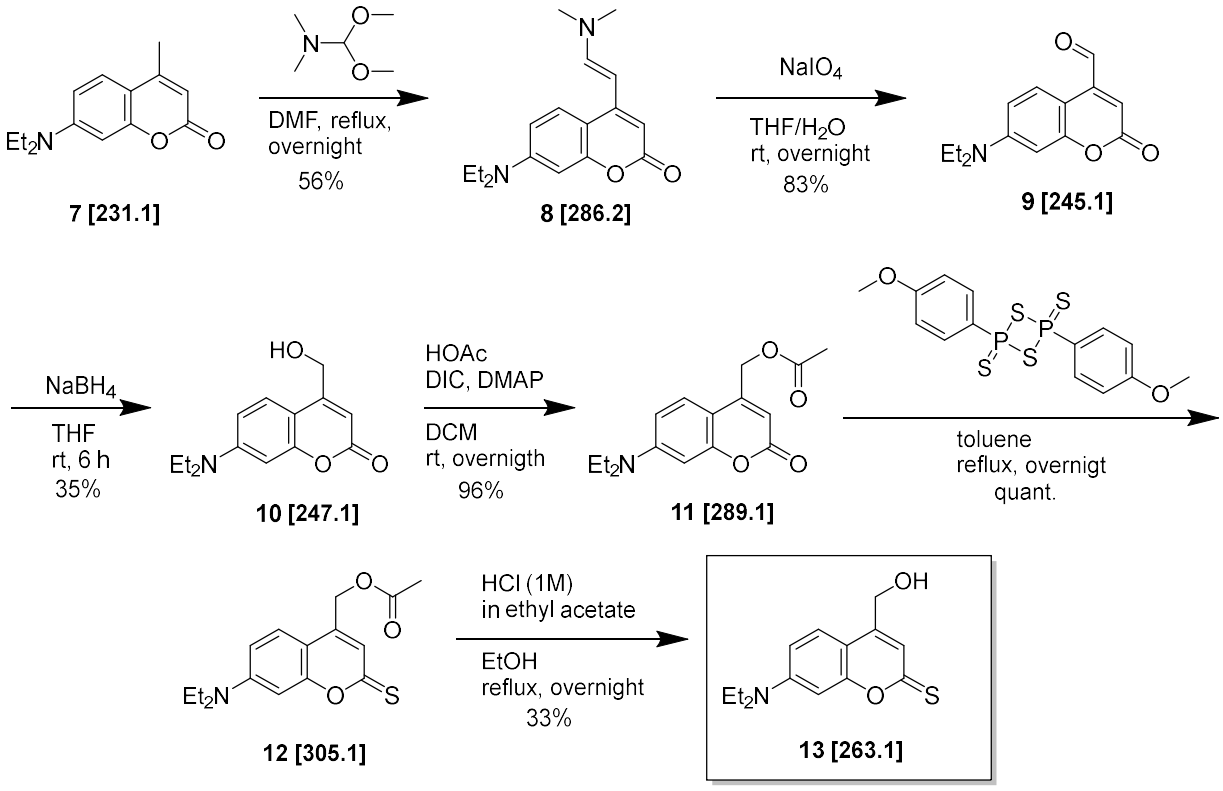

Scheme 5: Synthesis of thio-coumarin alcohol 13 in six steps. Starting with the oxidation of methyl precursor **7** to enamine and aldehyde. Subsequent reduction to alcohol **10**. Protection of the hydroxyl group, thionation with Lawesson's reagent and deprotection.

While the product of the first three steps is also available commercially, it has high cost and was not available constantly. That's why it was decided to generate the material from the cheaper precursor. Weinrich *et al.*[62] also describe a quicker route without purification in between the steps that might lead to higher yields as the product loss due to the purification steps is minimized. This was not yet verified and is subject of upcoming experiments.

The further synthesis included the protection of the alcohol by esterification with acetic acid (96% yield) and thionation using Lawesson's reagent (quant.). The final step was the deprotection of the alcohol using HCl in ethyl acetate (1M), yielding 33% of the desired product **13**. The poor yield might be because of photoinduced degradation or not optimized purification during the manual column chromatography over silica gel as described previously for the alcohol **10**. Here again, purification by HPLC is an interesting option, as the exposure to light can be minimized and the conditions further optimized. The product was analyzed by ^{1}H-NMR spectroscopy (Figure 13) and LC-MS (Figure 14).

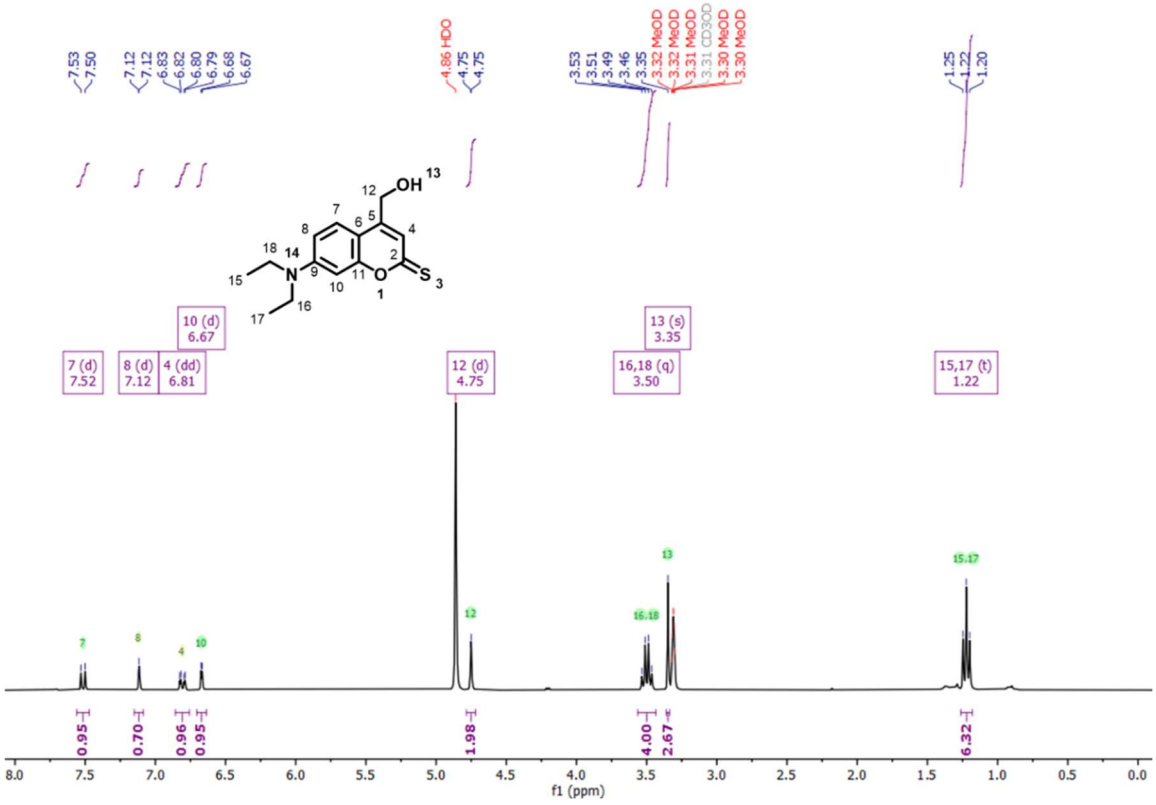

Figure 13: ^{1}H-NMR spectrum of thio-coumarin alcohol 13 (d4-MeOH, 300 MHz, 298 K). Processed with MestReNova.

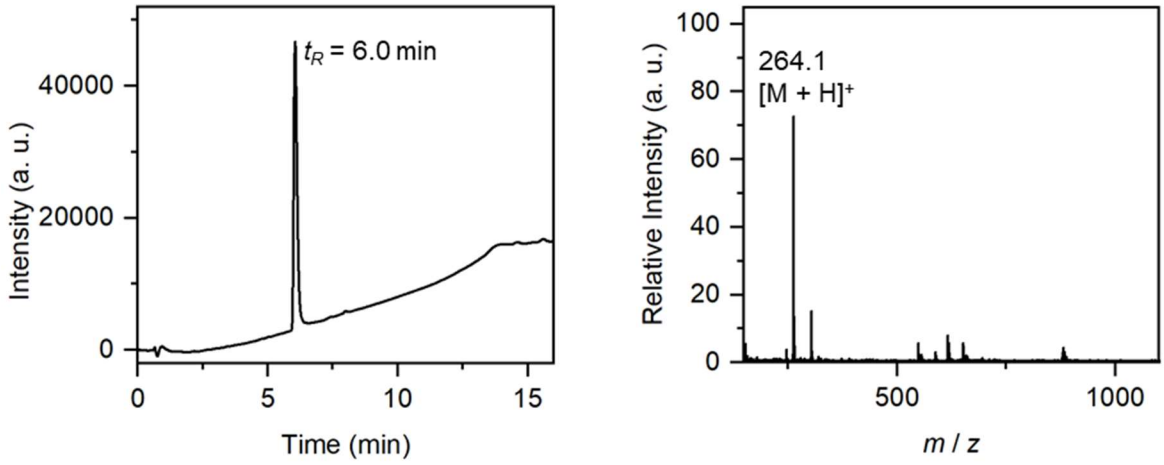

Figure 14: LCMS data of thio-coumarin alcohol 13. LC elugram (left, detection at 254 nm) and corresponding mass data (right).

3.2.2 Attachment of Thio-Coumarin to Tripeptide

After the synthesis of the thio-coumarin, it was attached to the tpy-KFN sequence **15** (synthesis shown in Scheme 3, step iii and iv) to introduce light-responsiveness.

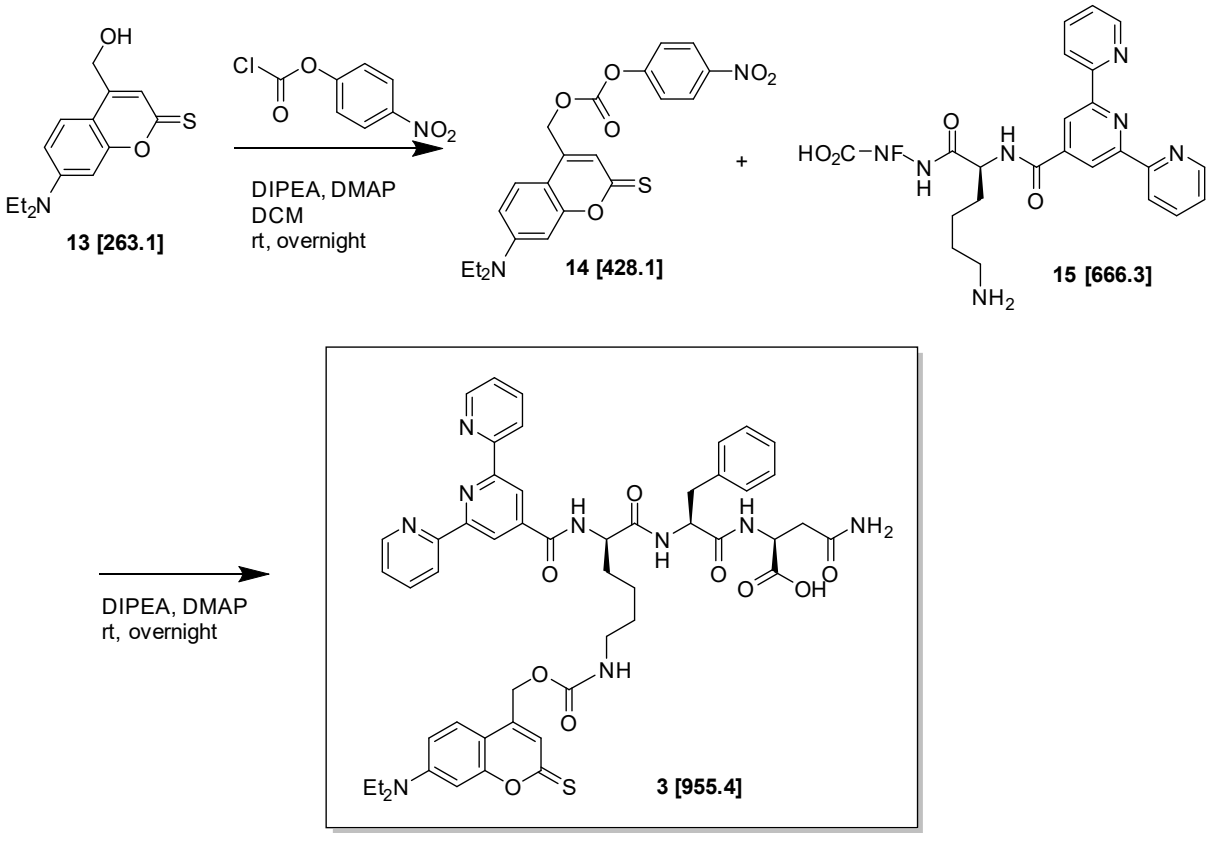

Scheme 6: Synthesis of coumarin attached tpy-KFN (3). Activation of the thio-coumarin as a reactive carbonate followed by reaction with free amine at lysine side chain of KFN.

To attach the thio-coumarin **13** to the tripeptide KFN (**15**), the coumarin was first activated *via* the reaction with 4-nitrophenyl chloroformate. As the LCMS data of the activated coumarin indicated sufficient purity, the generated reactive carbonate (**14**) was then conjugated to the free amine side chain of the tripeptide without further purification. The desired product **3** was isolated *via* HPLC and subsequent lyophilization as an orange solid (4 mg, 7%). The tripeptide (**15**) showed insufficient solubility in dichloromethane (DCM) and *N,N'*-dimethylformamide (DMF), which may have led to the poor yield.

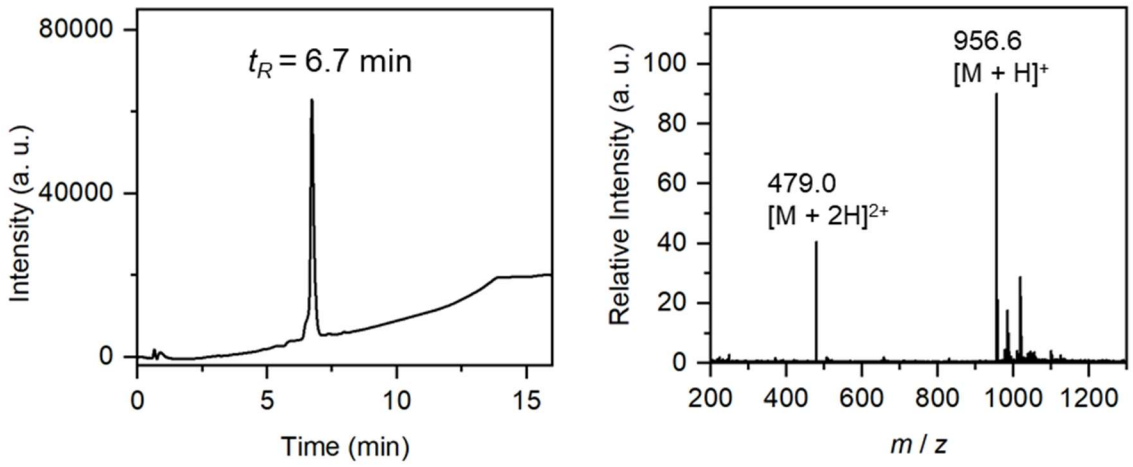

Figure 15: LCMS data of coumarin conjugated NFK-terpyridine 3. LC elugram (left, detection at 254 nm) and corresponding mass data (right).

To increase the yield, a prolonged reaction time was tested. However, LCMS analysis indicated an increased formation of a dimeric coumarin carbonate **16** as byproduct and a further decrease in the desired product (compare Figure 16), excluding an increase in reaction time as an option for improved yields. Therefore, it was concluded that the solubility of **15** needs to be adjusted. Here, either a change of the solvent system (e.g. methanol) or the change of the counterion of the peptide (currently trifluoroacetate due to purification *via* HPLC) can be investigated in future.

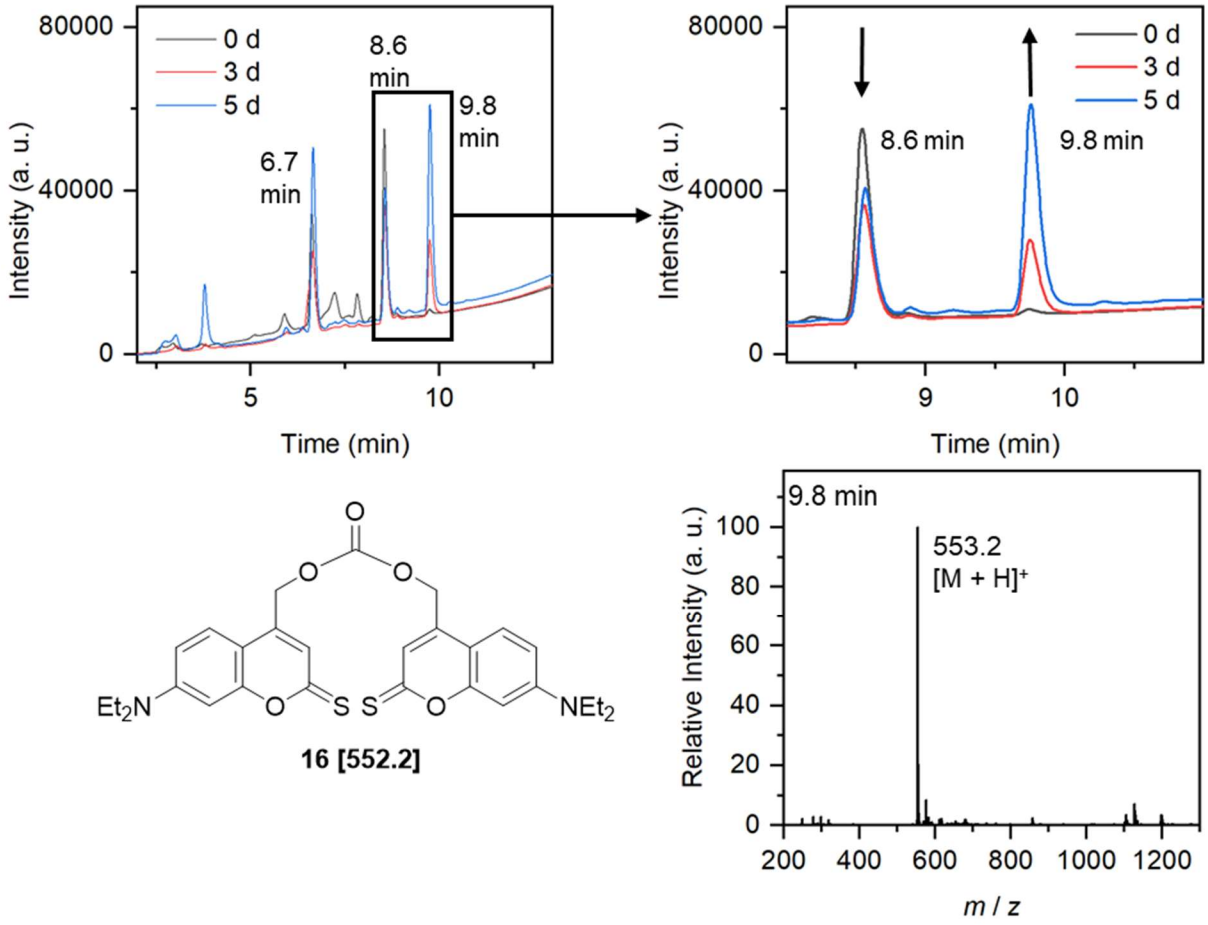

Figure 16: Coumarin attachment to tripeptide over time. LC elugrams (detection at 254 nm) for different reaction times and mass data corresponding to t_R=9.8 min after five days reaction time.

3.2.3 Photodynamic Behaviour of Thio-Coumarin-KFN-tpy

The UV/Vis absorption spectrum of the thio-coumarin **13** is described in literature and displays a maximum at λ = 470 nm (Figure 17 B, DEACMS-OH) in a 1:1 mixture of ACN/water.[38] For comparison, the UV/Vis-spectrum of compound **3** was therefore measured in a 1:1 mixture of ACN and DPBS buffer in 50 µM concentration. Under similar conditions a control measurement of the peptide without coumarin was conducted. The resulting spectrum of JL47 (Figure 17 A) shows a broad absorption at 473 nm corresponding to the main absorption of the coumarin, as well as additional bands below 300 nm that can be attributed to absorptions of the peptide backbone without the dye (**15**). After the spectrum of the caged molecule was recorded, irradiation experiments with a blue LED emitting light at 470 nm were performed.

For the experimental setup, the cuvette containing the peptide solution was placed in 3 cm distance to the source of light and irradiated in distinct time intervals. The power of the lamp was P = 15 W. The intensity (I) of light is calculated for a given area (A) in space as the quotient of the amount of light energy (E) transmitted (through this area) per time (t) and the size of the area.[63]

$$I = \frac{\frac{dE}{dt}}{A} = \frac{P}{A} \quad (1)$$

Assuming a point-like light source that emits light equally in all three dimensions, and with the energy loss (e.g. absorption) excluded, the corresponding intensity decreases quadratically with the distance to the object:

$$I = \frac{P}{A} = \frac{P}{4\pi r^2} = \frac{15\,W}{4\pi(3\text{ cm})^2} = 0.133\frac{\text{W}}{\text{cm}^2} \quad (2)$$

The maximum of the absorption band showed a minor hypsochromic shift (473 nm → 465 nm, compare Figure 17 D). Moreover, the absorption band itself exhibited decay over time, because of further photolysis of the intermediary formed thio-coumarin **13** that was also reported in previous studies[37,38]. After 180 s of irradiation, the solution was analyzed with LCMS (Figure 17 C). The starting material (**3**) with an elution time of t_R = 6.7 min was converted to the tpy-KFN (**15**, t_R = 3.8 min) and the thio-coumarin alcohol (**13**, t_R = 6.2 min) completely.

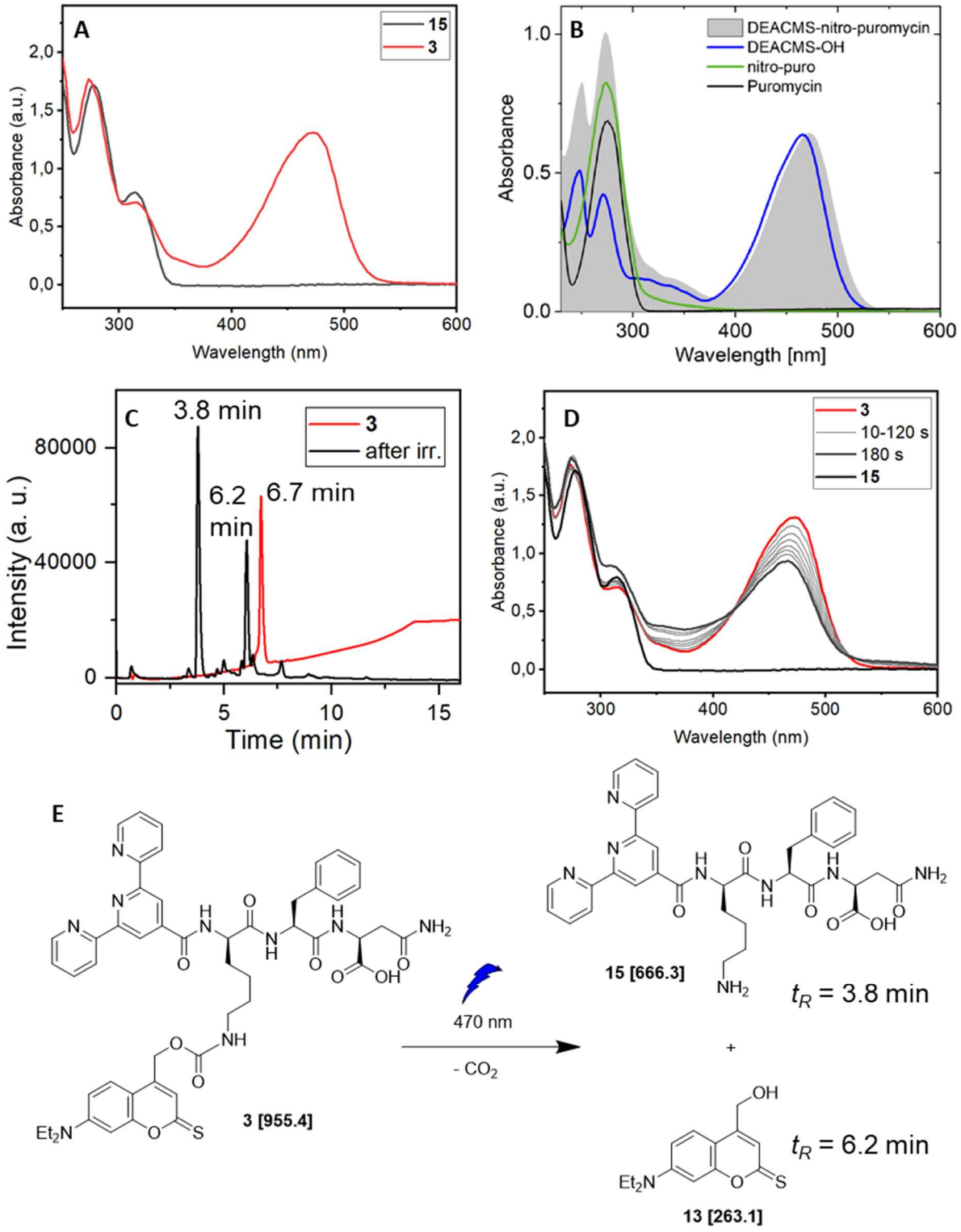

Figure 17: Photodynamic experiments with KFN derivatives. UV/Vis-spectrum of KFN-tpy with (**3**) and without (**15**, normalized) attached coumarin (A) and comparable spectra from the literature (B, DEACMS-OH = **13**)[38], LC chromatogram (C, detection at 254 nm) after 180 s irradiation, UV/Vis-spectra of **3** with applied irradiation at 470 nm (D), reaction scheme of photoinduced deprotection (E).

3.3 Glutathione responsive Peptide System

As previous results[24,26,44] demonstrated the promising self-assembling behavior of the isopeptide ISA sequence, the moleculare structure was optimized to contain the disulfide linker attached to the TAT sequence as well as an additional alkyne to generate a platinum binding site.

3.3.1 Synthesis of isopeptide with activated disulfide-bond

For the GSH-responsive functionality of the target molecule, isopeptide **21** was synthesized in seven steps (compare Scheme 7).

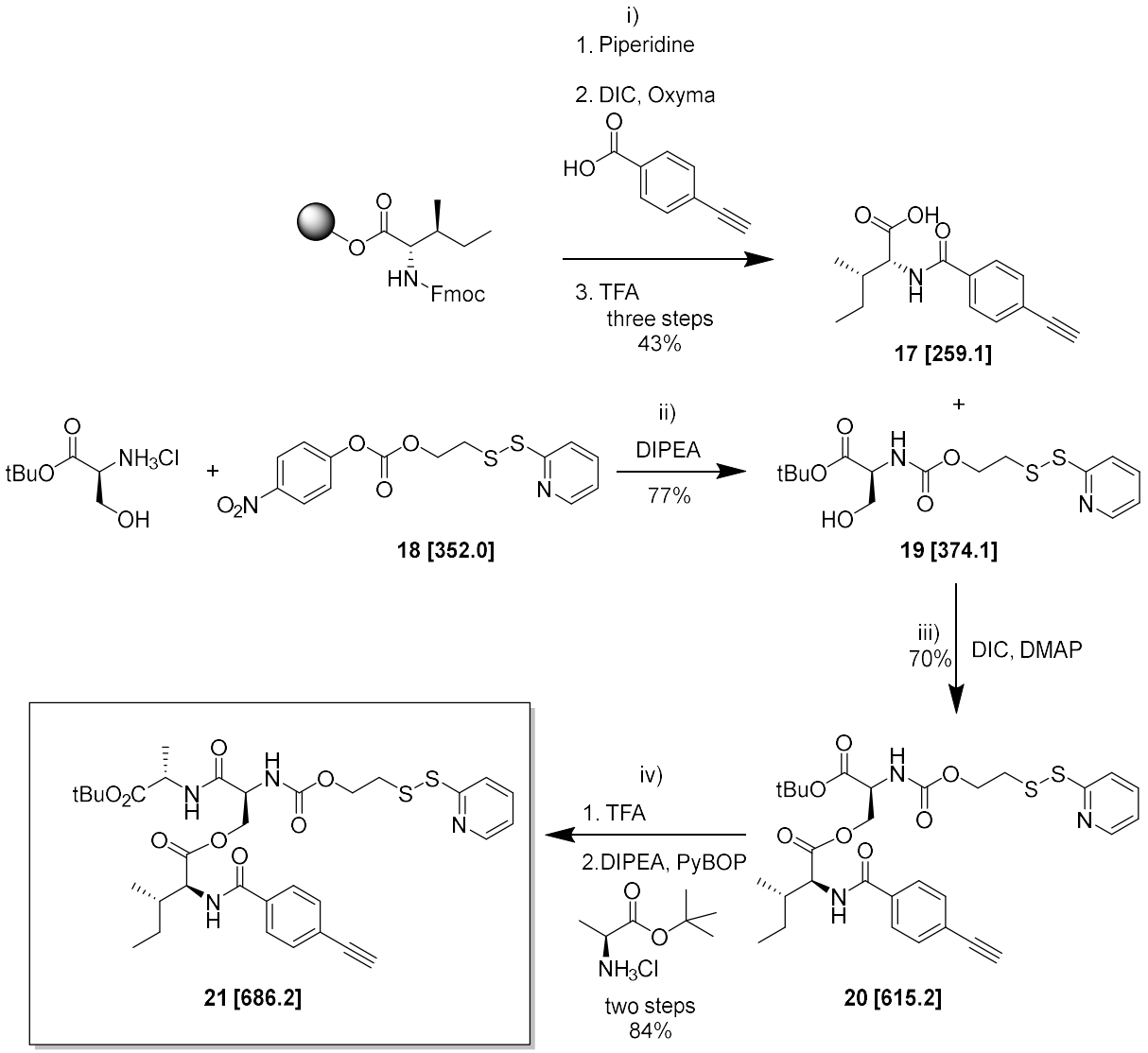

Scheme 7: Synthesis of isopeptide with activated disulfide bond. i) 1. Piperidine in DMF (20%), rt, 4x10 min, 2. DMF, rt, overnight, 3. 95% TFA, 2.5% TIPS, 2.5% H2O, rt, 2 h; ii) DCM, rt, overnight; iii) DCM, rt, overnight; iv) 1. 50% TFA, 50% DCM, rt, 6 h, 2. DCM, rt, overnight.

The first three steps were conducted in a Merrifield apparatus. Fmoc-isoleucine loaded (0.70 loading) Wang resin was deprotected using piperidine in DMF (20%), followed by DIC and Oxyma® supported coupling of 4-ethynylbenzoic acid. After cleavage using 95% TFA, the isoleucine-alkyne **17** was isolated in 43% yield. The activated disulfide **19** was prepared in 77% yield by DIPEA mediated coupling of tert-butyl protected serine hydrochloride to the reactive carbonate **18**. The subsequent esterification of **17** and **19** yielded **20** in 70% yield. After deprotection of the *C*-terminus with 50% TFA, *tert*-butyl protected alanine hydrochloride was coupled to the compound using DIPEA and PyBOP. The final isopeptide **21** was isolated in 84% yield as a colourless solid by HPLC following lyophilization and analyzed by LC-MS (Figure 18). Additionally, the *tert*-butyl protecting group was removed to generate comparative material for cellular uptake without the TAT (compound **22**).

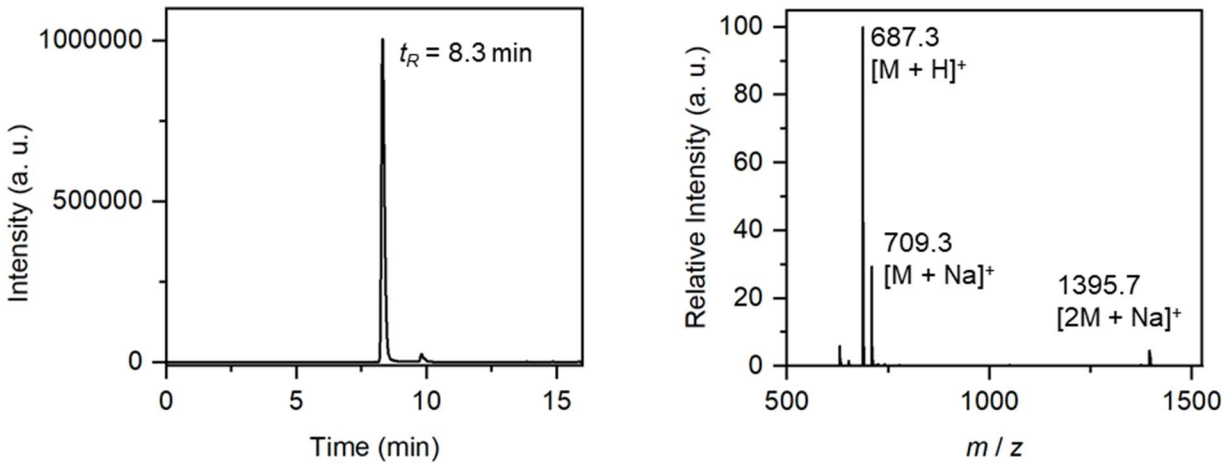

Figure 18: LCMS data of isopeptide 21. LC elugram (left, detection at 254 nm) and corresponding mass data (right).

3.3.2 Synthesis of TAT and conjugation to the Isopeptide

The cell-penetrating peptide TAT (transactivator of transcription) was synthesized *via* Fmoc solid-phase synthesis using Rink Amide resin at a 0.1 mmol scale (Scheme 8). The original amino acid sequence of TAT (YGRKKRRQRRR) was extended to include an additional *L*-cysteine at the *N*-terminus that provided the thiol group for the conjugation to the isopeptide **21** *via* disulfide-exchange reaction. The Monomethoxytrityl-group (Mmt) was chosen as the protecting group for the cysteine thiol as it is removable selectively using mild acidic conditions (2% TFA, five times for 10 min) while other side chain protecting groups or the linkage between the peptide and the solid phase are not affected. The resin-bound cysteine-modified TAT with a free thiol group then underwent a disulfide-exchange reaction with the isopeptide **21** replacing the pyridyl-substituent of the activated disulfide-bond. The resulting resin-bound isopeptide-TAT-conjugate was cleaved off the solid phase using a 95% TFA-solution which also removed all protecting groups yielding 37% of compound **1**.

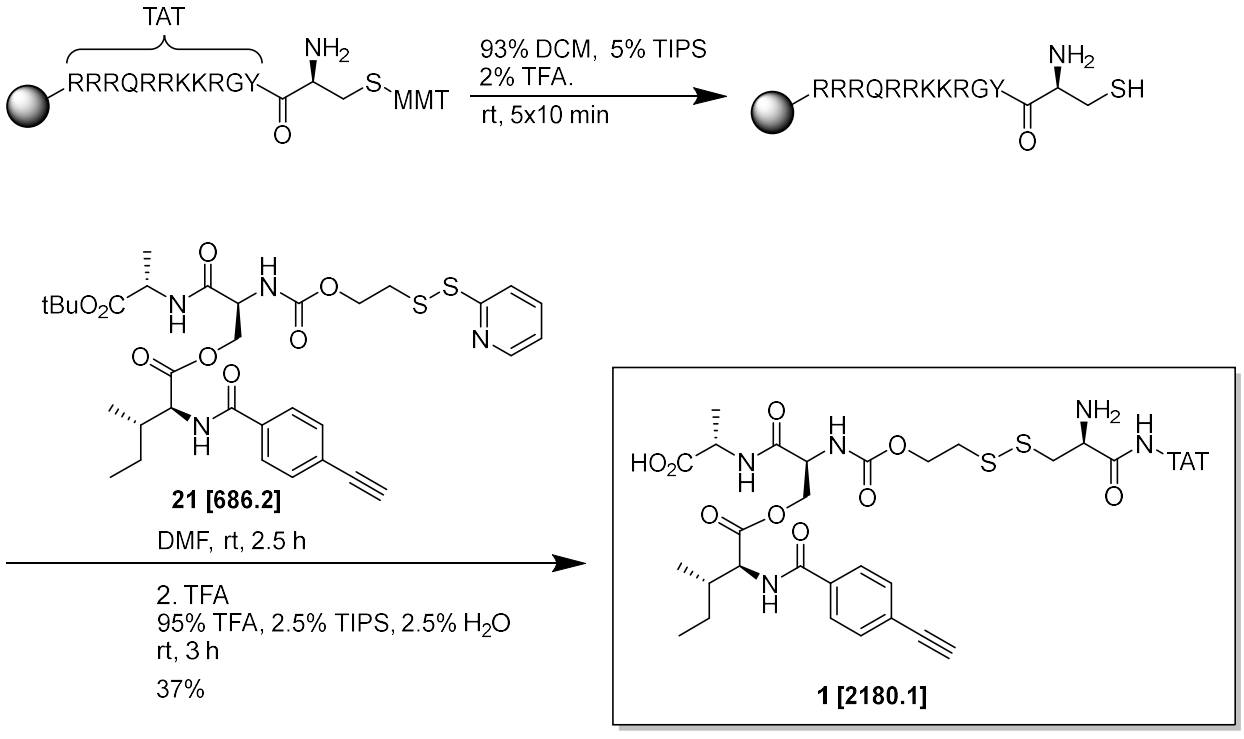

Scheme 8: Synthesis of isopeptide-TAT-conjugate 1. SPPS of Cys-TAT followed by coupling to isopeptide **21**.

The final peptide was precipitated in cold diethylether and further purified by HPLC and subsequent lyophilisation resulting in 67 mg (37%) of a colourless solid that was further analysed by LC-MS (Figure 19) and MALDI-TOF mass spectrometry (Figure 20).

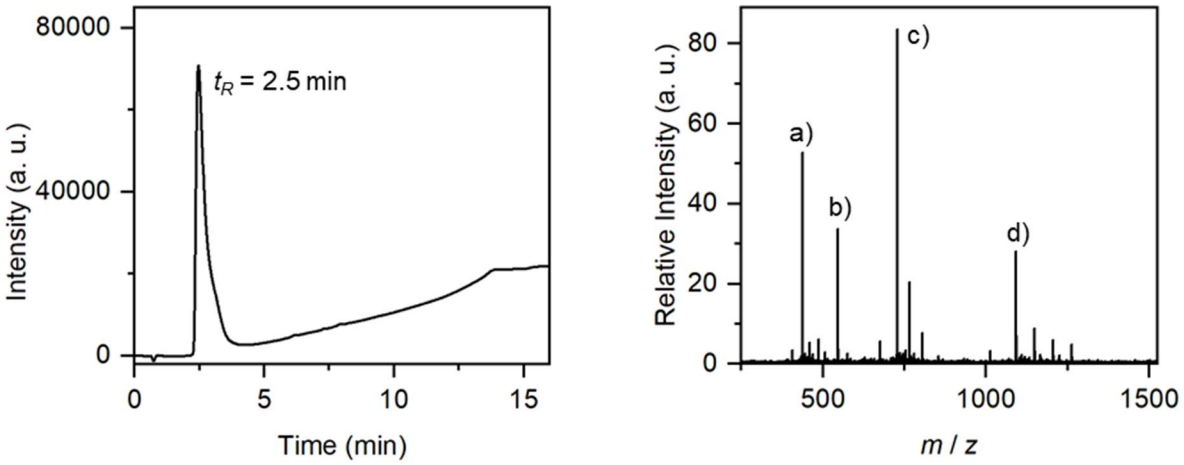

Figure 19: LCMS data of TAT derived isopeptide 1. LC elugram (left, detection at 254 nm) and corresponding mass data (right). a) 437.4 $[M + 5H]^{5+}$, b) 546.3 $[M + 4H]^{4+}$, c) 728.2 $[M + 3H]^{3+}$, d) 1091.7 $[M + 2H]^{2+}$.

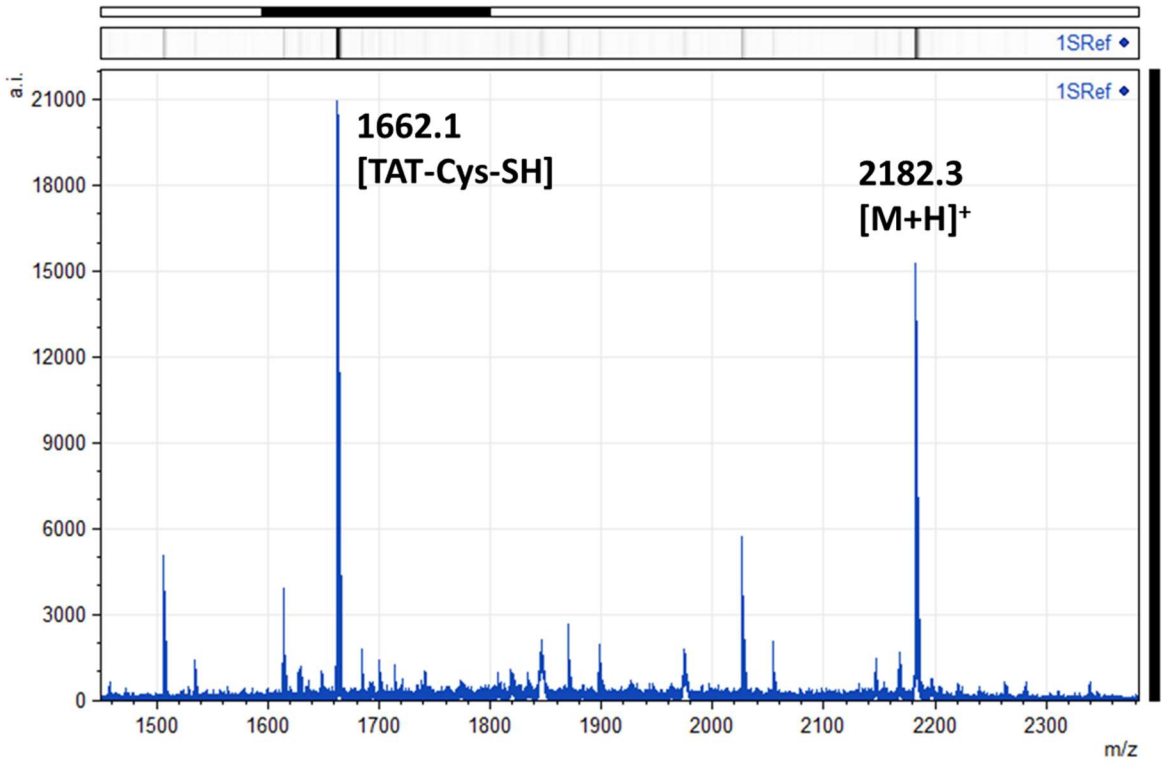

Figure 20: Maldi-ToF spectrum of TAT containing isopeptide 1.

3.3.3 Synthesis of Iso-ISA-Alkyne-Pt-tpy-NMe_3^+

The stability of the isopeptide with the activated disulfide bond (**22**) towards typical complexation conditions was investigated with the Cl-Pt-tpy-NMe_3^+ complex **23** in the presence of CuI/DIPEA to activate and deprotonate the alkyne at elevated temperature in DMF (Scheme 9). After precipitation in cold ether and subsequent centrifugation and washing steps the LC-MS data showed extensive degradation of the disulfide bond. *Via* additional reaction with 4,4'-dithiodipyridine, the desired product could not be regenerated as the free thiol is degrading further under the formation of an oxathiolanone.

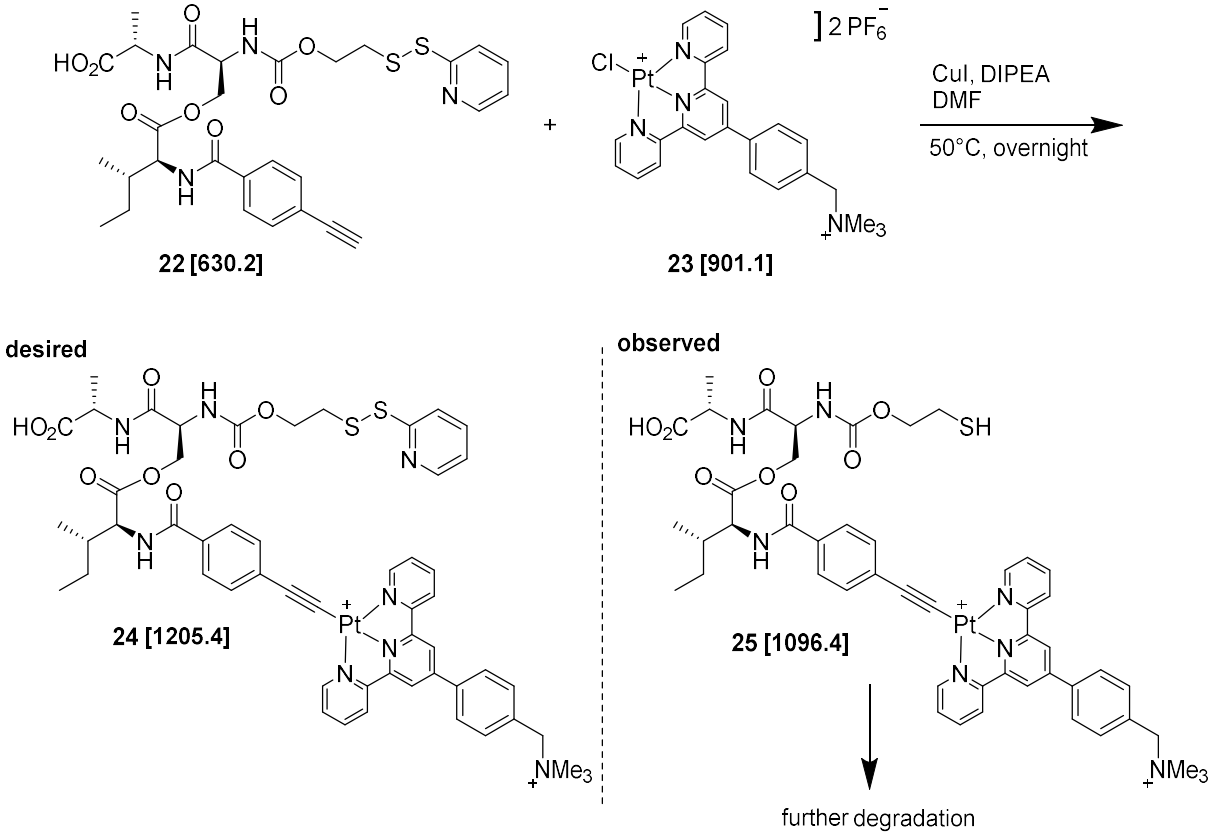

Scheme 9: Complexation experiment with the isopeptide with activated disulfide bond (22). Desired and observed product of reaction with Cl-Pt-tpy-NMe_3^+ complex (**23**). The free thiol will undergo a cyclization reaction resulting in a free amino group and 1,3-oxathiolan-2-one.

As the stability of the disulfide bond is expected to increase after the attachment of the TAT sequence (**1**) the cell-penetrating sequence was coupled to the isopeptide before the follow-up experiment (Scheme 10). The complexation indicated positive results in LC-MS analytic, however the conditions need to be further optimized. 2.4 mg (10%

yield) of the complex **26** could be isolated by analytical HPLC and analyzed by LC-MS (Figure 21).

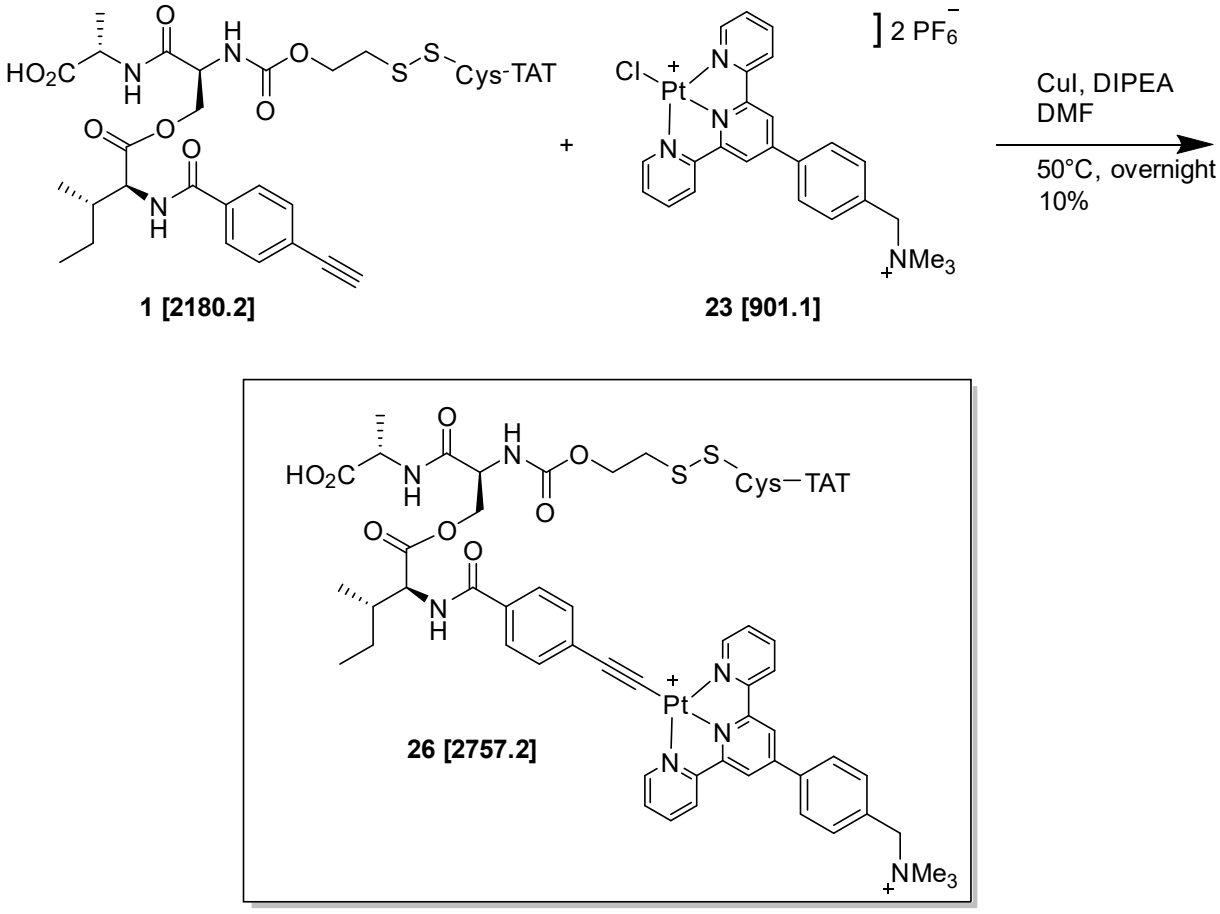

Scheme 10: Complexation of the TAT conjugated depipeptide with Cl-Pt-tpy-NMe$_3^+$(26).

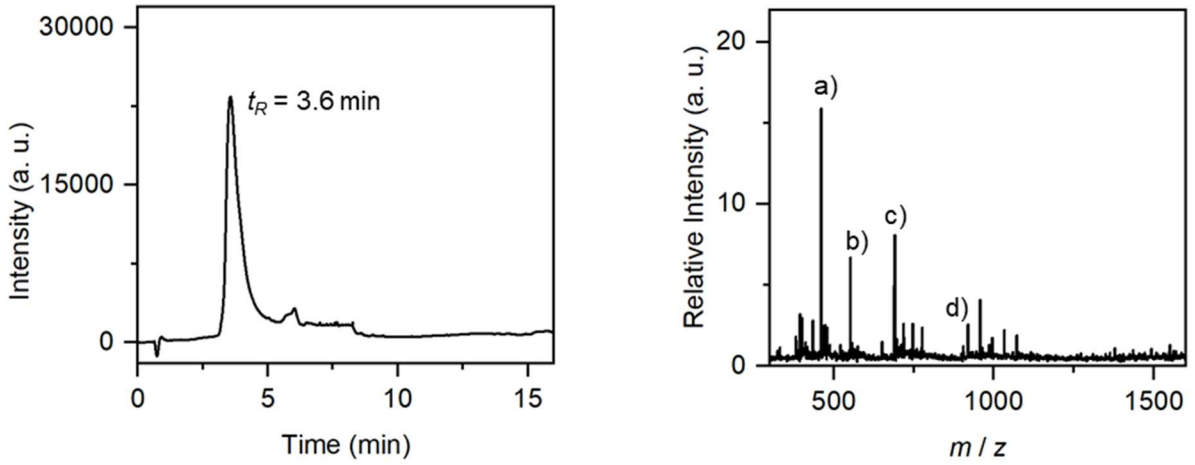

Figure 21: LCMS data of TAT containing complex 26. LC elugram (left) and corresponding mass data (right). a) $[M+4H]^{6+}$=460.3, b) $[M+3H]^{5+}$=551.8, c) $[M+2H]^{4+}$=690.1, d) $[M+H]^{3+}$=918.6.

3.3.4 HPLC Kinetic Analysis of Glutathione-induced Degradation of Isopeptide

To gain information on the kinetics of the glutathione-induced degradation of the isopeptide Pt (II) complex, a series of analytical HPLC measurements were conducted in a chronological sequence (Figure 22, bottom). For this purpose, the isopeptide complex (**26**) was dissolved in 50 mM NH_4CO_3 buffer that either did or did not contain glutathione. To simulate the intracellular glutathione levels and the reducing environment of the cytosol, the first sample contained 1 mM of reduced glutathione (GSH). The mixed sample was shaken at room temperature while over the course of the analysis 10 µl samples of the solution were injected into the analytical HPLC at distinct time points. The exact experimental set up is shown in chapter 5 and the reaction scheme is shown in Figure 22 (top).

The elugrams of the sample with an intracellular concentration of GSH show the degradation process of **26** (t_R = 10.3 min) over time (Figure 22). Upon addition of the reducing agent, the disulfide cleavage takes place immediately which is shown by the signals of the intermediate **27** (t_R = 14.7–15.1 min). After 20 min a small peak at an elution time of t_R = 11.3 min indicates the further degradation resulting in the free isopeptide **28**. The amount of **28** reaches its maximum after one hour and decays over the following hours. After 7 hours, only the signal of the final product (**29**, t_R = 12.4 min) could be observed. The presented data shows that the starting material (**26**) showed a complete conversion to the linear complex **29** within a 7-hour time frame.
Besides these fruitful findings, the discussed kinetic data also shows an impurity (t_R = 10.0 min) in the starting material that also reacts with GSH resulting in a peak with a corresponding elution time of 7.0 min. The impurity could be unreacted precursor complex (**23**) that undergoes ligand exchange reaction resulting in the GSH attached complex.

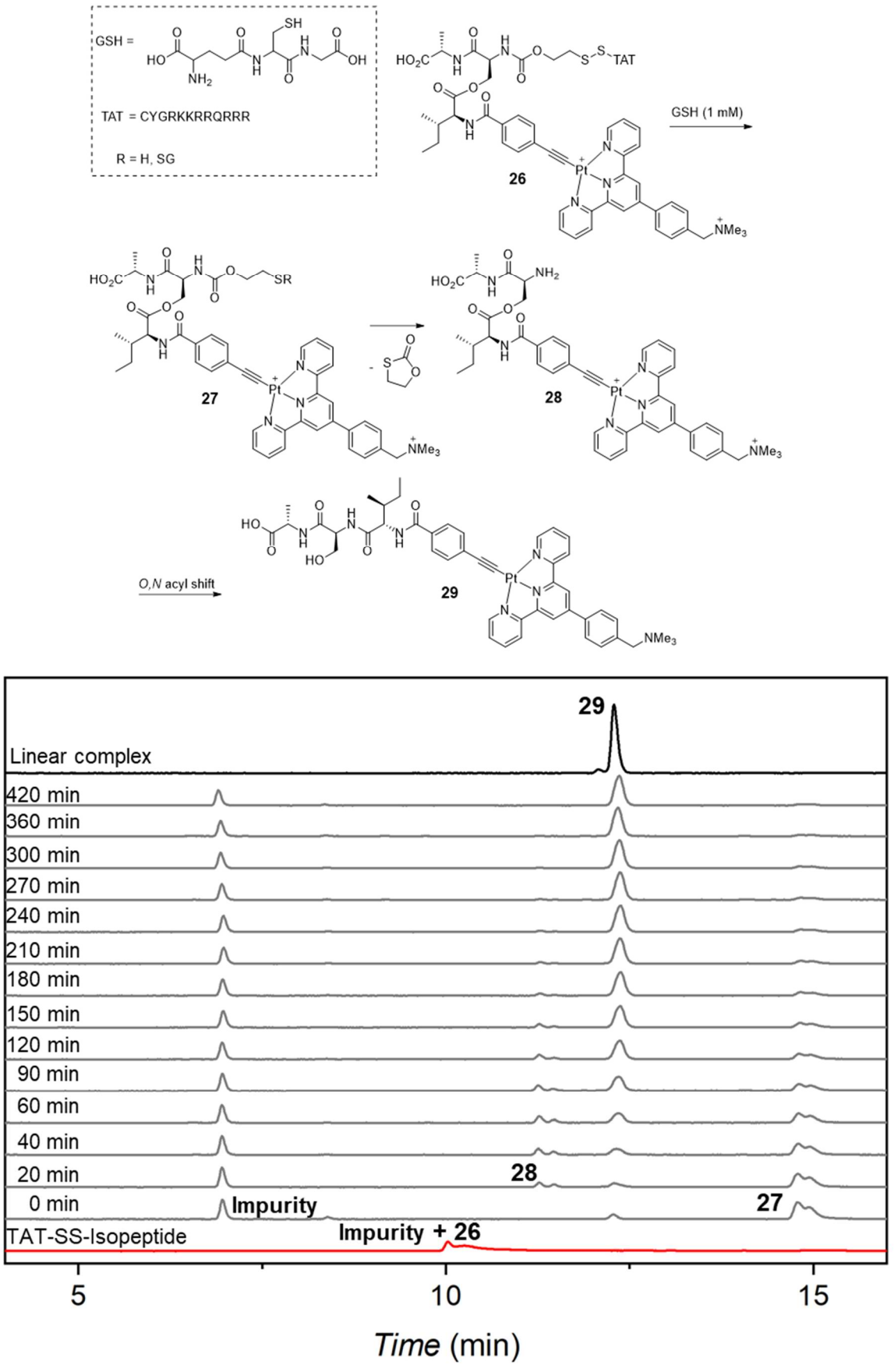

Figure 22: Analysis of glutathione-induced degradation of 26 by analytical HPLC. Reaction scheme of cleavage and self-immolation of the trigger group, followed by subsequent rearrangement (top). Degradation of 26 (t_R = 10.3 min) at intracellular levels of glutathione ([GSH] =1 mM).

3.3.5 Optical Properties of TAT-containing Pt (II) complex

To survey the optical properties of the TAT-containing isopeptide in complexation with the Platinum (II) core (**26**), UV/Vis absorption and luminescence emission spectra were recorded and compared to the data of the linearized complex **29**. Correlation of the absorption bands to the associated charge transfer processes is analogue to chapter 3.1.3. The absorption band at ca. 460 nm can be attributed to a combination of *d*π(Pt)→π*(tpy) MLCT and LLCT interactions between the alkynyl and the terpyridine ligands and the shoulder centered at ca. 590 nm is assigned to metal-metal-to-ligand charge-transfer (MMLCT) transitions.[26,60] Comparing these MMLCT shoulders, **29** exhibits a stronger band, indicating a higher extend of intermolecular dz^2 interactions between the metal centers of neighboring molecules. Upon excitation at 488 nm, the complexes both show a NIR emission originating from the MMLCT excited states. However, when compared to each other, the emission of the isopeptide variant (**26**) is shifted hypsochromic to 779 nm, while the emission of the linearized pendant (**29**) is centered at 793 nm. This can also be ascribed to the weaker MMLCT interactions of the kinked isopeptide complex (**26**) in comparison to the linearized complex (**29**). For the emission experiments, different slit sizes in the photometer were used. That is why the intensity of the luminescence cannot be compared, even though an increase in emission of **29** is expected due to stronger MMLCT transitions.

However, the difference in photophysical properties of the two complexes exemplifies the suitability of the design for the tracking of the GSH-induced conversion and subsequent self-assembly.

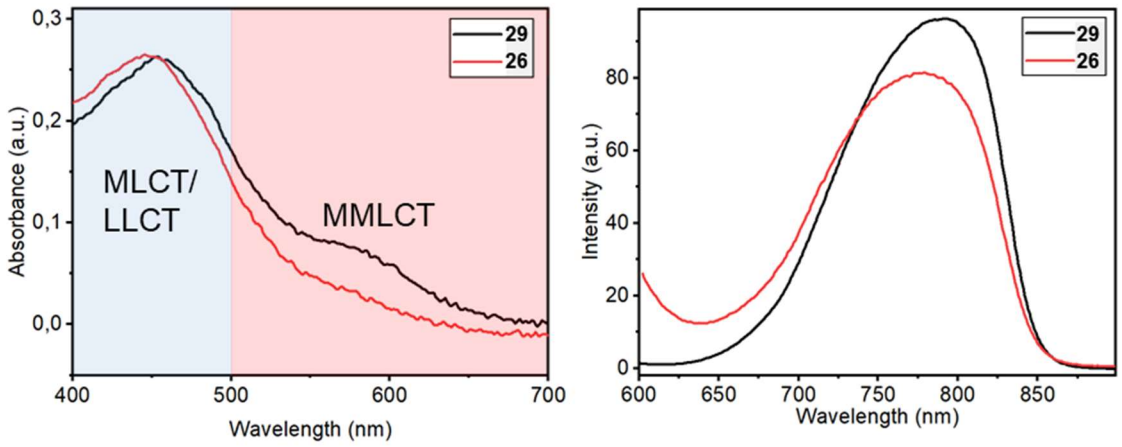

Figure 23: UV/Vis absorption and luminescence emission spectra of platinum (II) complexes 26 and 29. 50 µM in DPBS (1% DMSO). Excitation wavelength for emission 488 nm. Data of **29** can also be found in publication[27].

3.3.5 Cellular Uptake Studies with TAT-SS-Isopeptide-Pt (II) Complex

The TAT sequence facilitates cellular uptake[64] and was therefore implemented in the molecular design. To verify the cellular uptake and investigate the distribution of compound **26** within the cells, confocal laser scanning microscopy was conducted. A549 lung alveolar adenocarcinoma cells were incubated for 4 h with the complex in 25 µM and 10 µM concentrations respectively. Additionally, the nuclei were stained with Hoechst-dye and membranes were visualized with Cell Mask Deep Red.

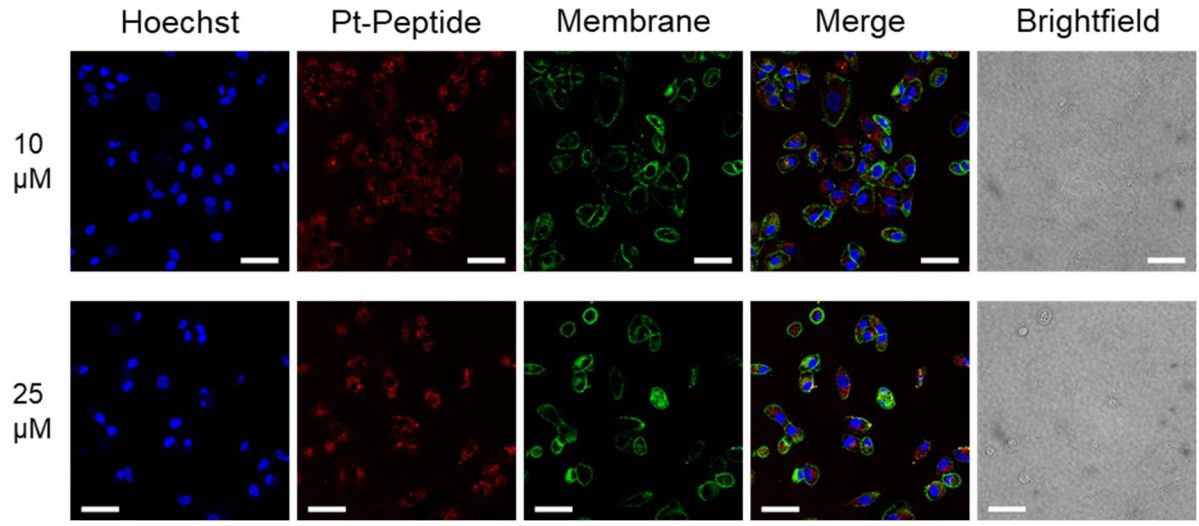

Figure 24: Internalization and intracellular self-assembly of 26. Visualized by confocal laser scanning micrographs of A549 cells treated for 4 h with **26** (25 µM and 10 µM), Hoechst Dye and Cell Mask Deep Red Dye. Scale bars = 50 µm. Processed with Icy Software.

Both screened concentrations display emission in the NIR window that can be attributed to the aggregating Pt complexes, which indicates successful cellular uptake. This observation contrasts the lack of structure formation within the TEM studies with 25 and 10 µM concentrations. The reason for this could be an increase in concentration due to compartmentalization during the uptake. Moreover, the structures appear distributed throughout the cell and not mainly localized in proximity of the nucleus as described for boronic acid based pendants.[26] This indicates a difference in the uptake process. While the previous trigger system was first activated within the acidic pH of the endocytic pathway, the herein presented group self immolates upon reduction of the linker by GSH in the cytosol. In addition to that, the toxicity of the GSH-responsive molecule appears significantly lower as the cells after 4 h are still largely alive, although they display some signs of cellular stress with observable rounding (compare Figure 24).

4 Summary and Outlook

The aim of this project was the synthesis of GSH and photoresponsive peptide sequences and the further analysis of their degradation behavior. Furthermore, Pt (II) conjugates of the described motifs should be prepared and analyzed regarding their self-assembly behavior. To achieve this, a linear Pt (II) containing peptide was prepared and analyzed *via* TEM. The amino acid subunits were tailored to provide propensity towards assembly without preventing sufficient solubility. After the proof of concept with the linear peptide conjugate, two stimuli-responsive concepts were scrutinized. A thio-coumarin photoprotective group, possessing an absorption maximum at 470 nm, was synthesized, and attached to the KFN tripeptide that was further functionalized with a platinum binding terpyridine ligand at the *N*-terminus. The photodynamic behavior of this photoprotected sequence was screened with UV/Vis and LCMS approaches. On the other hand, a glutathione-responsive precursor undergoing a multistep cascade reaction when exposed to intracellular concentrations of GSH was designed. Utilizing a serine ester bond in an isopeptide approach, the ISA tripeptide was equipped with a “kink” circumventing the aggregation. Upon reduction of the disulfide, the linker system self-immolates, freeing the *N*-terminus of the serine. The system stabilizes *via O,N* acyl shift resulting in a linearized sequence. Further functionalization with an alkyne moiety, enabled attachment to a platinum (II) complex. Moreover, the cell-penetrating TAT sequence was introduced into the molecule at the disulfide site. The degradation kinetics of this system in GSH containing buffer (*c* = 1 mM) were analyzed by analytical HPLC. The data showed an almost instantaneous decay of the disulfide bridge, which is in accordance to previous findings of comparable systems.[44] The linker then self-immolates freeing the *N*-terminus of the serine over the course of approximately five hours. Free isopeptide then steadily linearizes to the final product, indicated by a constant ratio of isopeptide and increasing product peak. Next up, preliminary cellular studies were conducted to screen celluar uptake and keep track of the impact of the compound on cells. A549 cells were incubated for four hours with 10 and 25 μM sample concentrations respectively. Nuclei and membranes were stained additionally, and confocal laser scanning microscopy was performed. By tracking the NIR-emission of the aggregating Pt (II) (tpy) complex, cellular uptake could be evidenced. The compound appeared to be localized within the cytosol. The cells did not display major signs of cell death within this time frame, however rounded shape

indicated a certain level of stress. The emergence of the NIR-emission proves the formation of intracellular structures even with low concentrations where TEM did not supply sufficient imaging.

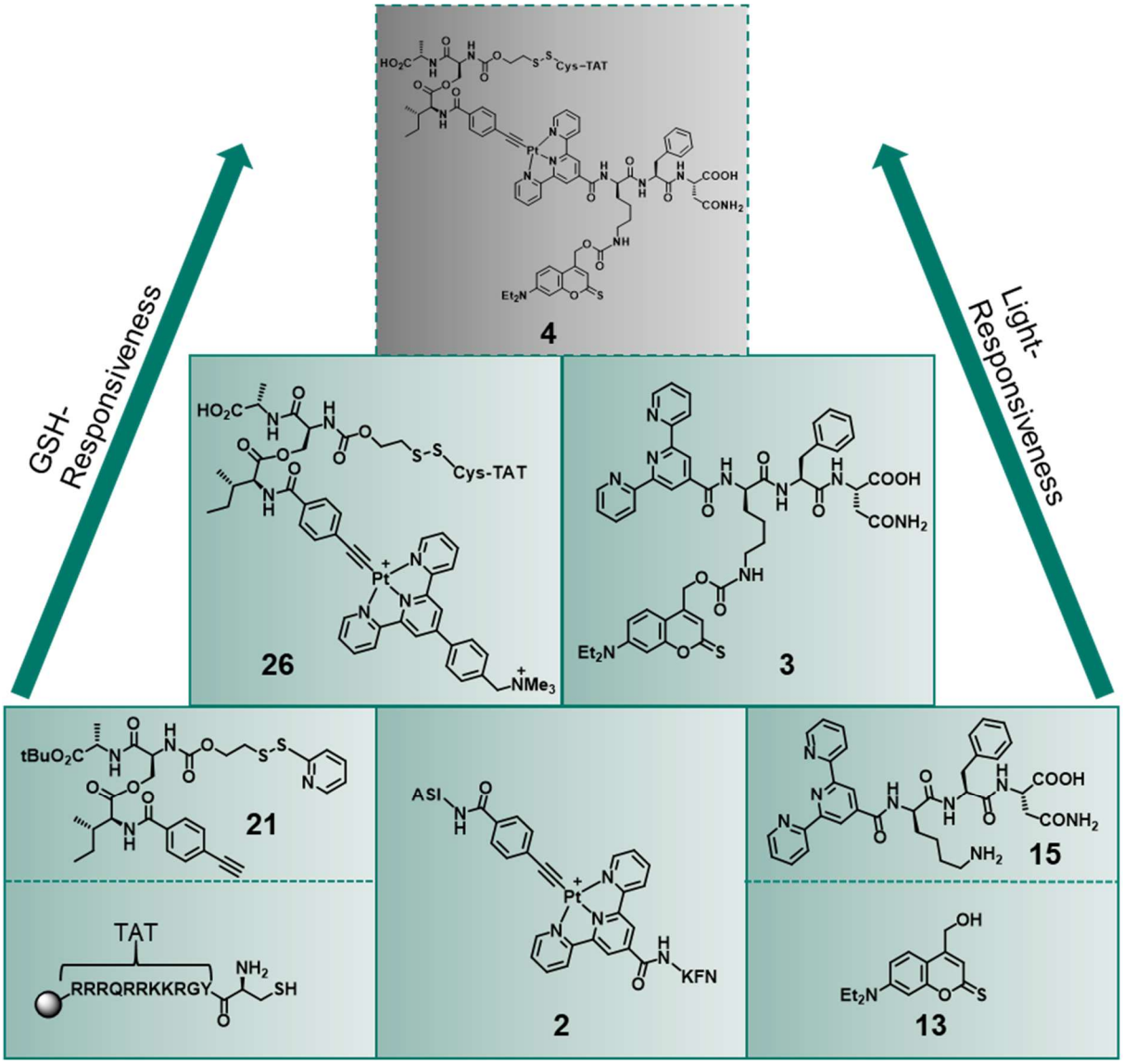

Figure 25: Synthetic Summary. SPPS-synthesis of Cys-Tat followed by disulfide coupling to alkyne-functionalized iso-ISA (**21**) and complexation to Pt (II) precursor (**26**, left, GSH-responsiveness). Synthesis of thio-coumarin (**13**) and attachment to tpy-KFN tripeptide **15** (**3**, right, light-responsiveness). Platinum (II) complex of ISA-alkyne and tpy-KFN (**2**). Dual-responsive platinum (II) complex (**4**, not realized, top in grey).

The next step would be the fusion of both parts into a dual responsive platinum-based peptide that provides spatiotemporal control over the superstructure formation while being traceable with the intrinsic NIR-emission. Although the individual components were successfully prepared, this final step could not be realized within the time frame of this project. This is therefore the focus of future studies. After the synthesis of this

complex, interesting studies regarding the photodynamic behavior of the target molecule can be conducted as the platinum terpyridine complex as well as the coumarin PPG express an absorption band at ca. 470 nm. Additionally, aggregation studies and analyses of the photochemical properties of the precursor molecules will be performed. Focusing on the biological application, cellular uptake, cytotoxicity, and the effect on metabolism can be analyzed. Correlations between the morphology of the assemblies and their biological effects can be drawn to guide future design strategies.

Within this project, first insights into the degradation behavior of the stimuli-responsive chemical groups were achieved. However, the intermediates of both processes, especially when combined, are not described yet. After scrutinizing the combination of GSH and light responsiveness, combinations of other trigger systems could be screened. An obvious candidate is the replacement of the disulfide trigger by the ROS-specific boronic acids that were already described in the context of platinum complexes before.[26] The coalescence of extrinsic and intrinsic stimuli however should be conserved, as this provides precise spatiotemporal control over the aggregation behavior. Variations in the PPG segment include the further functionalization of the coumarin group. For instance the aniline ethyl groups can be used to attach more complex structures that influence the intermolecular interactions dramatically.[61]

Summarized, the herein described Pt (II) (tpy) moiety represents an intricate platform for a multitude of future experiments in the field of supramolecular chemistry, synthetic biology, and nanomedicine.

5 Experimental Part

5.1 Analytical Instruments and Methods

Reagents and solvents were purchased from commercial sources and were used without further purification. Peptide Synthesis grade reagents were used for synthesizing the peptides. HPLC was performed using CH_3CN in HPLC grade and H_2O for HPLC and reactions was obtained from a Millipore purification system

NMR-Spectroscopy

^{1}H- and ^{13}C-NMR-measurements were conducted at DRX 250-, AVANCE 300-, AVANCE 700-Spectrometers by Bruker at 278 K or 310 K in deuterated solvents. Internal standard was set depending on the used solvent. Samples containing water were measured with water-suppression. The data was processed with the software *MestReNova* by Mestrelab. Chemical shift δ was indicated in part per million (ppm). Multiplets were abbreviated as s=singlet, d=doublet, t=triplet, q=quartet, m=multiplet.

HPLC

Peptides were purified by preparative HPLC using a setup by Shimadzu. For purification, a Phenomenex Gemini 5 µm NX-C18 110 Å 150 × 30 mm was used at a flowrate of 25 mL/min. All measurements and purification steps were done using gradients of acetonitrile and MilliQ water, each acidified with 0.1% TFA. Absorbance was recorded at 214 and 254 nm wavelength. The software LabSolutions by Shimadzu and Powerpoint were used to process all HPLC spectra.

For analytical measurements an Atlantis T3 column (4.6 × 100 mm, 5 µm) was used at a flowrate of 1 ml/min, except for analysis of cell lysates where a ZORBAX Eclipse, XDB-C18, 80Å, 5 µm, 4.6 × 250 mm column was used at a flowrate of 1mL/min. All measurements and purification steps were done using gradients of acetonitrile and MilliQ water, each acidified with 0.1% TFA. Absorbance was recorded at 190, 214, 254 and 433 nm wavelength. The software LabSolutions by Shimadzu and PowerPoint were used to process all HPLC spectra.

Solid-Phase Peptide Synthesis

For the peptide synthesis, a LibertyBlue automated microwave synthesizer by CEM was used. The system was purged with DCM and piperidine was used for deprotection. Amino acids were dissolved in DMF and used inside 50 ml falcon tubes. DIC and Oxyma® were employed as coupling agents and therefore dissolved in DMF and used inside of glass vessels.

LC-MS

Compounds were analyzed by HPLC-ESI-MS on a LC-MS 2020 by Shimadzu using a Kinetex 2.6 µm EVO C18 100 Å LC 50 × 2.1 mm column. MilliQ water, acidified with 0.1% formic acid and acetonitrile were used as solvents for all measurements. The solvent gradient started with 5% ACN and 95% water, while the ACN content was linearly increased to 95% in 12 min. Data were processed in LabSolutions and Powerpoint.

TEM

TEM pictures of peptide solutions were taken on a JEOL 1400 transmission electron microscope at a voltage of 120 kV. Samples were prepared on Formvar/carbon-film coated copper grids (300 mesh) by Plano GmbH. To prepare the TEM grids, 3 µl of peptidesolution were put on freshly etched (30 s at 20% oxygen content) Formvar coated copper grids. After 5 min the solution was removed using a filter paper and grids were stained with uranyl acetate 4% for 2.5 min. The grids were washed three times with MilliQ water and dried before measuring. TEM images were processed in ImageJ.

Cell Culture

A549 cells were cultured at 37 °C and 5% CO2 in Dulbecco's Modified Eagle's Medium (DMEM, high glucose), supplemented with 10% FBS. Cell lines were cultured in T75 culture flask and subcultivated two to three times per week.

Confocal Laser Scanning Microscopy

Cellular uptake studies of A549 cells were seeded at a density of 25,000 cells/well in an 8-well confocal plate. After adhering for 24 h, cells were treated with the sample for 4 h at 37 °C. The sample was dissolved in DPBS in concentrations of 50 and 125 µM and further diluted with DPBS to a final volume of 40 µl. Sample solutions were further diluted 1:4 with DMEM and added to the cells, after removing the existing medium from the wells. After the incubation time was over, cells were stained with CellMask Deep Red (Invitrogen) according to manufacturer's protocol. The staining solution was removed, and DMEM Medium was added to the cells before they were imaged by confocal laser scanning microscopy. Confocal images of cells were taken on a Leica Stellaris 8 FALCON / DLS. To monitor the Pt (II) complex and the membrane stain, a white light laser, with excitation at 488 nm and 640 nm, was used with an emission filter from 650–800 nm.

Nanodrop

The UV/Vis absorption spectra for the solutions of the compounds were recorded on a Thermo Scientific™ NanoDrop 2000/2000c spectrophotometer in a Hellma high precision quartz cell, 10 × 10 mm light path. The luminescence emission spectra for the solutions of the compounds were recorded on a Cary Eclipse fluorescence/luminescence spectrophotometer in a Hellma high precision quartz cell, 10 × 10 mm light path. For the analysis of light-induced conversion from **3** to **15**, Compound **3** was dissolved in ACN at a concentration of 200 µM before diluting to desired concentrations using DPBS (pH 7.4, 50 mM) and ACN. The cuvette was placed in 3 cm distance of the light source and irradiated at the indicated time intervals (10, 20, 30, 60, 90, 120, 180 s).

MALDI-TOF

MALDI-TOF spectra were recorded on either a rapifleX MALDI-TOF/TOF from Bruker or MALDI Synapt G2-SI from Waters. Samples were mixed with a saturated solution of the matrix S7 α-cyano-4-hydroxycinnamic acid (CHCA) in water/ACN 1/1 + 0.1% TFA. Data processing was performed in mMass.

5.2 Small Molecules in Solution

JL26+JL27, JL31, JL35 – ASI-alkyne-Pt-tpy-KFN

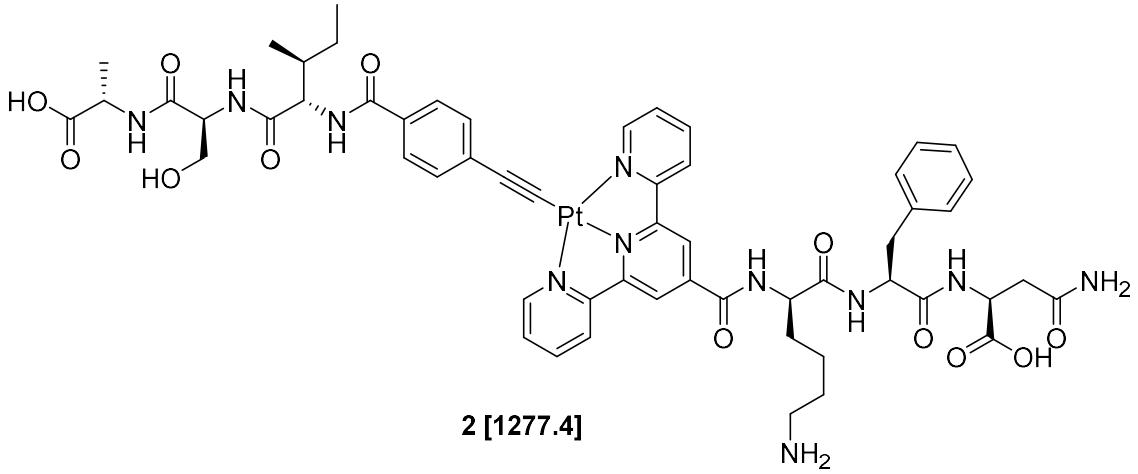

2 [1277.4]

a) JL26+JL27

Tpy-KFN (**15**, estimated two eq. of TFA attached; 8.6 mg, 9.6 µmol) and $PtCl_2(COD)_2$ (4.3 mg, 11.4 µmol) were dissolved in 5 ml DMF in an Ar-atmosphere and refluxed overnight. The solution was precipitated in cold ether, centrifuged (4000 rpm, 3 min) and decanted. The dark red residue was then dissolved in 5 ml DMF and ASI-alkyne **5** (11.5 mg, 27.6 µmol), DIPEA (36 µl, 210.9 µmol) and CuI (tip of spatula) were added. Three Freeze-Pump-Thaw-Cycles were conducted, and the solution was stirred at 50°C overnight. Then, the solution was precipitated in cold ether, centrifuged (4000 rpm, 3 min) and decanted. The LCMS data did not show signals corresponding to the product.

b) JL31

Tpy-KFN (**15**, estimated one eq. of H_2CO_3 attached; 9.9 mg, 13.2 µmol) and $PtCl_2(dmso)_2$ (5.8 mg, 13.7 µmol) were dissolved in 5 ml DMF in an Ar-atmosphere and refluxed overnight. The solution was precipitated in cold ether, centrifuged (4000 rpm, 3 min) and decanted. The dark red residue was then dissolved in 5 ml DMF and ASI-alkyne **5** (4.2 mg, 10.0 µmol), DIPEA (13 µl, 78.4 µmol) and CuI (tip of spatula) were added. Three Freeze-Pump-Thaw-Cycles were conducted, and the solution was stirred at 50°C overnight. Then, the solution was precipitated in cold ether,

centrifuged (4000 rpm, 3 min) and decanted. The LCMS data did not show signals corresponding to the product.

c) JL35

Fmoc-KFN-tpy (**6**, 12 mg, 12 µmol) and $PtCl_2(dmso)_2$ (5.5 mg, 12.0 µmol) were dissolved in 20 ml of a 1:1 mixture of MeOH and DCM. The solution was refluxed overnight, precipitated in cold ether, centrifuged (4000 rpm, 3 min) and decanted. The dark orange residue was dissolved in 10 ml DMF and alkyne-ISA (**5**, 15 mg, 35.9 µmol), DIPEA (10 µl, 129.1 µmol) and CuI (tip of spatula) were added. Three Freeze-Pump-Thaw-Cycles were conducted, and the solution was stirred at 50°C overnight. Then, the solution was precipitated in cold ether, centrifuged (4000 rpm, 3 min) and decanted. The residue was dissolved in 4 ml DMF and 1 ml Piperidine was added. The solution was stirred at room temperature for 10 min and the solvent was removed under reduced pressure. The residue was further purified by HPLC yielding a red-brown solid (2.7 mg, 1.8 µmol, 15% yield).

LCMS: (1277.4 g/mol): m/z = 639.5 $[M + H]^{2+}$, 852.5 $[2M + H]^{3+}$, 1277.5 $[M]^{+}$.

NMR: NMR experiments were not conducted, as the isolated amount of product was considered insufficient.

JL46, JL48 – tpy-KFN-coumarin

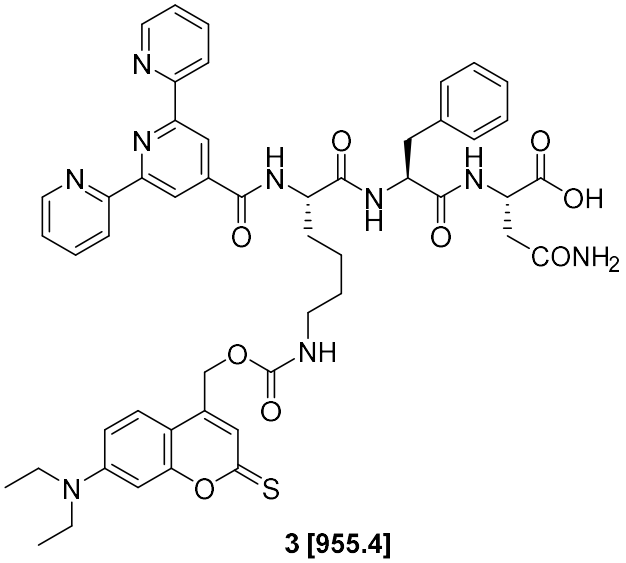

3 [955.4]

DMAP (16 mg, 132 µmol), DIPEA (102 µl, 599.8 µmol) and tpy-KFN **8** (estimation of two attached TFA molecules, 80.5 mg, 89.9 µmol) were partially dissolved in 5 ml DMF and added to the reaction mixture containing the coumarin carbonate **17** in DCM. The suspension was stirred at room temperature in the dark overnight. The solvent was evaporated under reduced pressure and the crude product was further purified by HPLC and lyophilization resulting in 4 mg (4.2 µmol, 7% yield) of an orange colored solid.

LCMS: (955.4 g/mol): *m*/*z* = 479.0 $[M + 2H]^{2+}$, 956.6 $[M + H]^{+}$.

JL33, JL34 – Fmoc-KFN-tpy

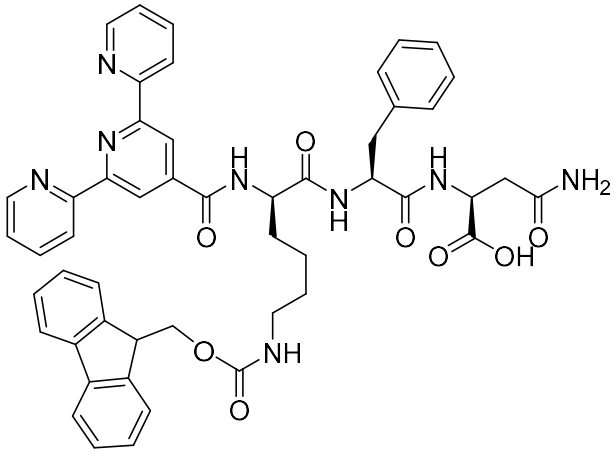

6 [888.3]

Tpy-KFN (98 mg, 147 µmol), Fmoc-OSU (57 mg, 169 µmol) and Na_2CO_3 (19 mg, 179 µmol) were dissolved in 80 ml of a 1:1 water/dioxane mixture at 0°C and stirred at ambient temperatures for 2 days. After LCMS analysis additional Fmoc-OSU (56 mg, 166 µmol) and Na_2CO_3 (23 mg, 217 µmol) were added, and the solution was stirred overnight. Dioxane was removed under reduced pressure and the aqueous phase was washed with EA (3x 50 ml) and DCM (2x 50 ml). The aqueous phase was lyophilized resulting in a pink solid (155 mg) that was further purified by HPLC resulting in a pink solid (12 mg, 13.5 µmol, 10% yield).

LCMS: (888.3 g/mol): *m*/*z* = 889.5 $[M + H]^+$, 911.5 $[M + Na]^+$.

JL24 – Coumarin enamine

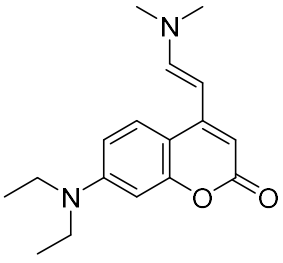

8 [286.2]

7-(Diethylamino)-4-methylcoumarin (**7**, 5.0 g, 21.65 mmol) was dissolved in 20 ml DMF and DMF-DMA (5.8 ml, 86.47 mmol) was added. The solution was refluxed overnight, diluted with DCM, and washed with saturated $NaHCO_3$ solution (3x 50 ml) and water (2x 50 ml). The organic phase was dried over $MgSO_4$, filtered and the

solvent was evaporated under reduced pressure. The brown residue (ca. 6 g) was purified by silica gel column chromatography (7:3 DCM/ ethyl acetate) resulting in a brown solid (1.3 g, 4.55 mmol, 21% yield). Additionally, a red fraction (1,0 g) and an orange fraction (2.2 g) were collected. The red fraction corresponds to hydrolyzed product and the orange fraction showed similar NMR signals to the brown solid.

R_f (7:3 DCM/EA, on silica): 0.5

NMR: ^{1}H NMR (300 MHz, $CDCl_3$) δ 7.52 (d, 1H), 7.21 (d, 1H), 6.59 – 6.45 (m, 2H), 5.84 (s, 1H), 5.32 – 5.16 (m, 1H), 3.39 (q, 4H), 2.98 (s, 6H), 1.19 (t, 6H).

JL29 – Coumarin aldehyde

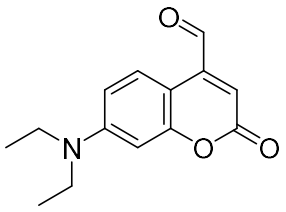

9 [245.1]

Coumarin **11** (1.3 g, 4.54 mmol) was dissolved in 35 ml of a 1:1 mixture of water and THF and $NaIO_4$ (2.9 g, 13.61 mmol) was added. The solution was stirred for 4.5 h at room temperature. Then, the precipitate was filtered off and washed with EA. The filtrate was extracted with saturated $NaHCO_3$ solution (3x 50 ml) and the organic phase was dried over $MgSO_4$, filtered and the solvent was removed under reduced pressure resulting in a dark red residue (0.92 g, 3.75 mmol, 83% yield) that was used in the next step without further purification.

NMR: ^{1}H NMR (300 MHz, $CDCl_3$) δ 10.03 (s, 1H), 8.30 (d, 1H), 6.63 (dd, 1H), 6.52 (d, 1H), 6.45 (s, 1H), 3.43 (q, 4H), 1.22 (t, 6H).

^{13}C NMR (75 MHz, $CDCl_3$) δ 192.67, 127.17, 117.46, 109.66, 97.75, 44.93, 12.58.

LCMS: (245.1 g/mol): *m*/*z* = 246.1 $[M + H]^+$.

JL30 – Coumarin alcohol

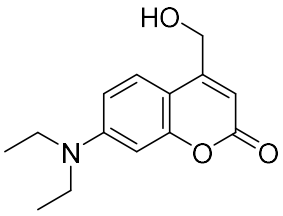

10 [247.1]

Coumarin **9** (460 mg, 1.88 mmol) was dissolved in 10 ml THF, cooled to 0°C and $NaBH_4$ (160 mg, 4.23 mmol) was added. The solution was stirred for 5 h at ambient temperatures, diluted with DCM and extracted with saturated $NaHCO_3$ solution (2x 50 ml). The organic phase was dried over $MgSO_4$, filtered and the solvent was removed under reduced pressure resulting in a yellow-brow solid.

NMR: ^{1}H NMR (300 MHz, $CDCl_3$) δ 7.25 (d, 1H), 6.49 (dd, 1H), 6.43 (d, 1H), 6.19 (d, 1H), 4.76 (d, 2H), 3.33 (q, 4H), 2.29 (s, 1H), 1.13 (t, 6H).

LCMS: (247.1 g/mol): *m*/*z* = 248.1 $[M + H]^+$, 495.3 $[2M + H]^+$.

JL15, JL19 – Protection of Coumarin alcohol

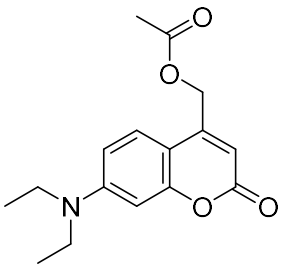

11 [289.1]

The coumarin alcohol **10** (40 mg, 0.162 mmol) was dissolved in DCM in an Ar-atmosphere and acetic acid (0.019 ml, 0.324 mmol) and DMAP (10 mg, 0.081 mmol) was added. Then, DIC (0.05 ml, 0.324 mmol) was added, and the reaction was stirred at ambient temperature overnight in the dark. The mixture was washed with brine (2x 20 ml) and water (2x 20 ml), the organic phase was dried over $MgSO_4$, filtered and the solvent was removed under reduced pressure. The residue (115 mg) was further purified by silica gel column chromatography (2:1 cyclohexane/ ethyl acetate) resulting in a yellow solid (37 mg, 0.128 mmol, 79% yield).

R_f (2:1 EA/Cy, on silica): 0.5

NMR: ^{1}H NMR (300 MHz, $CDCl_3$) δ 7.20 (d, 1H), 6.56 – 6.41 (m, 2H), 6.06 (d, 1H), 5.15 (d, 2H), 3.35 (q, 4H), 2.12 (s, 3H), 1.14 (t, 6H).

^{13}C NMR (75 MHz, $CDCl_3$) δ 124.51, 108.79, 106.61, 98.01, 61.49, 44.90, 20.90, 12.57.

LCMS: (289.1 g/mol): *m*/*z* = 290.1 $[M + H]^+$, 579.3 $[2M + H]^+$.

JL17, JL21 – Reaction with Lawesson's reagent

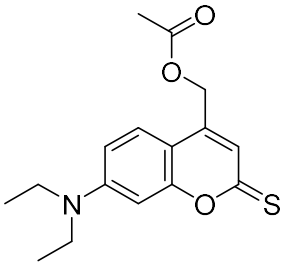

12 [305.1]

Coumarin **11** (180 mg, 0.622 mmol) and Lawesson's reagent (164 mg, 0.404 mmol) were dissolved in anhydrous toluene in an Ar-atmosphere. The solution was refluxed in the dark overnight. The solvent was removed under reduced pressure and the residue was further purified by silica gel column chromatography (3:1 cyclohexane/ ethyl acetate) resulting in an orange-brown solid (205 mg, 0.672 mmol, 100% yield).

R_f (99:1 DCM/Acetone, on silica): 0.8

LCMS: (305.1 g/mol): *m*/*z* = 306.1 $[M + H]^+$.

JL20, JL23 – Deprotection of JL17, JL23

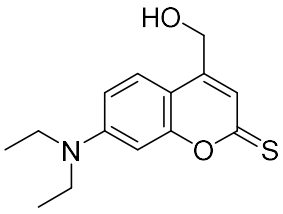

13 [263.1]

Coumarin **12** (190 mg, 0.622 mmol) was dissolved in ethanol that was dried over $MgSO_4$ for 2 days. HCl in ethyl acetate (1M, 2 ml, 2 mmol) was added and the solution was refluxed in the dark overnight. The solvent was removed under reduced pressure and the residue (310 mg) was purified by silica gel column chromatography (2:1 cyclohexane/ ethyl acetate) yielding an orange-brown solid (53 mg, 0.202 mmol, 32% yield).

R_f (3:1 EA/Cy, on silica): 0.3

NMR: ^{1}H NMR (300 MHz, d3-MeOD) δ 7.51 (d, 1H), 7.12 (d, 1H), 6.81 (dd, 1H), 6.67 (d, 1H), 4.75 (d, 1H), 3.50 (q, 4H), 3.35 (s, 2H), 1.22 (t, 6H).

LCMS: (263.1 g/mol): *m*/*z* = 264.1 $[M + H]^+$.

JL45, JL47 – Coumarin-(*p*-nitrophenyl)-carbonate

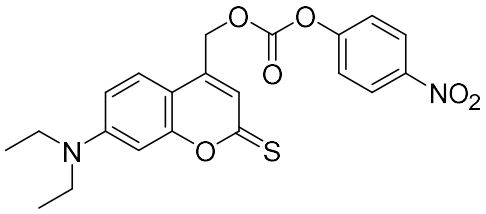

14 [428.1]

The thio-coumarin alcohol **13** (32.0 mg, 121.5 µmol) was dissolved in 10 ml DCM and DIPEA (206 µl, 1215 µmol) and 4-nitrophenyl carbonochloridate (36.7 mg, 182.3 µmol) were added. The solution was stirred at ambient temperature in the dark overnight and used for the follow up reaction without further purification.

LCMS: (428.1 g/mol): *m*/*z* = 429.1 $[M + H]^+$.

NMR: NMR experiments were not conducted, as the product was not isolated and used for the next step without purification.

JL03, JL13– (4-ethynylbenzoyl)-*L*-isoleucine

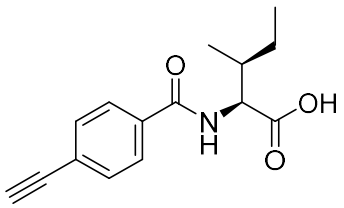

17 [259.1]

Fmoc-Ile-Wang-resin (0.70 loading, 2.416 g, 1.69 mmol) was swollen in DMF for 1 h. After filtration the resin was deprotected using 20% piperidine in DMF. After deprotection, the resin was transferred to a glass vial and 4-ethynylbenzoic acid (494.0 mg, 3.38 mmol), DIC (0.8 ml, 5.07 mmol) and Oxyma® (1441.0 mg, 10.14 mmol) were added in DMF. The mixture was shaken over night at room temperature. After filtration, the resin was washed with DMF and DCM, transferred into a glass vial and treated with 10 ml cleavage cocktail (95% TFA, 2.5% TIPS, 2.5% water) for 2 h while shaking. The resin was filtered and washed with DCM. The filtrate was evaporated under reduced pressure and the crude product was further purified by HPLC resulting in 264 mg (1.02 mmol, 60% yield) of a colorless solid.

LCMS: (259.1 g/mol): *m*/*z* = 260.1 $[M + H]^+$, 541.3 $[2M + Na]^+$.

NMR: ^{1}H NMR (300 MHz, $CDCl_3$) δ 7.75 (d, 2H), 7.56 (d, 2H), 6.65 (d, 1H), 4.82 (dd, 1H), 3.21 (s, 1H), 2.14 – 2.00 (m, 1H), 1.68 – 1.48 (m, 1H), 1.29 (ddt, 1H), 1.06 – 0.92 (m, 6H).

^{13}C NMR (75 MHz, $CDCl_3$) δ 175.73, 166.97, 133.88, 132.53, 127.21, 126.02, 82.78, 79.92, 57.07, 37.99, 25.39, 15.67, 11.75.

JL04, JL12, JL42 – Ser-SS-Py

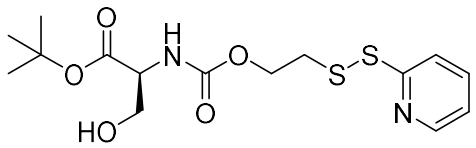

19 [374.1]

L-serine *tert*-butyl ester hydrochloride (200 mg, 1 mmol) and DIPEA (0.88 ml, 5 mmol) was dissolved in 10 ml of anhydrous DCM and degassed with Argon for two minutes. In a different flask, the reactive carbonate (495 mg, 1.3 mmol) was dissolved in 5 ml DCM and likewise degassed with Argon. Then the reactive carbonate solution was added to the Serine and stirred at ambient temperature overnight. The solution was diluted with ethyl acetate and washed with brine (2x 20 ml) and water (2x 20 ml). The organic phase was dried over $MgSO_4$, filtered and the solvent was evaporated under reduced pressure. The residue (582 mg) was further purified by silica gel column chromatography (1:1 ethyl acetate/ cyclohexane) resulting in a light-yellow oil (287 mg, 0.76 mmol, 76% yield)

R_f(1:1 EA/Cy, on Silica): 0.3

NMR: ^{1}H NMR (300 MHz, $CDCl_3$) δ 8.44 (d, 1H), 7.69 (dt, 2H), 7.16 – 7.06 (m, 1H), 6.90 (d, 1H), 5.60 (d, 1H), 4.41 (dt, 1H), 4.28 (q, 2H), 3.92 (d, 2H), 3.05 (tq, 2H), 1.49 (s, 9H).

^{13}C NMR (75 MHz, $CDCl_3$) δ 149.67, 137.40, 126.34, 121.07, 120.19, 115.82, 63.68, 56.78, 51.20, 37.70, 28.15.

LCMS: (374.1 g/mol): *m*/*z* = 375.1 $[M + H]^+$, 397.1 $[M + Na]^+$, 771.3 $[2M + Na]^+$.

JL05, JL07, JL16 – Alkyne-Ile-Ser-SS-Py

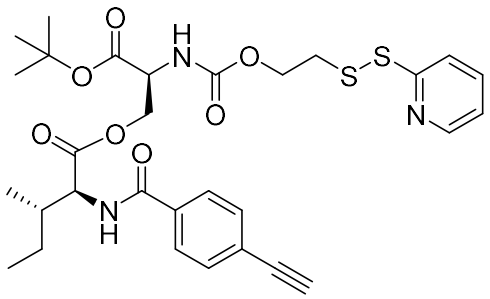

20 [615.2]

The alkyne **17** (41 mg, 0.16 mmol) was dissolved in 5 ml DCM and degassed with Argon. In a separate vial, the serine derivative **19** (30 mg, 0.08 mmol) was dissolved in 5 ml DCM and degassed with Argon. Then, both solutions were combined and DIC (0.05 ml, 0.31 mmol) and DMAP (9 mg, 0.07 mmol) were added. The solution was stirred at room temperature overnight. The solvent was removed under reduced pressure and the residue was purified by silica gel column chromatography (3:1 cyclohexane/ ethyl acetate) resulting in a yellow oil (34 mg, 70% yield).

R_f (3:1 Cy/EA, on silica): 0.3

NMR: ^{1}H NMR (300 MHz, $CDCl_3$) δ 8.47 (s, 1H), 7.82 – 7.73 (m, 2H), 7.66 (d, 2H), 7.55 (d, 2H), 7.09 (ddd, 1H), 6.60 (dd, 1H), 5.59 (d, 1H), 4.84 (ddd, 1H), 4.62 (d, 1H), 4.56 – 4.40 (m, 2H), 4.35 – 4.28 (m, 2H), 3.21 (d, 1H), 3.08 – 2.97 (m, 2H), 2.00 (s, 1H), 1.60 (s, 2H), 1.47 (d, 9H), 1.43 (d, 6H).

^{13}C NMR (75 MHz, $CDCl_3$) δ 149.87, 137.21, 132.49, 127.23, 122.04, 120.97, 119.99, 79.79, 65.36, 63.20, 57.10, 56.08, 38.79, 38.16, 37.79, 28.08, 27.06, 26.47, 25.45, 14.91, 11.91.

LCMS: (615.2 g/mol): *m*/*z* = 616.3 $[M + H]^+$, 638.3 $[M + Na]^+$.

JL06 – Deprotection of JL05, JL07, JL16

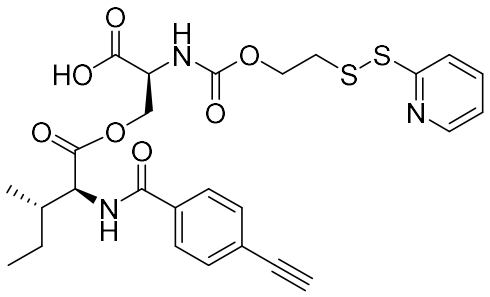

20B [559.1]

The protected peptide **20** (34 mg, 0.055 mmol) was dissolved in 3 ml DCM and cooled to 0°C. Then, 3 ml TFA was added dropwise, and the solution was stirred at ambient temperature for 6 h. The solvent was removed under reduced pressure yielding a colourless to yellow oil (31 mg, 0.055 mmol, 100% yield).

LCMS: (559.1 g/mol): *m*/*z* = 560.2 $[M + H]^+$, 582.2 $[M + Na]^+$.

JL08, JL10, JL22 – Alkyne-ISA-SS-Py

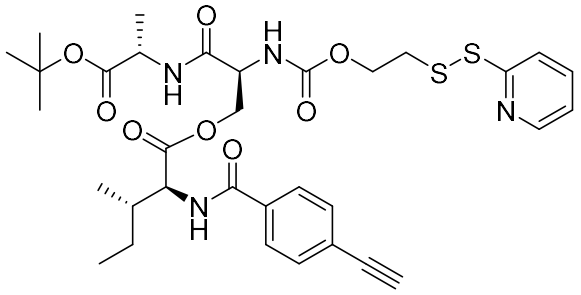

21 [686.2]

The peptide **20B** (31 mg, 0.055 mmol) was dissolved in 10 ml anhydrous DCM in an Ar-atmosphere and PyBOP (58 mg, 0.112 mmol), *L*-alanine *tert*-butyl ester hydrochloride (20 mg, 0.112 mmol) and DIPEA (0.05 ml, 0.302 mmol) were added. After 10 min additional alanine (8 mg, 0.044 mmol) was added to the reaction. The solution was stirred at room temperature overnight, diluted with ethyl acetate and washed with brine (3x 20 ml) and water (2x 20 ml). The organic phase was dried over $MgSO_4$, filtered and the solvent was removed under reduced pressure. The residue (60 mg) was further purified by silica gel column chromatography (3:2 ethyl acetate/ cyclohexane) resulting in a colorless oil (32 mg, 0.046 mmol, 84% yield).

R_f (3:1 EA/Cy, on silica): 0.8

LCMS: (686.2 g/mol): *m*/*z* = 687.3 $[M + H]^+$, 709.3 $[M + Na]^+$, 1395.7 $[2M + Na]^+$.

JL09 – Deprotection of JL08

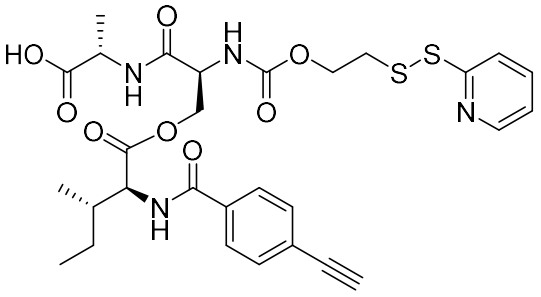

22 [630.2]

The protected peptide **21** (24 mg, 0.035 mmol) was dissolved in 2 ml DCM and 2 ml TFA. The solution was stirred at ambient temperature for 4 h. The solvent was removed under reduced pressure and the residue was dissolved in ACN/H_2O and lyophilized yielding a colorless solid (19 mg, 0.030 mmol, 86% yield).

NMR: ^{1}H NMR (700 MHz, DMSO-d6) δ 12.62 (s, 1H), 8.63 (d, *J* = 7.9 Hz, 0H), 8.52 (d, *J* = 8.4 Hz, 1H), 8.46 (dt, *J* = 4.7, 2.2 Hz, 1H), 8.36 (d, *J* = 7.4 Hz, 0H), 8.32 (d, *J* = 7.3 Hz, 1H), 7.87 (dd, *J* = 8.3, 3.9 Hz, 2H), 7.83 (tdd, *J* = 7.1, 4.8, 1.9 Hz, 1H), 7.79 (d, *J* = 8.0 Hz, 1H), 7.63 (d, *J* = 8.8 Hz, 0H), 7.57 (dd, *J* = 8.3, 1.6 Hz, 2H), 7.25 (dt, *J* = 7.7, 3.9 Hz, 1H), 4.60 (dd, *J* = 8.4, 5.7 Hz, 1H), 4.45 – 4.34 (m, 1H), 4.38 (s, 1H), 4.31 (dd, *J* = 11.0, 4.4 Hz, 0H), 4.22 (dd, *J* = 7.7, 4.8 Hz, 2H), 4.18 (t, *J* = 6.3 Hz, 2H), 4.12 (dd, *J* = 11.1, 8.0 Hz, 0H), 3.08 (t, *J* = 6.3 Hz, 2H), 2.03 – 1.90 (m, 1H), 1.51 – 1.44 (m, 1H), 1.39 (dq, *J* = 13.9, 7.0 Hz, 1H), 1.27 (dd, *J* = 7.3, 4.7 Hz, 3H), 1.25 – 1.23 (m, 1H), 1.16 (dq, *J* = 14.3, 7.4 Hz, 1H), 0.89 (dd, *J* = 13.8, 6.9 Hz, 3H), 0.85 (q, *J* = 7.7 Hz, 3H).

LCMS: (630.2 g/mol): *m*/*z* = 631.2 $[M + H]^+$, 653.2 $[M + Na]^+$, 1283.5 $[2M + Na]^+$.

JL11 – Py-SS-ISA-Alkyne-Pt-tpy

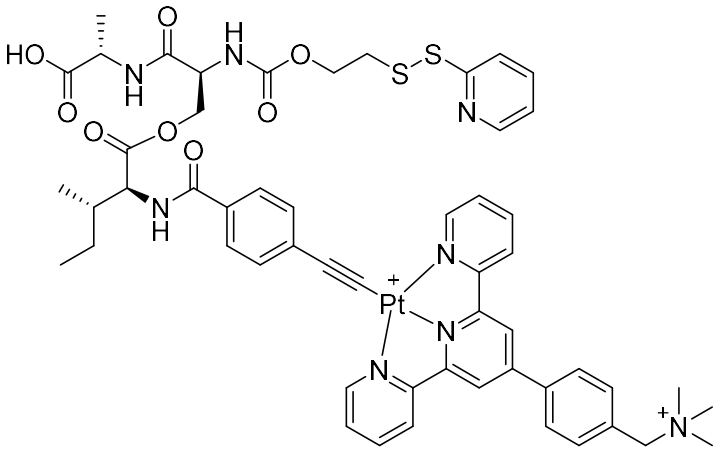

24 [1205.4]

Peptide **22** (9.8 mg, 0.0155 mmol), platinum complex **23** (15.2 mg, 0.0169 mmol), DIPEA (0.03 ml, 0.1722 mmol) and CuI (tip of a spatula) was combined in a flask and dissolved in 5 ml of anhydrous DMF in an Ar-atmosphere. Three Freeze-Pump-Thaw-Cycles were conducted, and the solution was stirred at 50°C overnight. Then, the solution was precipitated in cold ether, centrifuged (4000 rpm, 3 min) and decanted. The LCMS data showed high ratio of degradation and minor product signals.

JL37, JL39 – TAT-SS-ISA-alkyne-Pt-tpy

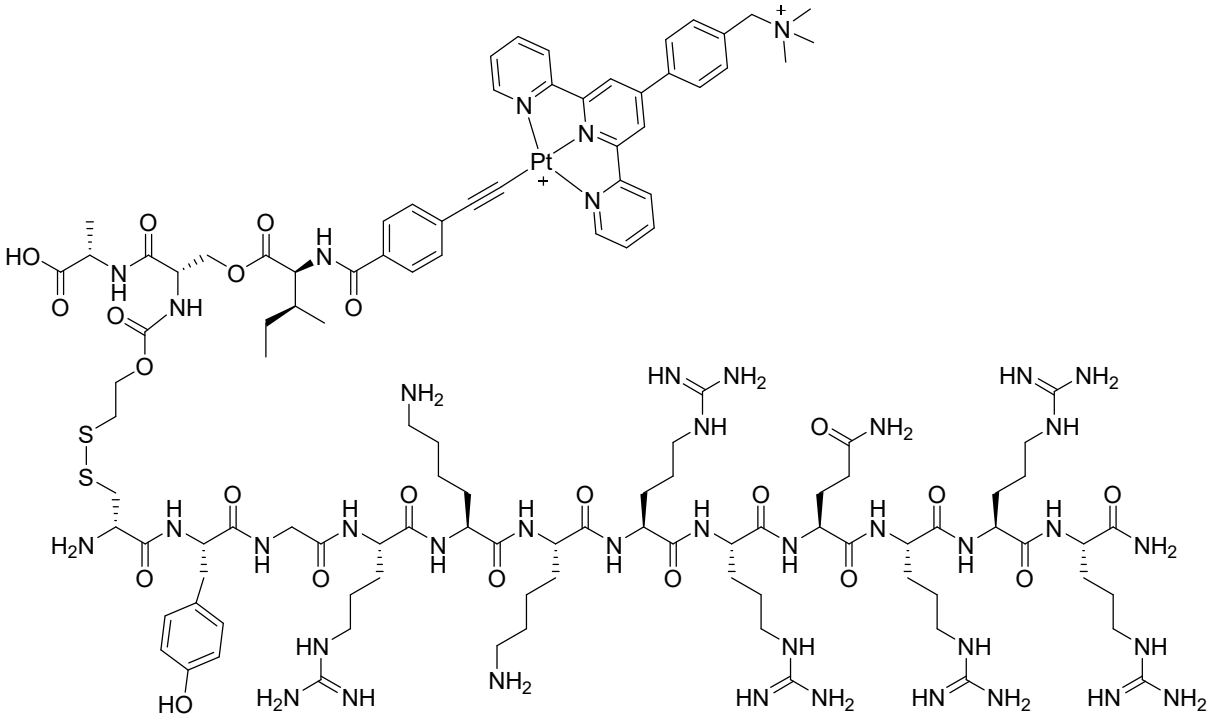

26 [2755.3]

a) JL37

Alkyne-Iso(I)SA-SS-TAT (**1**, eight attached TFA molecules estimated, 20.4 mg, 6.5 µmol), Pt-complex **23** (6.1 mg, 7.8 µmol), DIPEA (33 µl, 72.4 µmol) and CuI (tip of spatula) were dissolved in 5 ml DMF. Three Freeze-Pump-Thaw-Cycles were conducted, and the solution was stirred at 50°C overnight. Then, the solution was precipitated in cold ether, centrifuged (4000 rpm, 3 min) and decanted. The LCMS data indicated an insufficient conversion.

b) JL39

Alkyne-Iso(I)SA-SS-TAT (**1**, eight attached TFA molecules estimated, 20.1 mg, 6.5 µmol), Pt-complex **23** (7.0 mg, 6.7 µmol), DIPEA (12 µl, 344.6 µmol) and CuI (tip of spatula) were dissolved in 5 ml DMF. Three Freeze-Pump-Thaw-Cycles were conducted, and the solution was stirred at 50°C overnight. Then, the solution was

precipitated in cold ether, centrifuged (4000 rpm, 3 min) and decanted. The dark red residue was further purified by analytical HPLC.

LCMS: (2755.3 g/mol): *m*/*z* = 460.3 $[M + 4H]^{6+}$, 551.8 $[M + 3H]^{5+}$, 690.1 $[M + 2H]^{4+}$, 918.6 $[M + H]^{3+}$.

NMR: NMR experiments were not conducted, as the isolated amount of product was considered insufficient and the resulting NMR data was expected to be of reduced interest.

5.3 Solid Phase Peptide Synthesis

Peptides were synthesized using the Fmoc solid phase peptide synthesis strategy by Merrifield, synthesizing the peptide from *C*- to *N*-terminus in a microwave assisted peptide synthesizer. The resin was swollen in DMF for 1 h before use. The Fmoc-protecting group was removed by two consecutive deprotection steps (2 and 5 min) with 20% piperidine in DMF (10 ml) at 75 °C. After deprotection, the resin was washed four times with DMF (7 ml). This procedure was repeated for all coupled amino acids.

JL36, JL41, JL43 – TAT-Cys-SS-Iso(l)SA

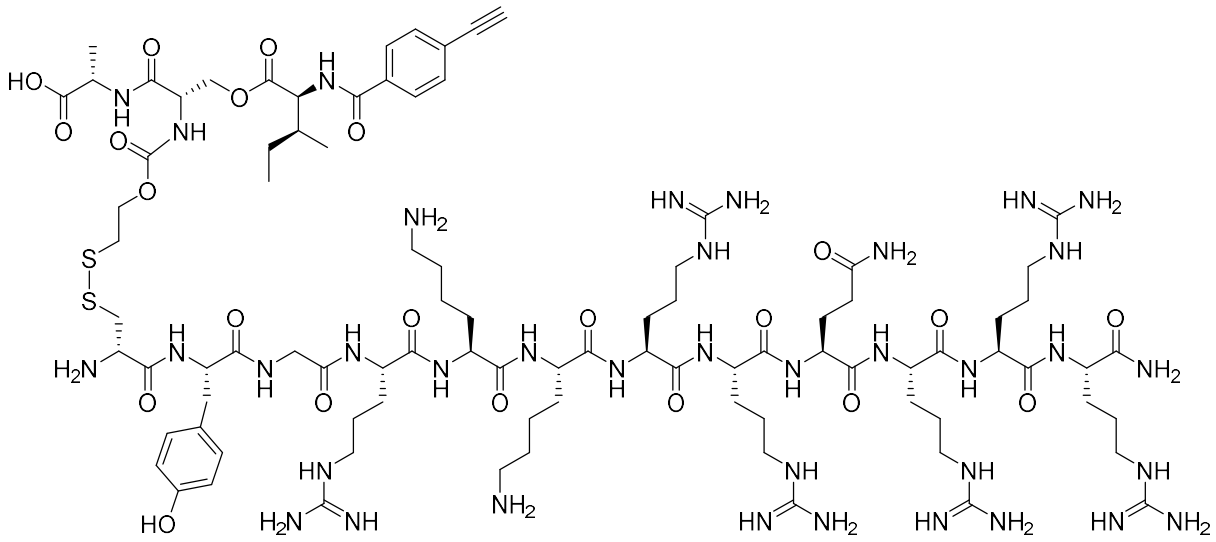

1 [2181.1]

TAT-Cys(Mmt) was synthesized using Rink amide resin at a scale of 0.1 mmol. Before every coupling, the Fmoc group was cleaved by two deprotection steps using 20% piperidine in DMF (3 mL) for 2 and 5 min at 75 °C. Fmoc-Arg(Pbf), Fmoc-Gln(Trt), Fmoc-Lys(Boc), Fmoc-Gly, Fmoc-Tyr(tBu) and Fmoc-Cys(Mmt) (5 equiv in 2.5 mL)

were coupled for 20 min using DIC as the activator (5 equiv in1 mL) and Oxyma® as the activator base (10 equiv in 0.5 mL DMF). After deprotection of the Fmoc protecting group the resin was transferred to a merrifield apparatus and treated with a cleavage cocktail consisting of 2% TFA, 5% TIPS and 93% DCM (five times for ten minutes). After washing with DMF and DCM, the disulfide containing isopeptide **21** (0.05 mmol, 37 mg) was dissolved in 5 ml DMF and added to the resin. After shaking for 3 h at ambient temperature the resin was again washed with DMF and DCM. Subsequently, the acid labile protecting groups were removed and the peptide was cleaved off the solid support in the same step using 5 ml of a cleavage solution (95% TFA, 2.5% TIPS, 2.5% H_2O) for 3 h and further purified *via* HPLC and lyophilization, yielding 66.8 mg (37%, eight attached TFA molecules estimated) of a colorless solid.

LCMS: (2181.1 g/mol): *m*/*z* = 437.4 $[M + 5H]^{5+}$, 546.3 $[M + 4H]^{4+}$, 728.2 $[M + 3H]^{3+}$, 1091.7 $[M + 2H]^{2+}$.

MALDI-Tof: (2181.1 g/mol): *m*/*z* = 1662.1 $[TAT\text{-}Cys\text{-}SH + H]^{+}$, 2182.3 $[M + H]^{+}$.

NMR: NMR experiments were not conducted as the complexity of the peptide limits the gained knowledge.

JL02, JL32 – Linear Alkyne-ISA

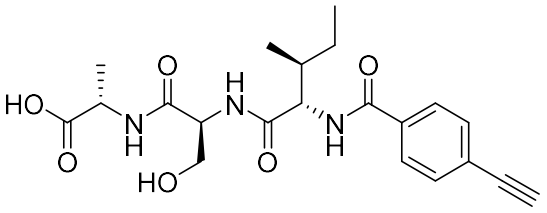

5 [417.2]

Fmoc-Ala preloaded Wang-resin (0.25 mmol) was swollen in DMF for 1 h before use. First, the Fmoc group was removed by two consecutive deprotection steps (2 and 5 min) with 20% piperidine in DMF (10 ml) at 75 °C. After deprotection, the resin was washed four times with DMF (7 ml). Fmoc-serine (5 eq. in 10 ml DMF) was coupled to the *N*-terminus by using the activator DIC (5 eq. in 5 ml DMF) and activator base Oxyma® (10 eq. in 7 ml DMF) at 75 °C for 20 min. Likewise, Fmoc-Isoleucine was coupled to the peptide.

After deprotection of the Fmoc protecting group, the *N*-terminus was modified outside the microwave reactor using the Alkyne containing benzoic acid **5** (2 eq.) in 5 ml DMF and Oxyma® (6 eq.) and DIC (3 eq.) overnight at room temperature. After washing with DMF and DCM, the resin was cleaved from the solid support by using 5 ml of a cleavage cocktail (95% TFA, 2.5% TIPS, 2.5% H_2O). The solvent was removed under reduced pressure and the crude product was further purified by HPLC to yield 39 mg (37%) of **6**.

LCMS: (417.2 g/mol): *m*/*z* = 418.2 $[M + H]^+$, 440.2 $[M + Na]^+$, 835.5 $[2M + H]^+$, 857.5 $[2M + Na]^+$.

NMR: ^{1}H NMR (700 MHz, DMSO) δ 12.55 (s, 1H), 8.44 (d, *J* = 8.5 Hz, 1H), 8.06 (d, *J* = 7.9 Hz, 1H), 7.99 (d, *J* = 7.3 Hz, 1H), 7.90 – 7.86 (m, 2H), 7.60 – 7.56 (m, 2H), 4.83 (s, 1H), 4.39 (t, *J* = 8.5 Hz, 1H), 4.38 (s, 1H), 4.34 (dt, *J* = 7.7, 5.8 Hz, 1H), 4.20 (p, *J* = 7.2 Hz, 1H), 3.59 (qd, *J* = 10.8, 5.8 Hz, 2H), 1.92 (tdd, *J* = 8.6, 6.8, 3.0 Hz, 1H), 1.50 (dtd, *J* = 14.9, 7.5, 3.4 Hz, 1H), 1.25 (d, *J* = 7.3 Hz, 3H), 1.23 – 1.14 (m, 1H), 0.91 (d, *J* = 6.8 Hz, 3H), 0.84 (t, *J* = 7.4 Hz, 3H).

JL25, JL28, JL38 – Terpyridine-KFN

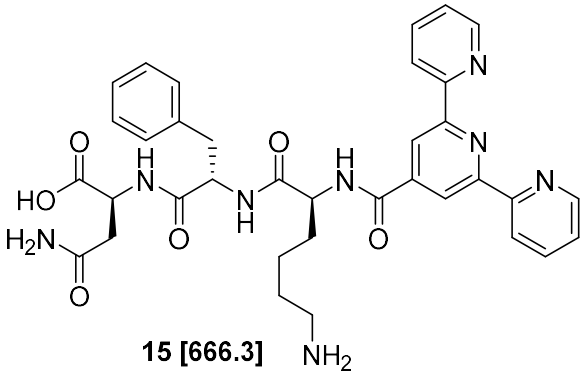

15 [666.3]

Fmoc-Asn preloaded Wang-resin (0.5 mmol) was swollen in DMF for 1 h before use. First, the Fmoc group was removed by two consecutive deprotection steps (2 and 5 min) with 20% piperidine in DMF (10 ml) at 75 °C. After deprotection, the resin was washed four times with DMF (7 ml). Fmoc-Phenylalanine (5 eq. in 10 ml DMF) was coupled to the *N*-terminus by using the activator DIC (5 eq. in 5 ml DMF) and activator base Oxyma® (10 eq. in 7 ml DMF) at 75 °C for 20 min. Likewise, Fmoc-Lysine-(Boc) was coupled to the peptide.

After deprotection of the Fmoc protecting group, the *N*-terminus was modified outside the microwave reactor using [2,2':6',2''-terpyridine]-4'-carboxylic acid (2 eq.) in 5 ml DMF and Oxyma® (6 eq.) and DIC (3 eq.) overnight at room temperature. After washing with DMF and DCM, the resin was dried, and cleaved off the solid support by using 5 ml of a cleavage cocktail (95% TFA, 2.5% TIPS, 2.5% H_2O). The product was precipitated in cold ether, centrifuged and the solid residue was further purified by HPLC and subsequent lyophilization to yield 162 mg (49%) of 15.

LCMS: (666.3 g/mol): *m*/*z* = 334.3 $[M + 2H]^{2+}$, 667.4 $[M + H]^{+}$, 1333.8 $[2M + H]^{+}$.

NMR: ^{1}H NMR (700 MHz, DMSO) δ 12.88 – 12.36 (m, 1H), 9.08 (d, *J* = 8.1 Hz, 1H), 8.84 (s, 2H), 8.79 (dd, *J* = 5.0, 1.6 Hz, 2H), 8.68 (d, *J* = 7.9 Hz, 2H), 8.34 (d, *J* = 7.8 Hz, 1H), 8.09 (d, *J* = 8.3 Hz, 1H), 8.07 (td, *J* = 7.7, 1.8 Hz, 2H), 7.61 (s, 3H), 7.59 – 7.55 (m, 2H), 7.42 (s, 1H), 7.26 (d, *J* = 7.6 Hz, 2H), 7.17 (t, *J* = 7.6 Hz, 2H), 7.08 (t, *J* = 7.4 Hz, 1H), 6.93 (s, 1H), 4.62 (td, *J* = 8.9, 4.2 Hz, 1H), 4.55 (d, *J* = 7.3 Hz, 1H), 4.53 (d, *J* = 8.1 Hz, 1H), 3.08 (dd, *J* = 14.0, 4.2 Hz, 1H), 2.84 – 2.80 (m, 1H), 2.80 – 2.75 (m, 2H), 2.58 (d, *J* = 5.7 Hz, 1H), 1.74 (dt, *J* = 14.4, 9.2 Hz, 2H), 1.54 (hept, *J* = 6.8 Hz, 2H), 1.41 – 1.22 (m, 2H).

References

1. Whitesides, G. M. & Grzybowski, B. Self-assembly at all scales. *Science.* **295**, 2418–2421 (2002).

2. Lindoy, L. F. & Atkinson, I. M. Self-assembly: What Does it Mean? in *Self-assembly in Supramolecular Systems* 1–5 (The Royal Society of Chemistry, 2000). doi:10.1039/9781847551863-00001.

3. Halley, J. D. & Winkler, D. A. Consistent concepts of self-organization and self-assembly. *Complexity* **14**, 10–17 (2008).

4. Berg, J. M., Tymoczko, J. L., Gatto jr., G. J. & Stryer, L. *Stryer Biochemie*. (Springer US, 2018).

5. Mendes, A. C., Baran, E. T., Reis, R. L. & Azevedo, H. S. Self-assembly in nature: using the principles of nature to create complex nanobiomaterials. *Wiley Interdiscip. Rev. Nanomedicine Nanobiotechnology* **5**, 582–612 (2013).

6. Whitesides, G. M., Mathias, J. P. & Seto, C. T. Molecular Self-Assembly and Nanochemistry: A Chemical Strategy for the Synthesis of Nanostructures. *Science.* **254**, 1312–1319 (1991).

7. Creighton, T. E. Protein folding. *Biochem. J.* **270**, 1–16 (1990).

8. Harrington, D. J., Adachi, K. & Royer, W. E. The High Resolution Crystal Structure of Deoxyhemoglobin S. *J. Mol. Biol.* **272**, 398–407 (1997).

9. Katsogiannou, M., Andrieu, C. & Rocchi, P. Heat shock protein 27 phosphorylation state is associated with cancer progression. *Front. Genet.* **5**, 1–5 (2014).

10. Woodson, S. A. RNA Folding Pathways and the Self-Assembly of Ribosomes. *Acc. Chem. Res.* **44**, 1312–1319 (2011).

11. Alberts, B. *et al. Molekularbiologie der Zelle*. (WILEY-VCH, 2017).

12. Dastider, D. *et al.* Hand Sanitizers Bid Farewell to Germs on Surface Area of Hands. *Eur. J. Pharm. Med. Res.* **7**, 648–656 (2020).

13. Mackenzie, R. J. DNA vs. RNA – 5 Key Differences and Comparison. *TechnologyNetworks* https://www.technologynetworks.com/genomics/lists/what-are-the-key-differences-between-dna-and-rna-296719 (2020).

14. Chagri, S., Ng, D. Y. W. & Weil, T. Designing bioresponsive nanomaterials for intracellular self-assembly. *Nat. Rev. Chem.* **accepted**, (2022).

15. Würthner, F. Aggregation-Induced Emission (AIE): A Historical Perspective. *Angew. Chemie - Int. Ed.* **59**, 14192–14196 (2020).

16. Luo, J. *et al.* Aggregation-induced emission of 1-methyl-1,2,3,4,5-pentaphenylsilole. *Chem. Commun.* **18**, 1740–1741 (2001).

17. An, H. W. *et al.* Bio-orthogonally Deciphered Binary Nanoemitters for Tumor Diagnostics. *ACS Appl. Mater. Interfaces* **8**, 19202–19207 (2016).

18. Yuan, Y. *et al.* Specific Light-Up Bioprobe with Aggregation-Induced Emission and Activatable Photoactivity for the Targeted and Image-Guided Photodynamic Ablation of Cancer Cells. *Angew. Chemie* **127**, 1800–1806 (2015).

19. Tu, Y. *et al.* Mimicking the Cell: Bio-inspired functions of supramolecular assemblies. *Chem. Rev.* **116**, 2023–2078 (2016).

20. Bradshaw, D. M. & Arceci, R. J. Clinical relevance of transmembrane drug efflux as a mechanism of multidrug resistance. *https://doi.org/10.1200/JCO.1998.16.11.3674* **16**, 3674–3690 (2016).

21. Cheng, D. B. *et al.* Autocatalytic Morphology Transformation Platform for Targeted Drug Accumulation. *J. Am. Chem. Soc.* **141**, 4406–4411 (2019).

22. Zimenkov, Y. *et al.* Rational design of a reversible pH-responsive switch for peptide self-assembly. *J. Am. Chem. Soc.* **128**, 6770–6771 (2006).

23. Liang, G., Ren, H. & Rao, J. A biocompatible condensation reaction for controlled assembly of nanostructures in living cells. *Nat. Chem. 2009 21* **2**, 54–60 (2009).

24. Pieszka, M. *et al.* Controlled Supramolecular Assembly Inside Living Cells by Sequential Multistaged Chemical Reactions. *J. Am. Chem. Soc.* **142**, 15780–15789 (2020).

25. Guo, W. W. *et al.* Intracellular Restructured Reduced Glutathione-Responsive Peptide Nanofibers for Synergetic Tumor Chemotherapy. *Biomacromolecules* **21**, 444–453 (2020).

26. Zhou, Z. *et al.* Platinum (II) Nanofibers as Assembly Driven Metabolic Inhibitors Against Metastatic Cancer Cells. *submitted* (2022).

27. Gao, Y., Shi, J., Yuan, D. & Xu, B. Imaging enzyme-triggered self-assembly of small molecules inside live cells. *Nat. Commun. 2012 31* **3**, 1–8 (2012).

28. Lee, H. K. *et al.* Light-induced self-assembly of nanofibers inside liposomes. *Soft Matter* **4**, 962–964 (2008).

29. Li, D. & Liu, C. Hierarchical chemical determination of amyloid polymorphs in neurodegenerative disease. *Nat. Chem. Biol. 2021 173* **17**, 237–245 (2021).

30. Li, M. *et al.* Proline Isomerization-Regulated Tumor Microenvironment-Adaptable Self-Assembly of Peptides for Enhanced Therapeutic Efficacy. *Nano Lett.* **19**, 7965–7976 (2019).

31. Balendiran, G. K., Dabur, R. & Fraser, D. The role of glutathione in cancer. *Cell Biochem. Funct.* **22**, 343–352 (2004).

32. Schumacker, P. T. Reactive oxygen species in cancer cells: Live by the sword, die by the sword. *Cancer Cell* **10**, 175–176 (2006).

33. Hanahan, D. & Weinberg, R. A. The Hallmarks of Cancer. *Cell* **100**, 57–70 (2000).

34. Hansen, M. J., Velema, W. A., Lerch, M. M., Szymanski, W. & Feringa, B. L. Wavelength-selective cleavage of photoprotecting groups: strategies and applications in dynamic systems. *This J. is Cite this Chem. Soc. Rev* **44**, 3358 (2015).

35. Deiters, A. Principles and applications of the photochemical control of cellular processes. *ChemBioChem* **11**, 47–53 (2010).

36. Young, D. D., Lusic, H., Lively, M. O., Yoder, J. A. & Deiters, A. Gene Silencing in Mammalian Cells with Light-Activated Antisense Agents. *ChemBioChem* **9**, 2937–2940 (2008).

37. Fournier, L. *et al.* A Blue-Absorbing Photolabile Protecting Group for in Vivo Chromatically Orthogonal Photoactivation. (2013) doi:10.1021/cb400178m.

38. Elamri, I. *et al.* Wavelength-Selective Uncaging of Two Different Photoresponsive Groups on One Effector Molecule for Light-Controlled Activation and Deactivation. *J. Am. Chem. Soc.* **143**, 10596–10603 (2021).

39. Casey, J. R., Grinstein, S. & Orlowski, J. Sensors and regulators of intracellular pH. (2009) doi:10.1038/nrm2820.

40. Waqas, M. *et al.* PH-Dependent In-Cell Self-Assembly of Peptide Inhibitors Increases the Anti-Prion Activity while Decreasing the Cytotoxicity. *Biomacromolecules* **18**, 943–950 (2017).

41. Shaw, P. E. Peptidyl-prolyl isomerases: a new twist to transcription. *EMBO Rep.* **3**, 521–526 (2002).

42. Sies, H. Glutathione and its role in cellular functions. *Free Radic. Biol. Med.* **27**, 916–921 (1999).

43. Depeille, P., Cuq, P., Passagne, I., Evrard, A. & Vian, L. Combined effects of GSTP1 and MRP1 in melanoma drug resistance. *Br. J. Cancer* **93**, 216–223 (2005).

44. Chagri, S., Ng, D. Y. W., Weil, T. & Al., E. Unpublished Work. (2020).

45. Veal, E. A., Day, A. M. & Morgan, B. A. Hydrogen Peroxide Sensing and Signaling. *Mol. Cell* **26**, 1–14 (2007).

46. Riedel, E. & Janiak, C. *Moderne Anorganische Chemie*. (De Gruyter, 2007).

47. Lippert, B. *Cisplatin: Chemistry and biochemistry of a leading anticancer drug*. *Cisplatin: Chemistry and Biochemistry of a Leading Anticancer Drug* (Wiley-VCH, 1999). doi:10.1002/9783906390420.

48. Takahara, P. M., Rosenzweig, A. C., Frederick, C. A. & Lippard, S. J. Crystal structure of double-stranded DNA containing the major adduct of the anticancer drug cisplatin. *Nat. 1995 3776550* **377**, 649–652 (1995).

49. Wing-Wah Yam, V., Ka-Man Au, V. & Yu-Lut Leong, S. Light-Emitting Self-Assembled Materials Based on d8 and d10 Transition Metal Complexes. *Chem. Rev.* **115**, 7589–7728 (2015).

50. Ratilla, E. M. A., Scott, B. K., Moxness, M. S. & Kostić, N. M. Terminal and New Bridging Coordination of Methylguanidine, Arginine, and Canavanine to Platinum(II). The First Cristallographic Study of Bonding between a Transition Metal and a Guanidine Ligand. *Inorg. Chem.* **29**, 918–926 (1990).

51. Bailey, J. A., Miskowski, V. M. & Gray, H. B. Spectroscopic and structural properties of binuclear platinum-terpyridine complexes. *Inorg. Chem.* **32**, 369–370 (1993).

52. Connick, W. B., Henling, L. M., Marsh, R. E. & Gray, H. B. Emission Spectroscopic Properties of the Red Form of Dichloro(2,2′-bipyridine)platinum(II). Role of Intermolecular Stacking Interactions. *Inorg. Chem.* **35**, 6261–6265 (1996).

53. Yip, H.-K., Cheng, L.-K., Cheung, K.-K. & Che, C.-M. *Luminescent Platinum (II) Complexes. Electronic Spectroscopy of Platinum(II) Complexes of 2,2':6',2''-Terpyridine (terpy) and p-Substituted Phenylterpyridines and Crystal Structure of [Pt(terpy)Cl] [CF3S03]*. *J. CHEM. SOC. DALTON TRANS* (1993).

54. Yam, V. W. W., Yu, K. L., Wong, K. M. C. & Cheung, K. K. Synthesis and structural characterization of a novel luminescent tetranuclear mixed-metal platimim(II)- Copper (I) complex. *Organometallics* **20**, 721–726 (2001).

55. Chung, C. Y. S., Li, S. P. Y., Morris, J. A., Sale, D. & Yam, V. W. W. Induced self-assembly and disassembly of water-soluble alkynylplatinum(II) terpyridyl complexes with “switchable” near-infrared (NIR) emission modulated by metal–metal interactions over physiological pH: demonstration of pH-responsive NIR luminescent probes in cell-imaging studies. *Chem. Sci.* **4**, 2453–2462 (2013).

56. Wong, K. M. C. & Yam, V. W. W. Luminescence platinum (II) terpyridyl complexes - from fundamental studies to sensory functions. *Coord. Chem. Rev.* **251**, 2477–2488 (2007).

57. Yam, V. W. W., Wong, K. M. C. & Zhu, N. Solvent-induced aggregation through metal···metal/π···π interactions: Large solvatochrmism of luminescent organoplatinum(II) terpyridyl complexes. *J. Am. Chem. Soc.* **124**, 6506–6507 (2002).

58. Septiadi, D., Aliprandi, A., Mauro, M. & De Cola, L. Bio-imaging with neutral luminescent Pt(II) complexes showing metal···metal interactions. *RSC Adv.* **4**, 25709–25718 (2014).

59. Aliprandi, A., Mauro, M. & De Cola, L. Controlling and imaging biomimetic self-assembly. *Nat. Chem.* **8**, 10–15 (2016).

60. Wing-Wah Yam, V., Kwun-Wa Chan, A. & Yau-Hin Hong, E. *Charge-transfer processes in metal complexes enable luminescence and memory functions*. *Nature Reviews Chemistry* www.nature.com/natrevchem doi:10.1038/s41570-020-0199-7.

61. Ren, Y., Ng, D. Y. W., Weil, T. & Al., E. Unpublished Work. (2022).

62. Weinrich, T., Gränz, M., Grünewald, C., Prisner, T. F. & Göbel, M. W. Synthesis of a Cytidine Phosphoramidite with Protected Nitroxide Spin Label for EPR Experiments with RNA. *European J. Org. Chem.* **2017**, 491–496 (2017).

63. Atkins, P. & De Paula, J. *Atkins' Physical Chemistry*. (Oxford University Press, 2006).

64. Frankel, A. D. & Pabo, C. O. Cellular uptake of the tat protein from human immunodeficiency virus. *Cell* **55**, 1189–1193 (1988).

Appendix

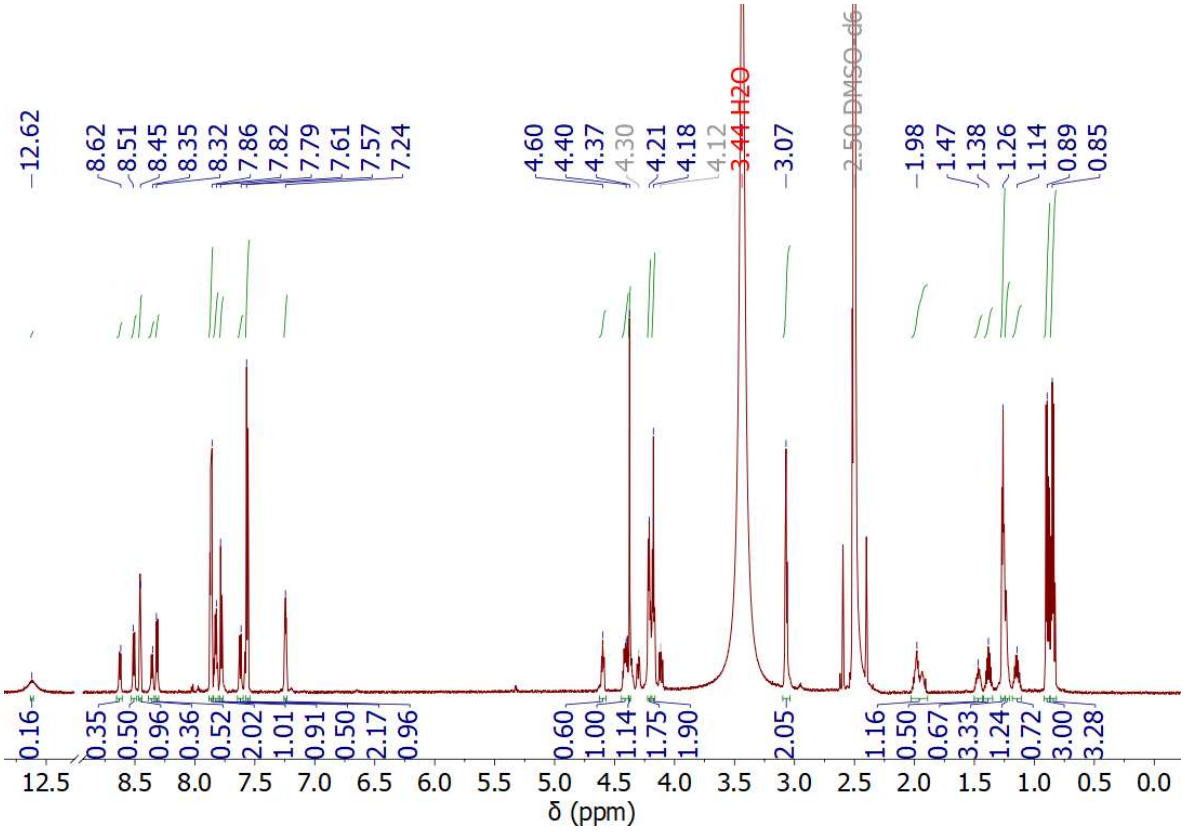

Figure 26: ^{1}H-NMR spectrum of JL09 (22) ($CDCl_3$, 300 MHz, 298 K). Processed with MestReNova.

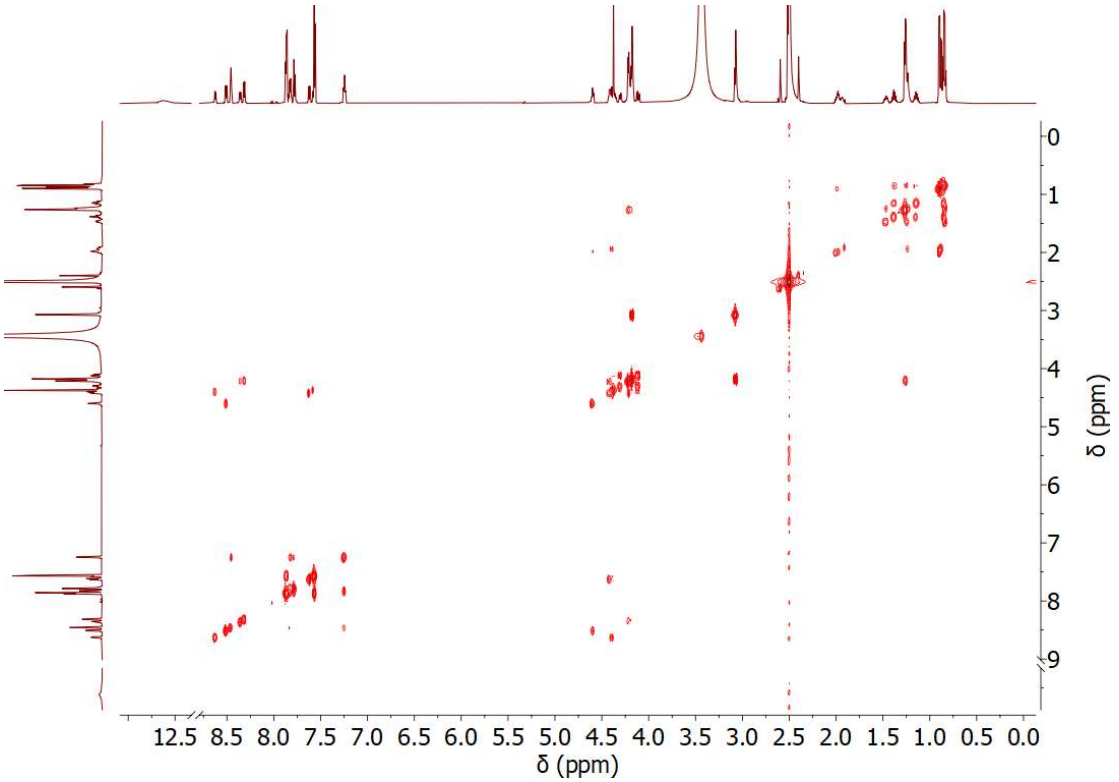

Figure 27: COSY-NMR spectrum of JL09 (22) ($CDCl_3$, 300 MHz, 298 K). Processed with MestReNova.

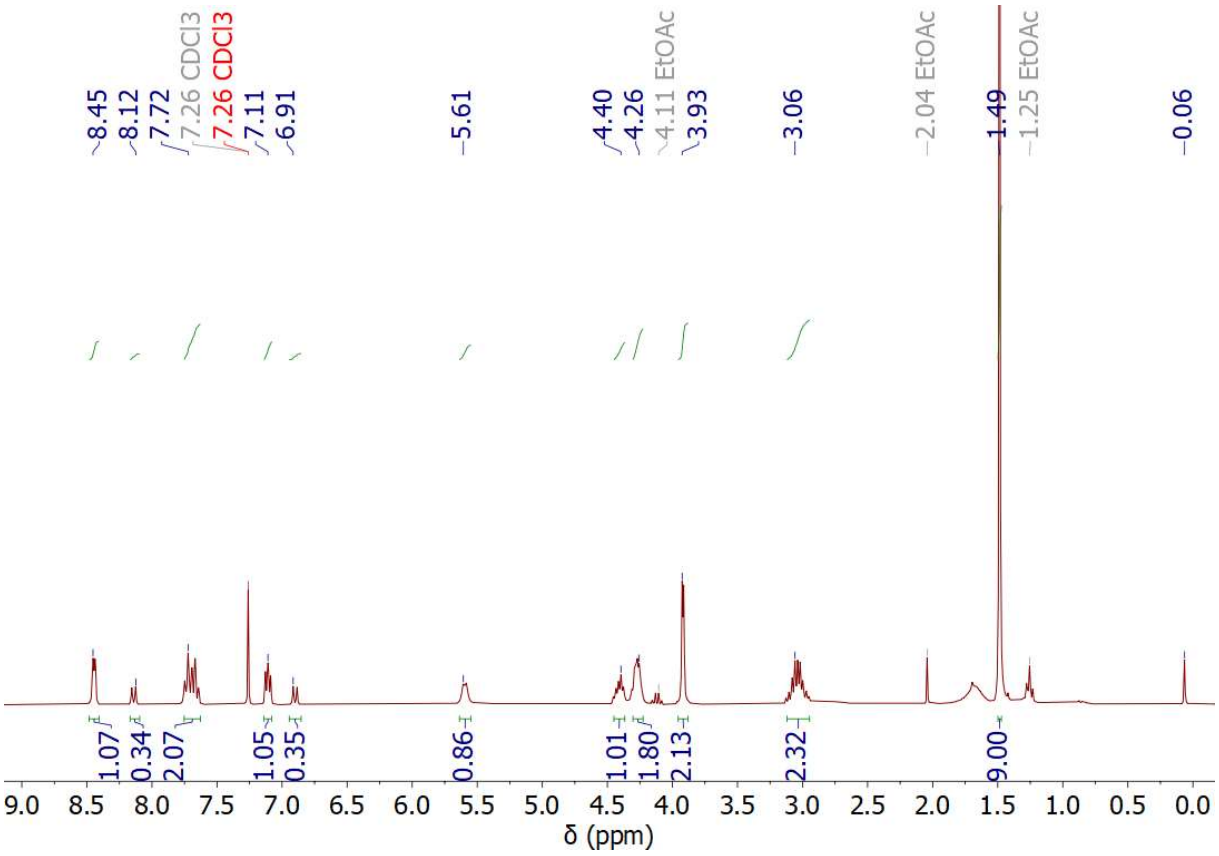

Figure 28: ^{1}H-NMR spectrum of JL12 (19) ($CDCl_3$, 300 MHz, 298 K). Processed with MestReNova.

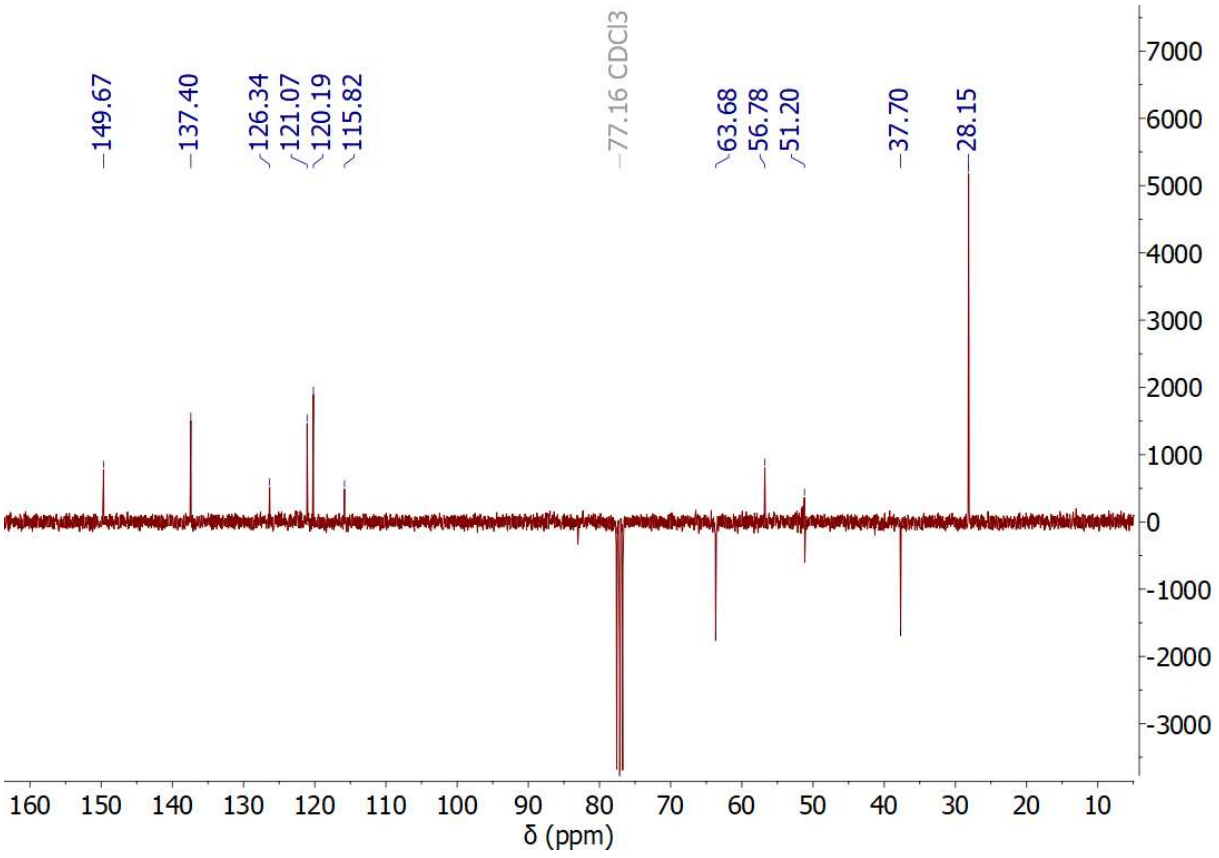

Figure 29: ^{13}C-NMR spectrum of JL12 (19) ($CDCl_3$, 300 MHz, 298 K). Processed with MestReNova.

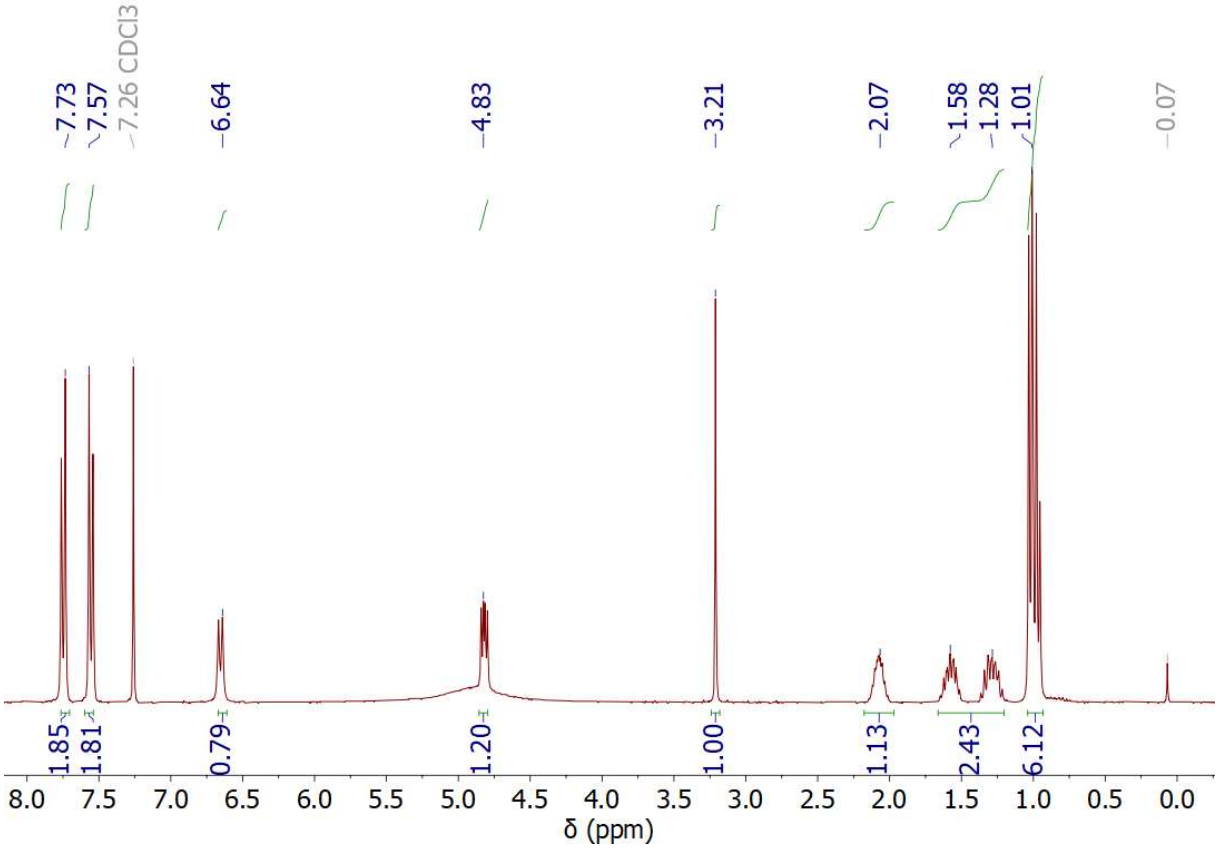

Figure 30: ^{1}H-NMR spectrum of JL13 (17) ($CDCl_3$, 300 MHz, 298 K). Processed with MestReNova.

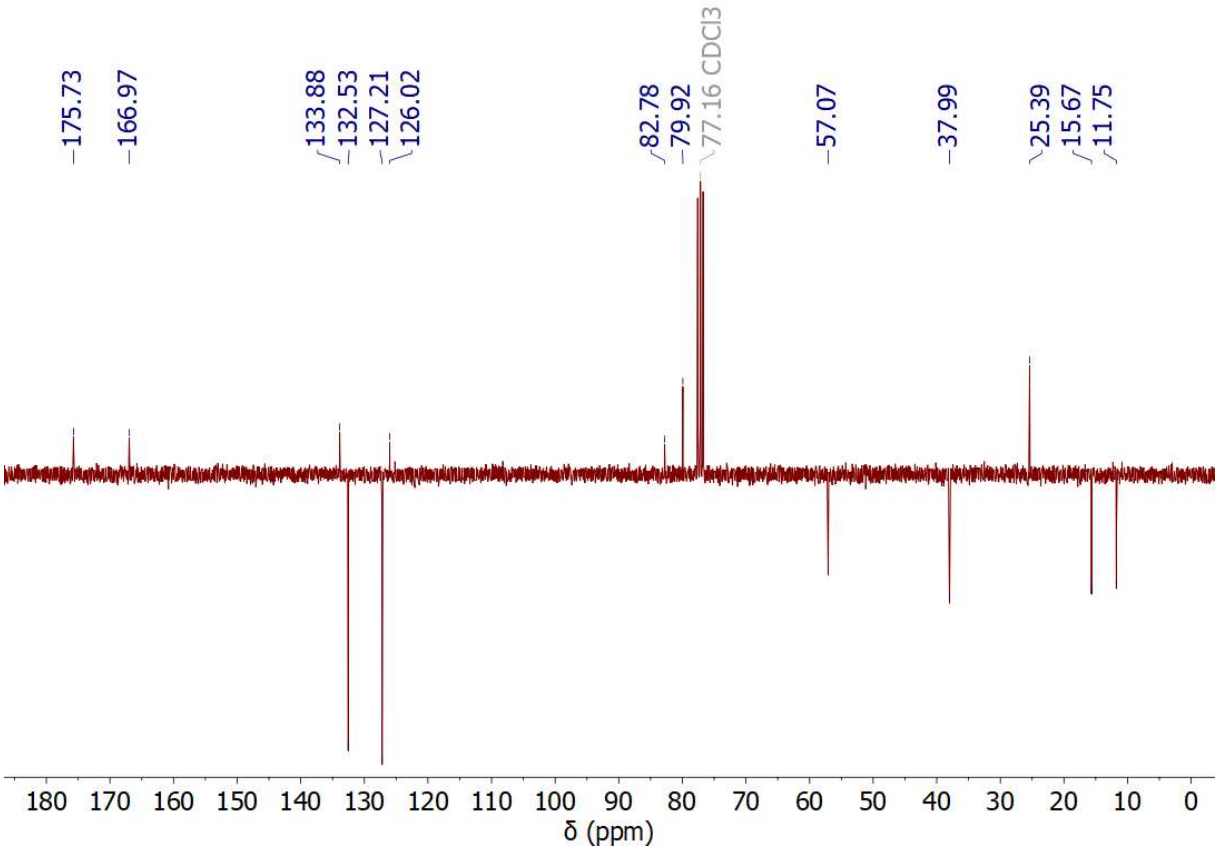

Figure 31: ^{13}C-NMR spectrum of JL13 (17) ($CDCl_3$, 300 MHz, 298 K). Processed with MestReNova.

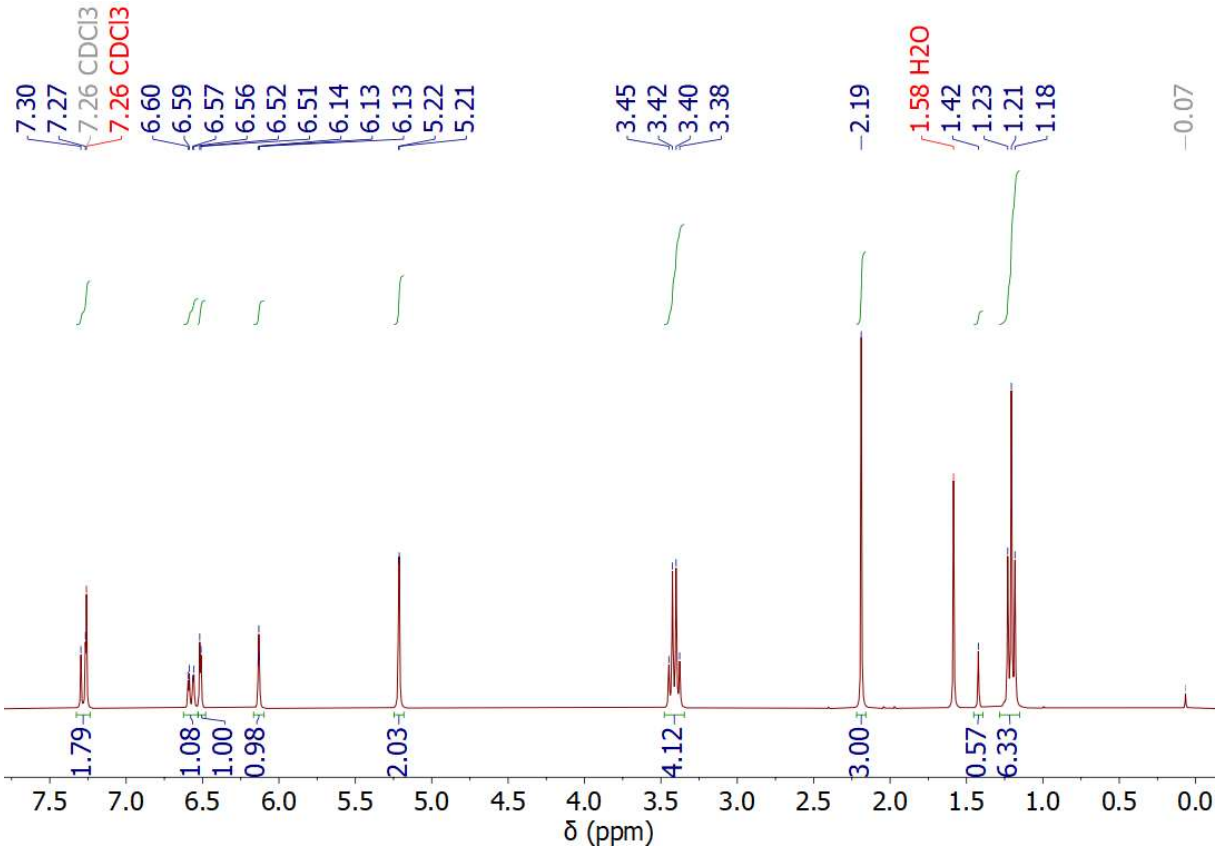

Figure 32: ^{1}H-NMR spectrum of JL15 (11) ($CDCl_3$, 300 MHz, 298 K). Processed with MestReNova.

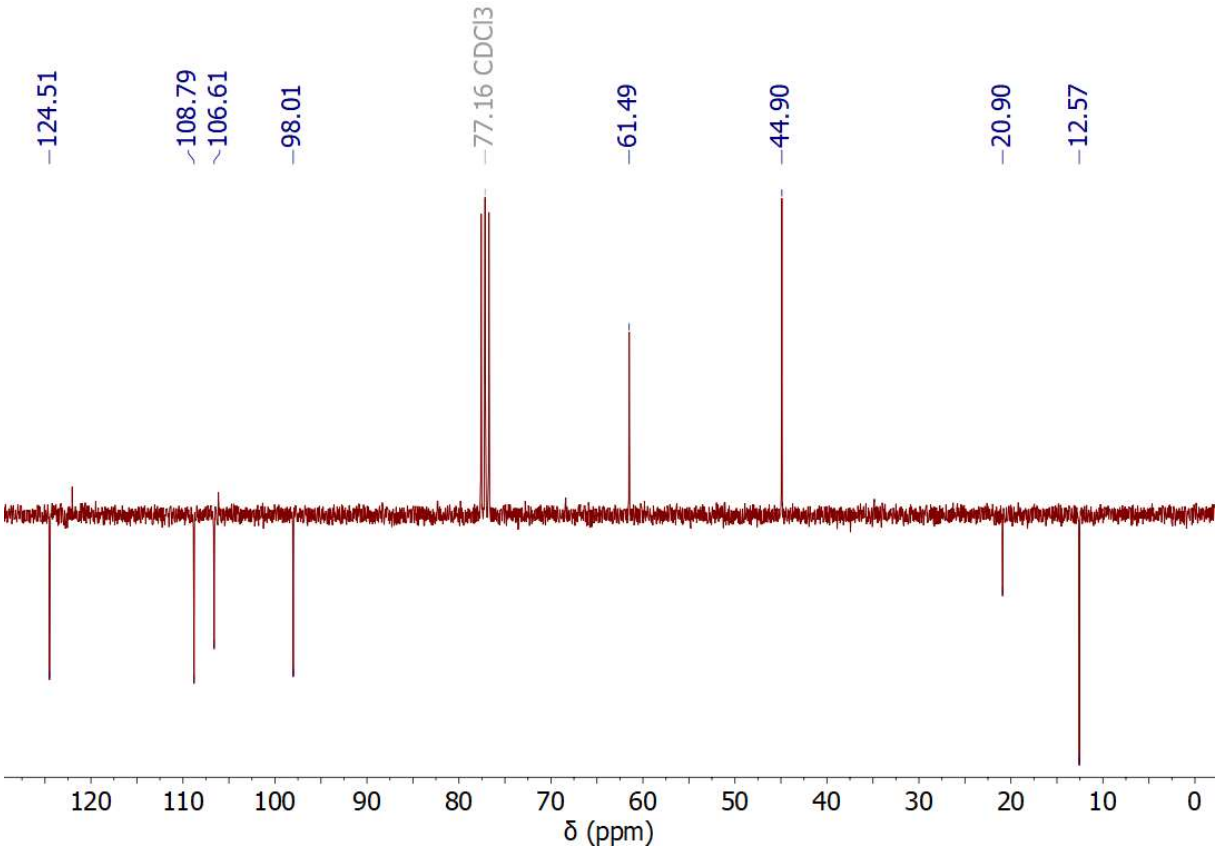

Figure 33: ^{13}C-NMR spectrum of JL15 (11) ($CDCl_3$, 300 MHz, 298 K). Processed with MestReNova.

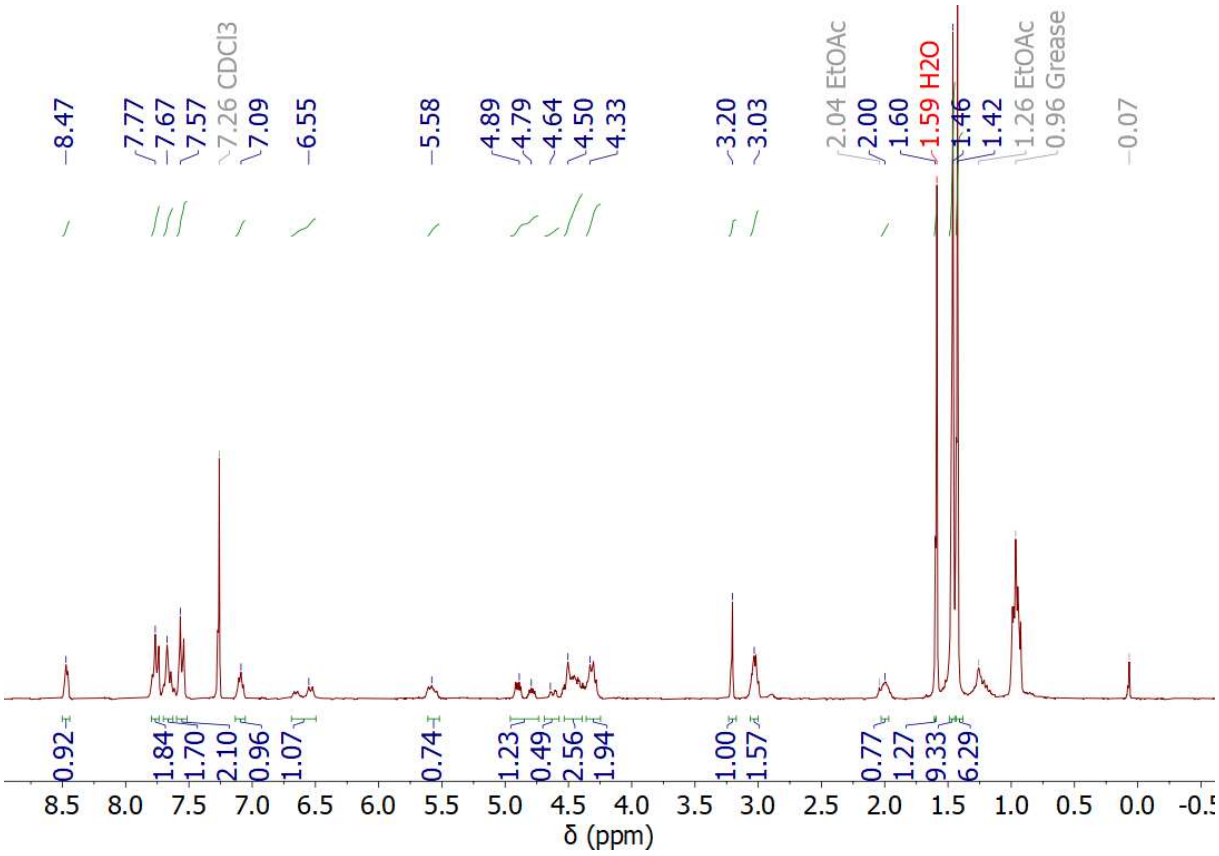

Figure 34: ^{1}H-NMR spectrum of JL16 (20) ($CDCl_3$, 300 MHz, 298 K). Processed with MestReNova.

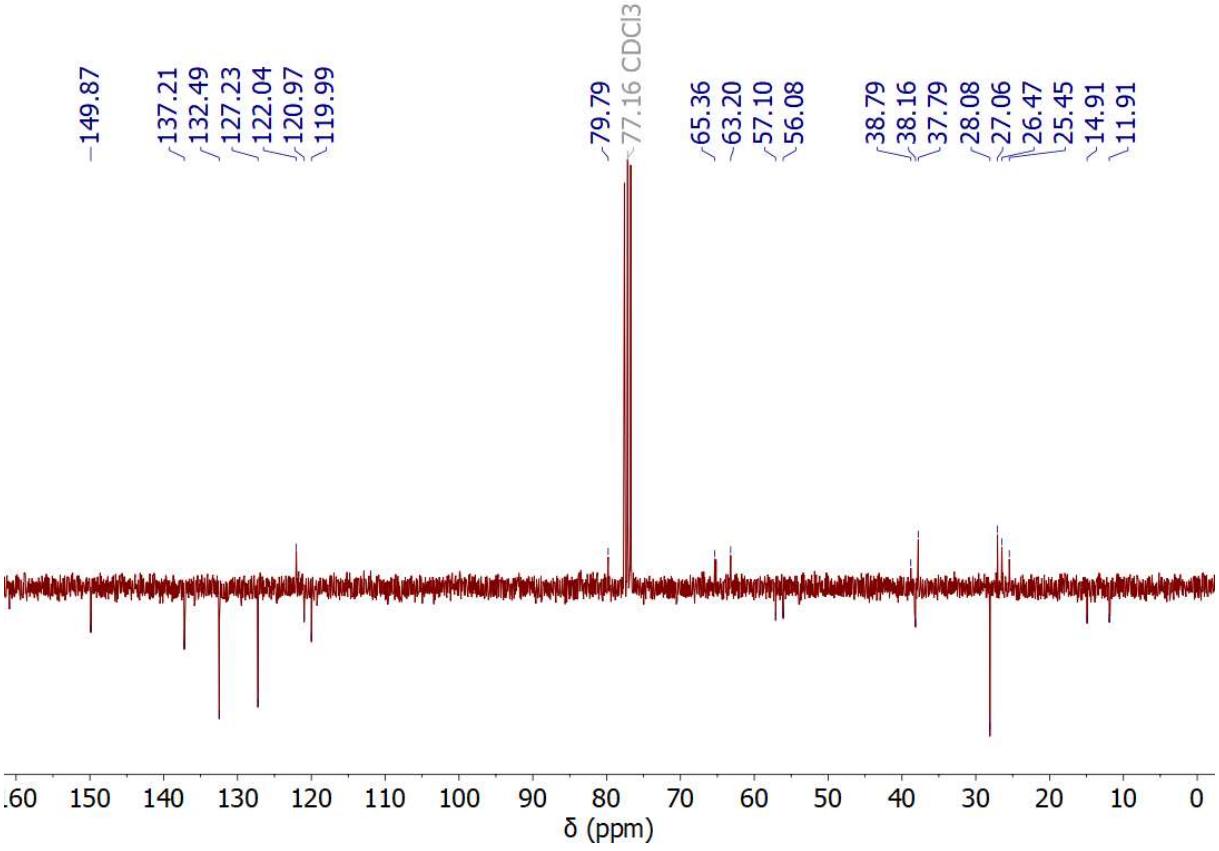

Figure 35: ^{13}C-NMR spectrum of JL16 (20) ($CDCl_3$, 300 MHz, 298 K). Processed with MestReNova.

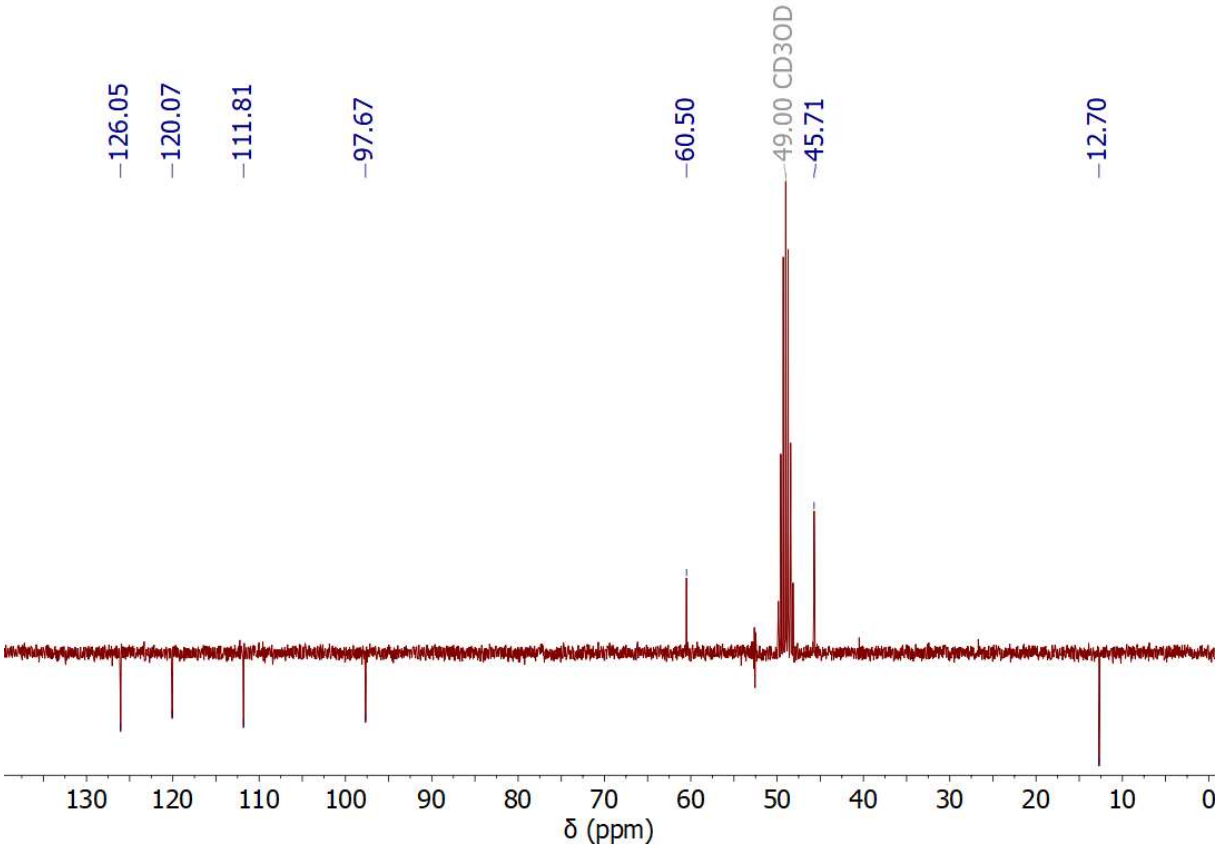

Figure 36: ^{13}C-NMR spectrum of JL20 (13) (d3-MeOD, 300 MHz, 298 K). Processed with MestReNova.

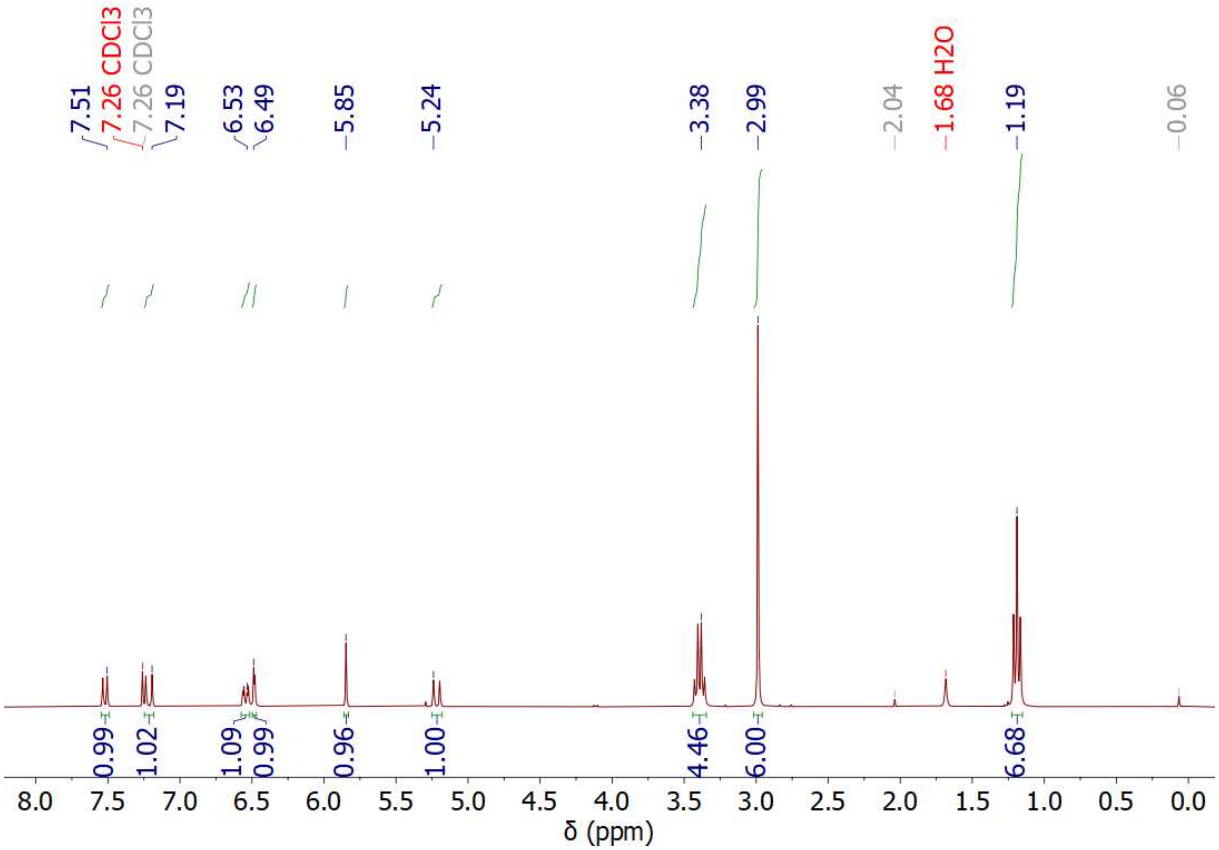

Figure 37: ^{1}H-NMR spectrum of JL24 (8) ($CDCl_3$, 300 MHz, 298 K). Processed with MestReNova.

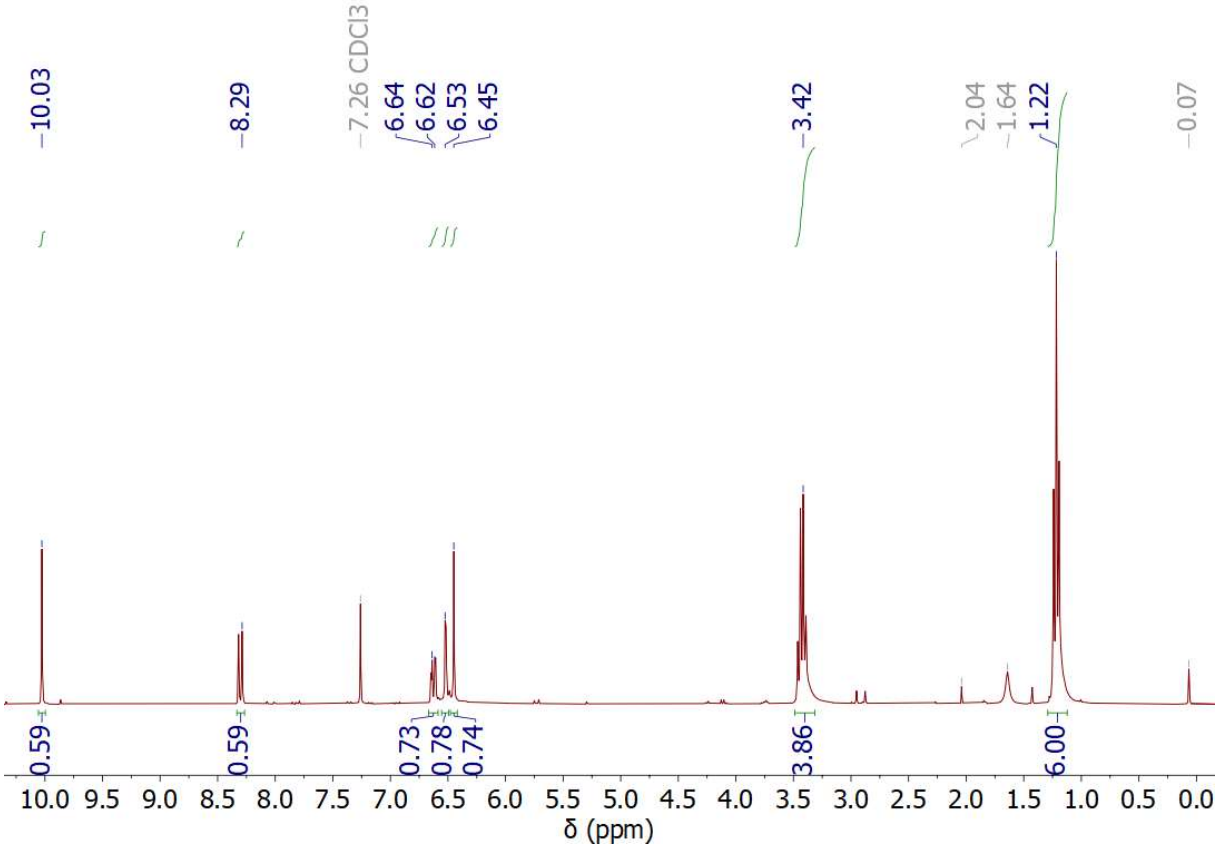

Figure 38: ^{1}H-NMR spectrum of JL29 (9) ($CDCl_3$, 300 MHz, 298 K). Processed with MestReNova.

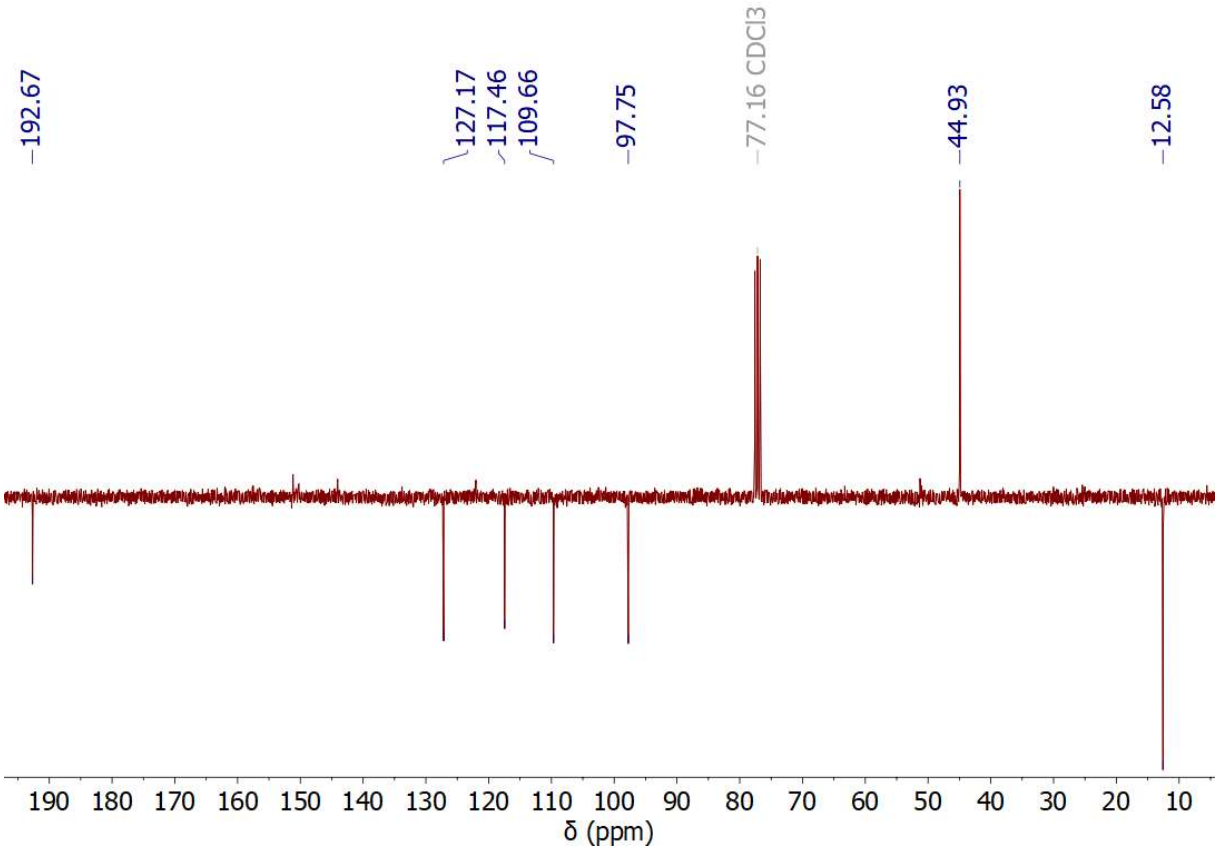

Figure 39: ^{13}C-NMR spectrum of JL29 (9) (d3-MeOD, 300 MHz, 298 K). Processed with MestReNova.

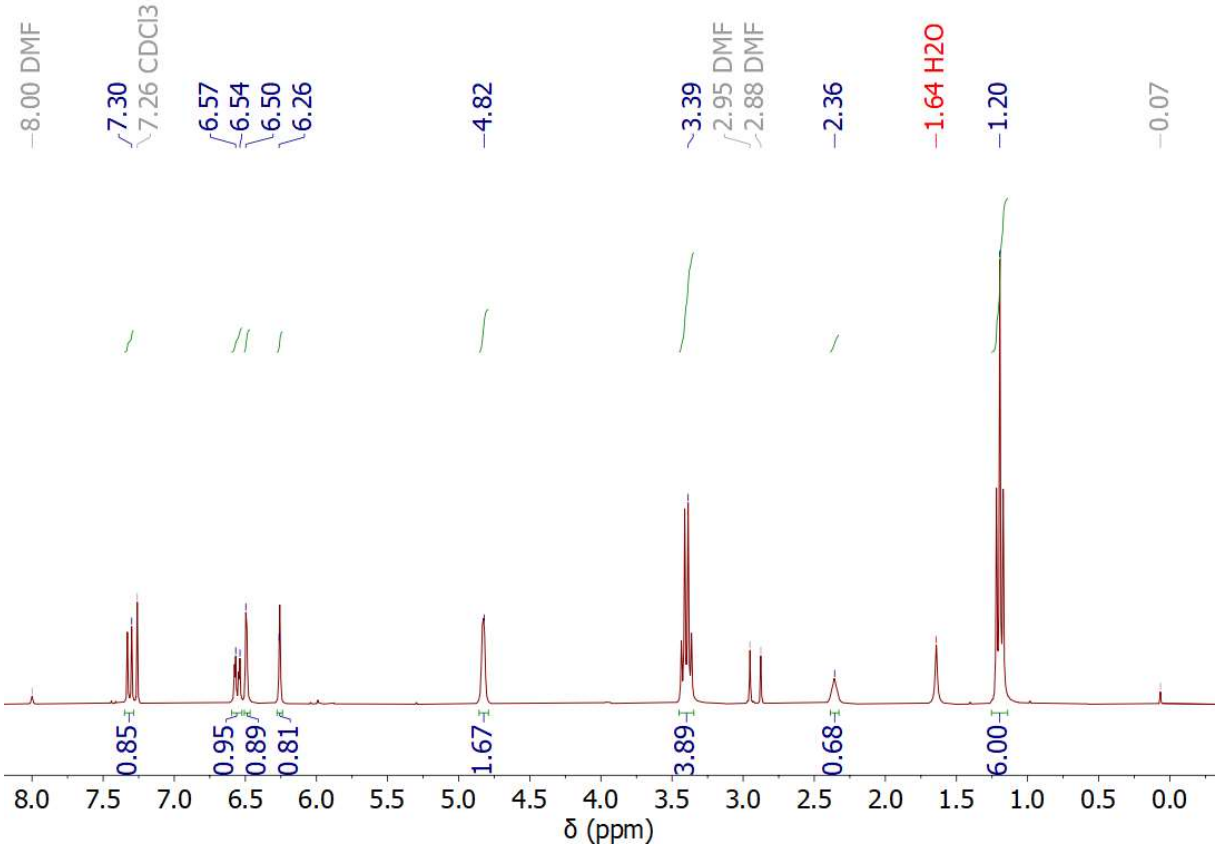

Figure 40: ^{1}H-NMR spectrum of JL40 (10) ($CDCl_3$, 300 MHz, 298 K). Processed with MestReNova.

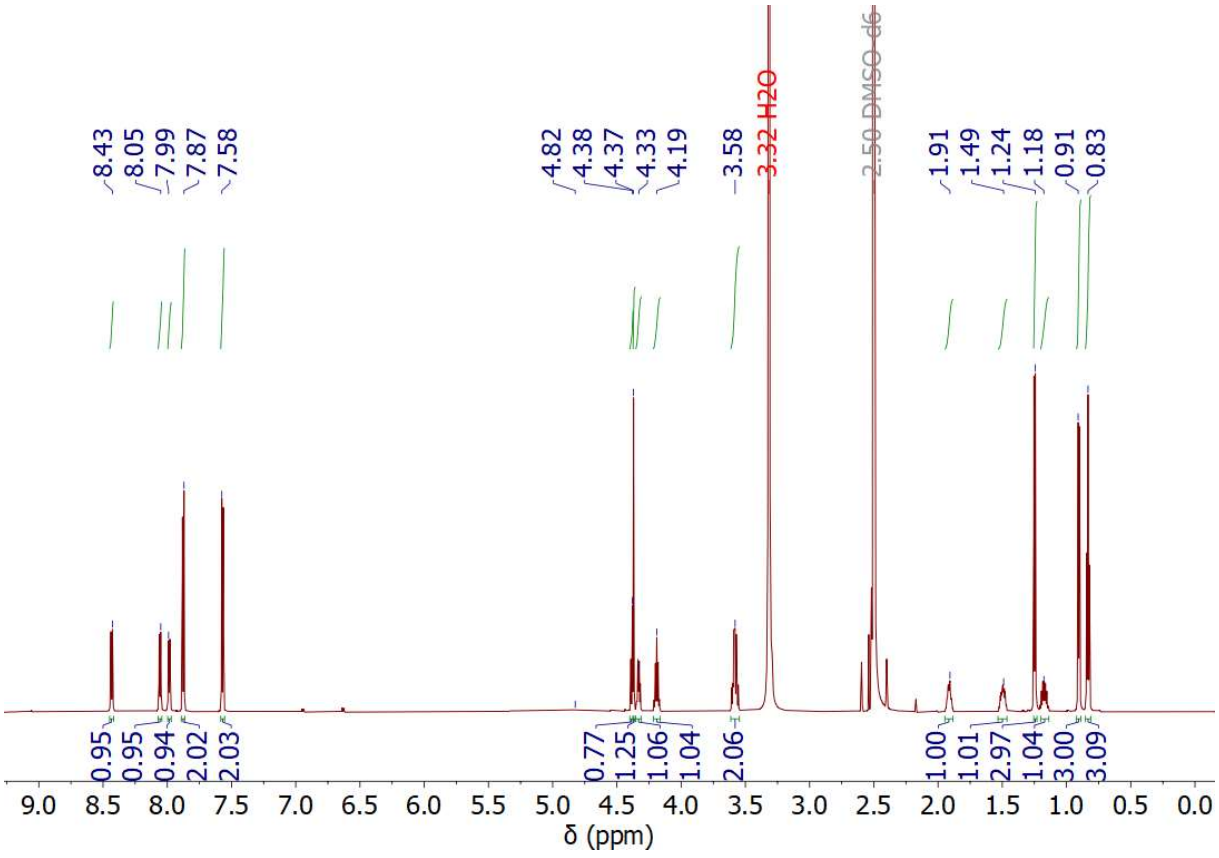

Figure 41: ^{1}H-NMR spectrum of linear Alkyne-ISA (JL32, 5) (d6-DMSO, 750 MHz, 298 K). Processed with MestReNova.

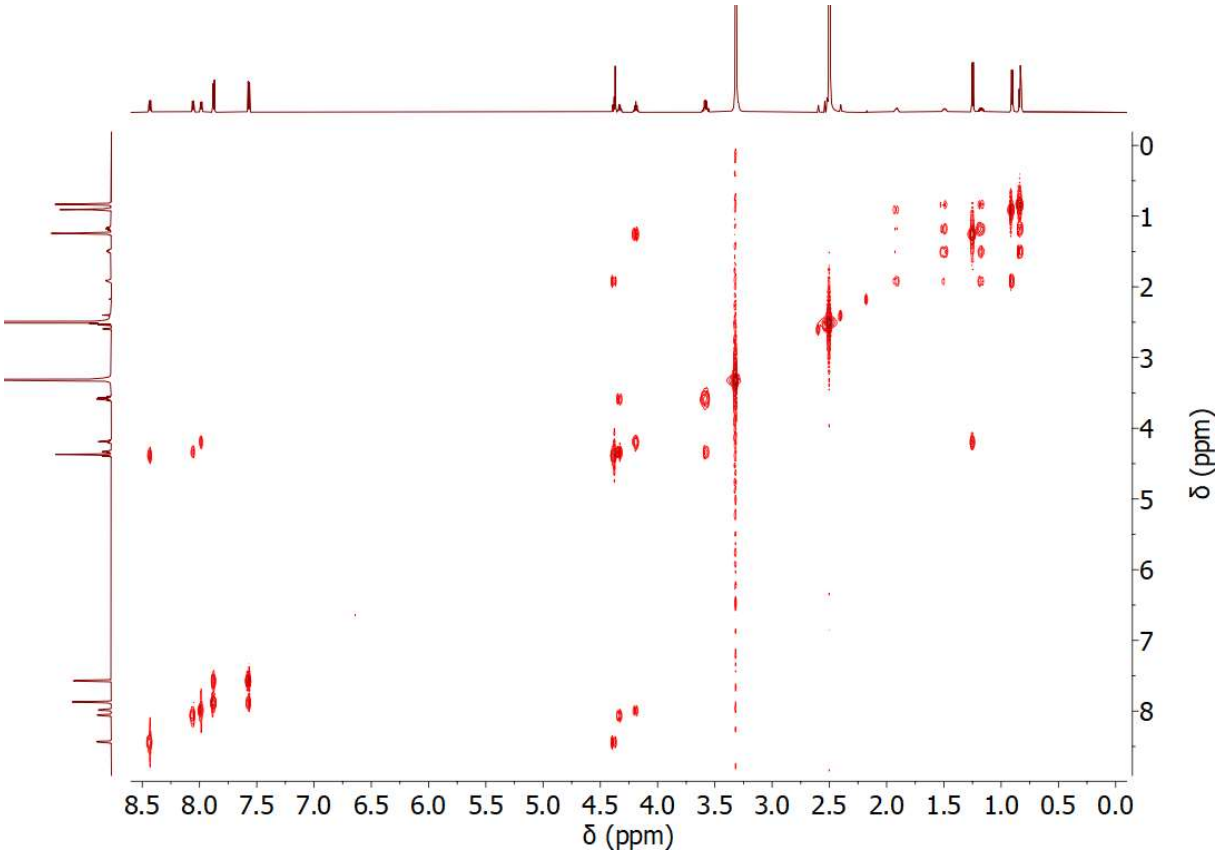

Figure 42: COSY-NMR spectrum of linear Alkyne-ISA (JL32, 5) (d6-DMSO, 750 MHz, 298 K). Processed with MestReNova.

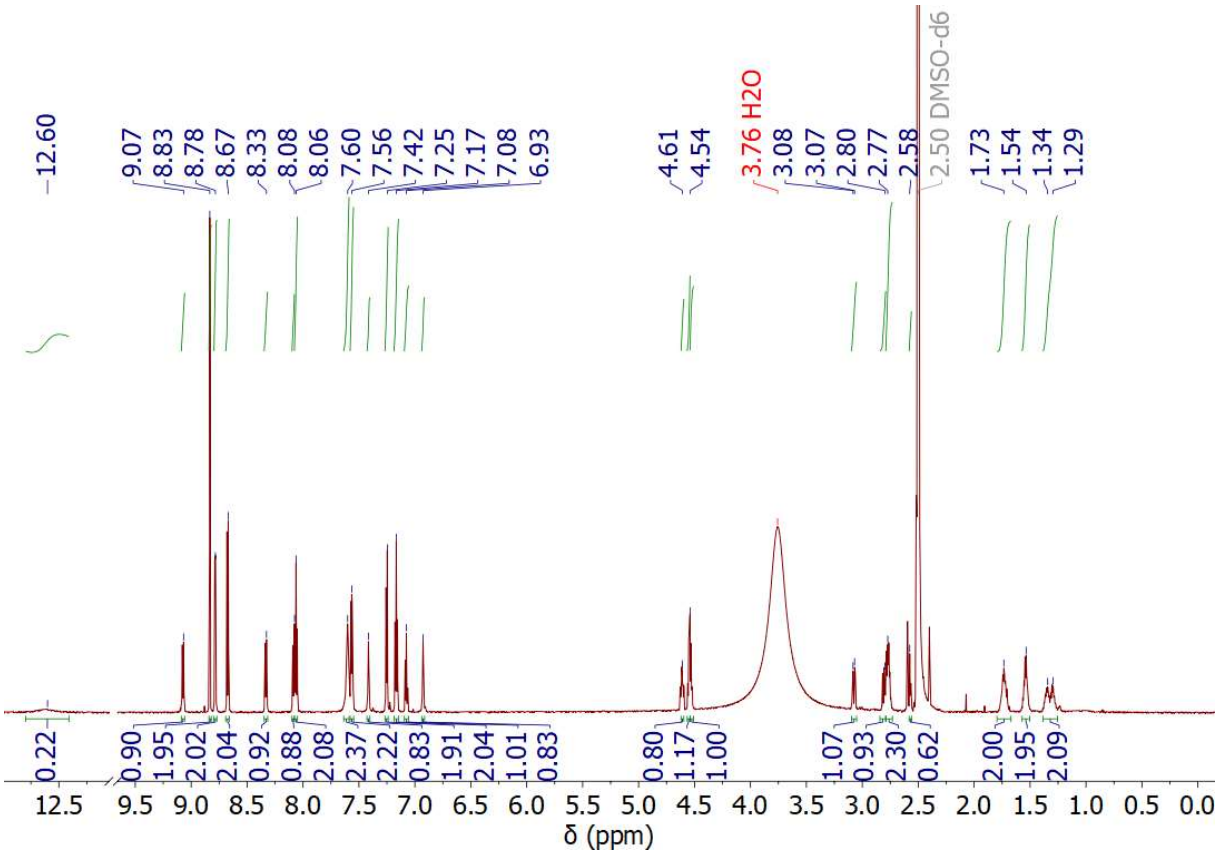

Figure 43: ^{1}H-NMR spectrum of linear tpy-KFN (JL38, 15) (d6-DMSO, 750 MHz, 298 K). Processed with MestReNova.

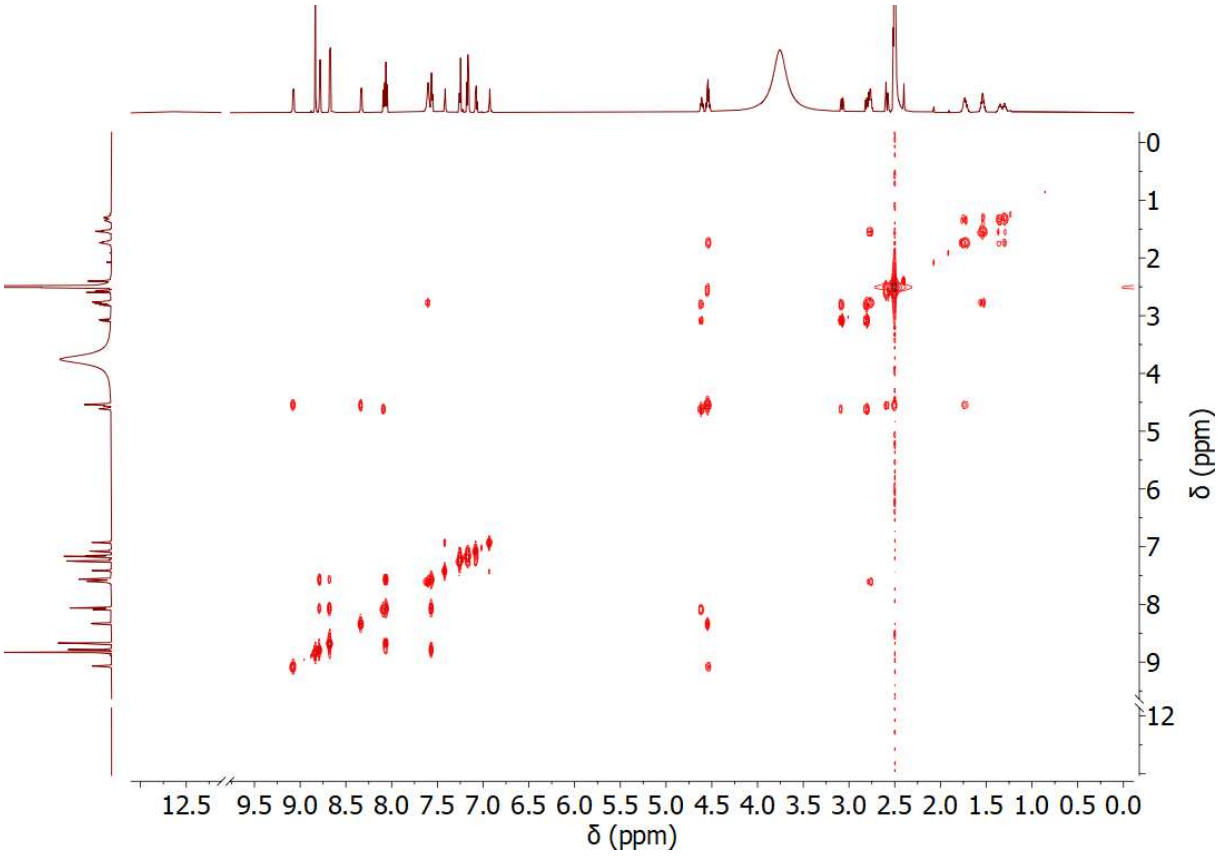

Figure 44: COSY-NMR spectrum of linear tpy-KFN (JL38, 15) (d6-DMSO, 750 MHz, 298 K). Processed with MestReNova.

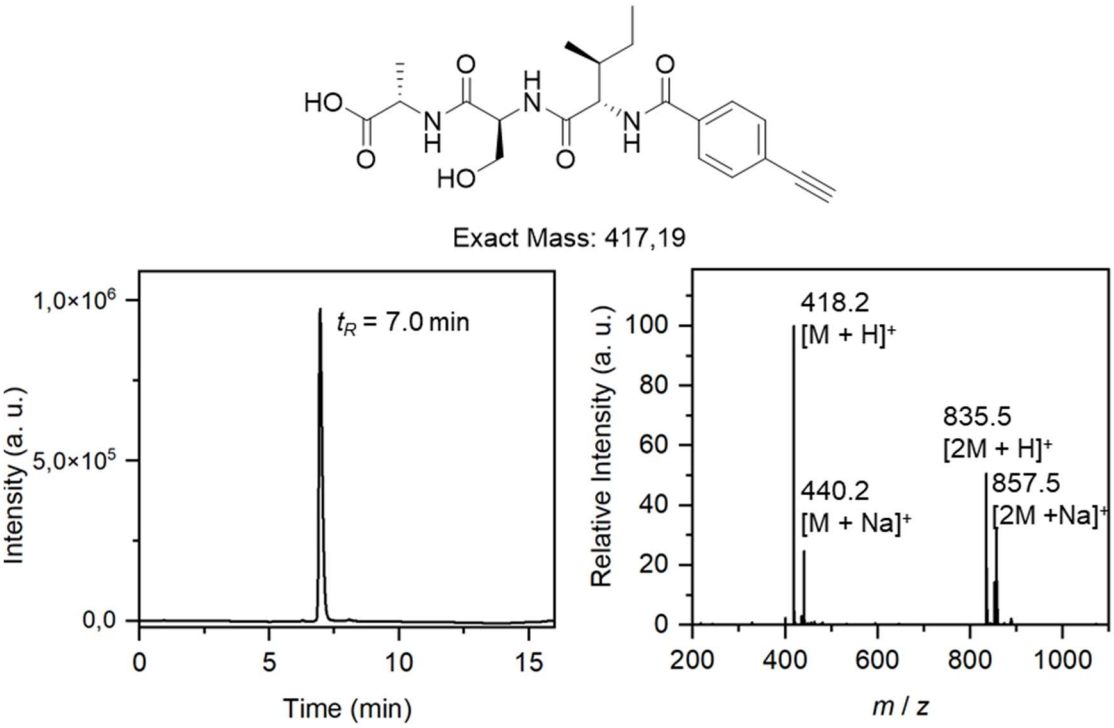

Figure 45: LC elugram (left, detection at 254 nm) and corresponding mass data (right) of JL02 (5).

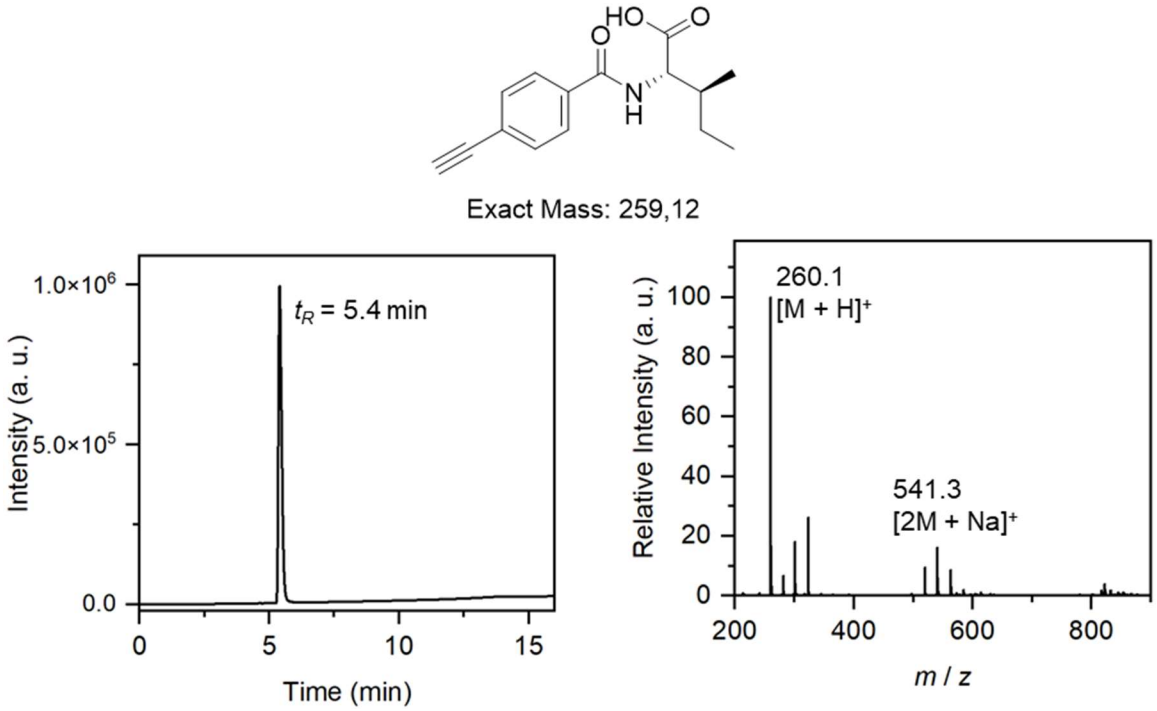

Figure 46: LC elugram (left, detection at 254 nm) and corresponding mass data (right) of JL03 (17).

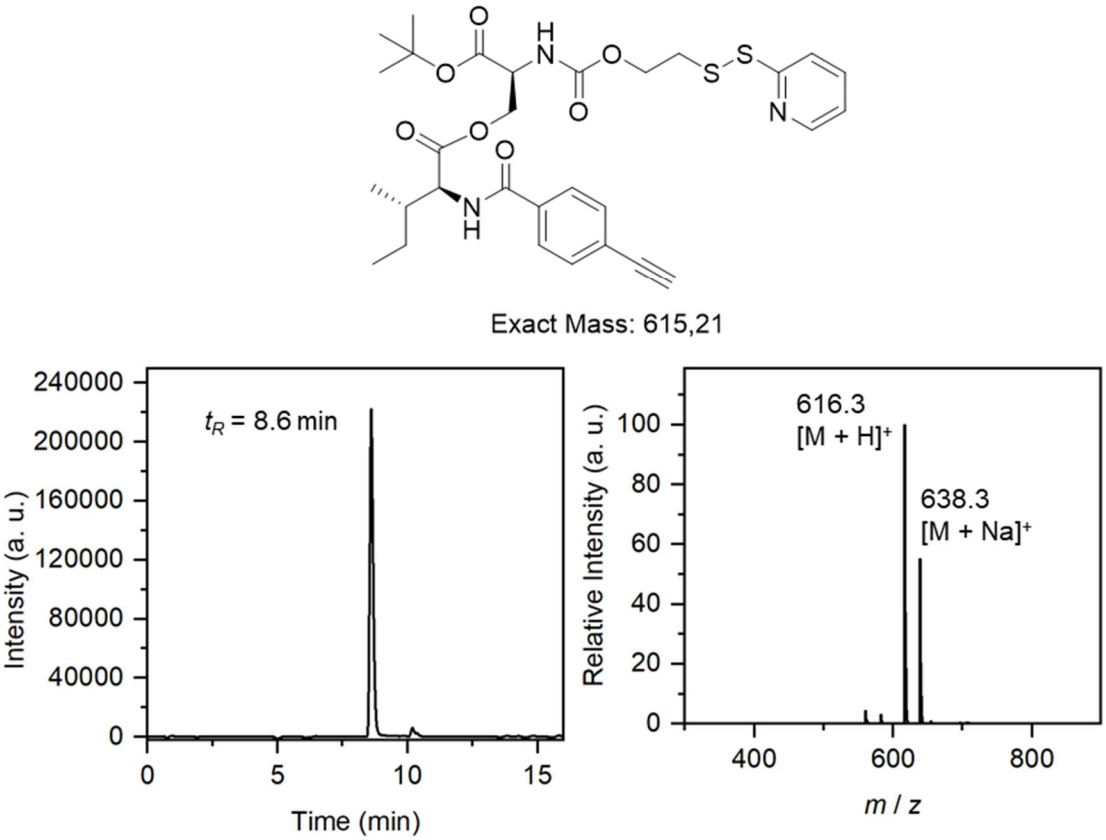

Figure 47: LC elugram (left, detection at 254 nm) and corresponding mass data (right) of JL05 (20).

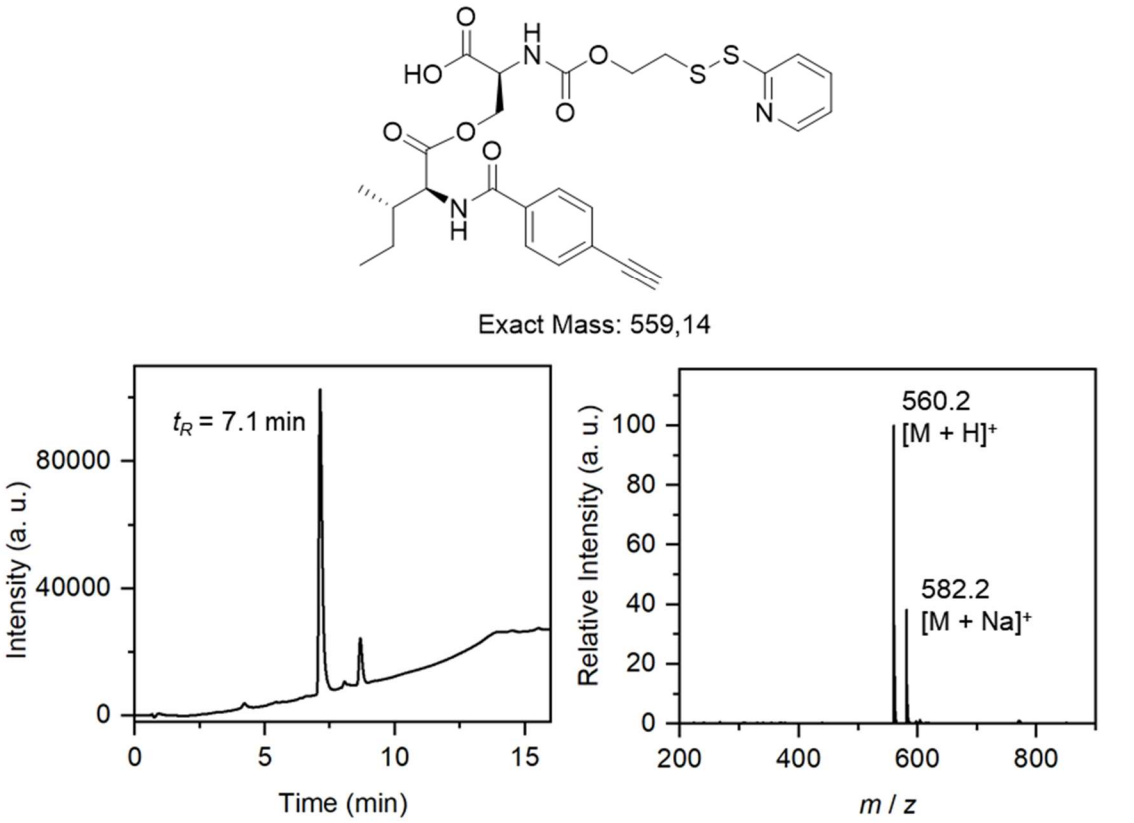

Figure 48: LC elugram (left, detection at 254 nm) and corresponding mass data (right) of JL06 (20B).

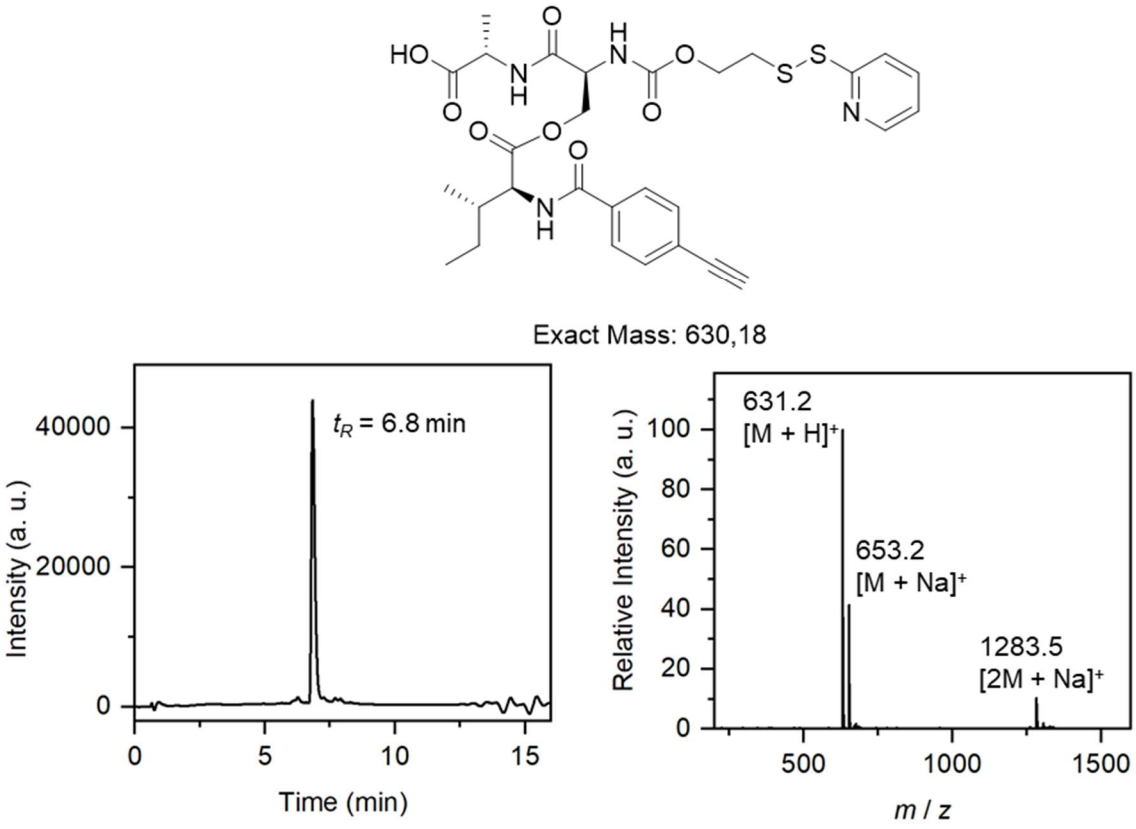

Figure 49: LC elugram (left, detection at 254 nm) and corresponding mass data (right) of JL09 (22).

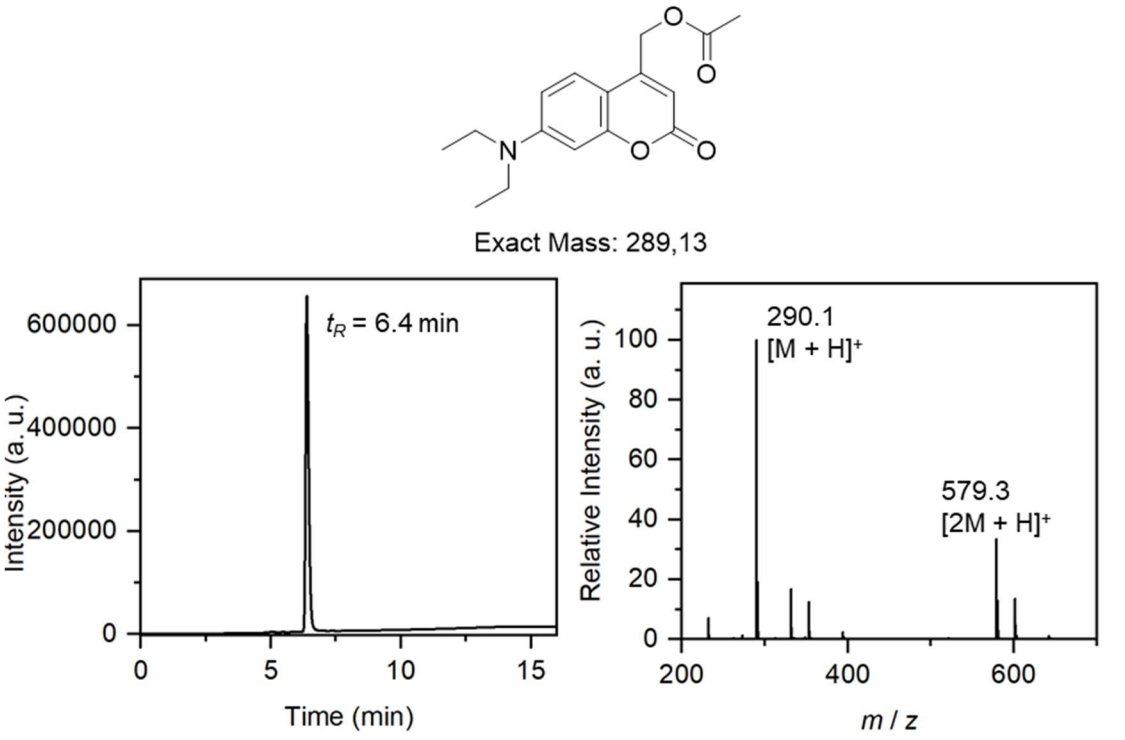

Figure 50: LC elugram (left, detection at 254 nm) and corresponding mass data (right) of JL15 (11).

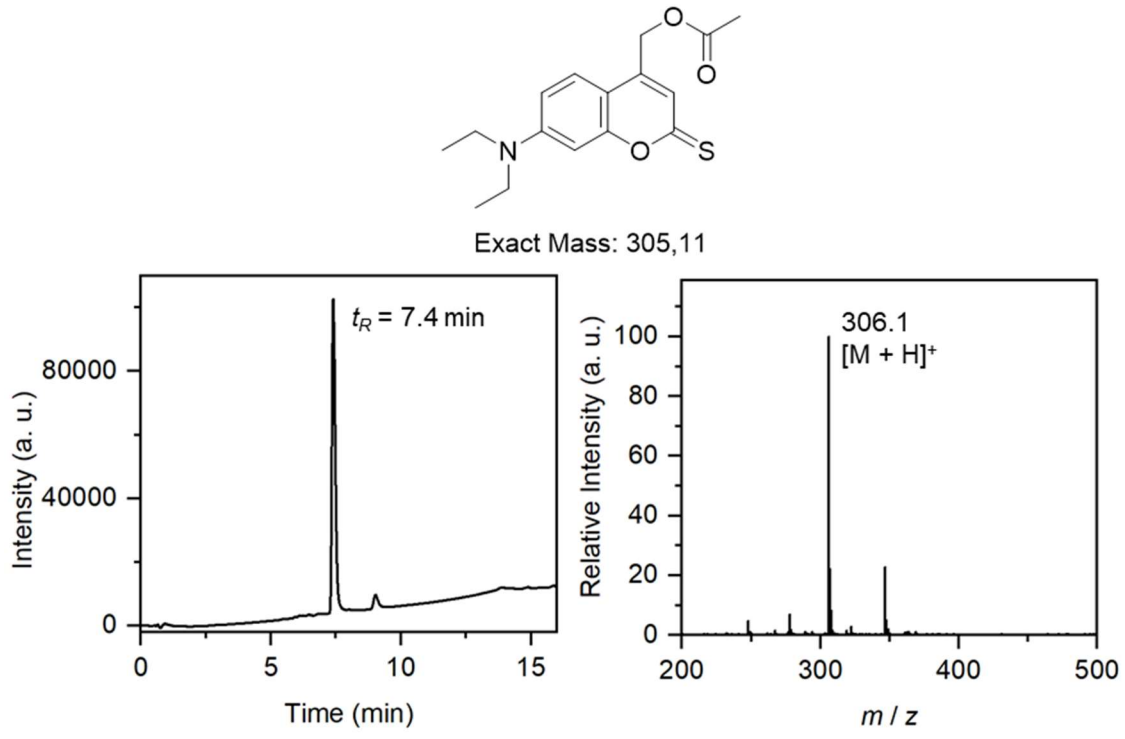

Figure 51: LC elugram (left, detection at 254 nm) and corresponding mass data (right) of JL21 (12).

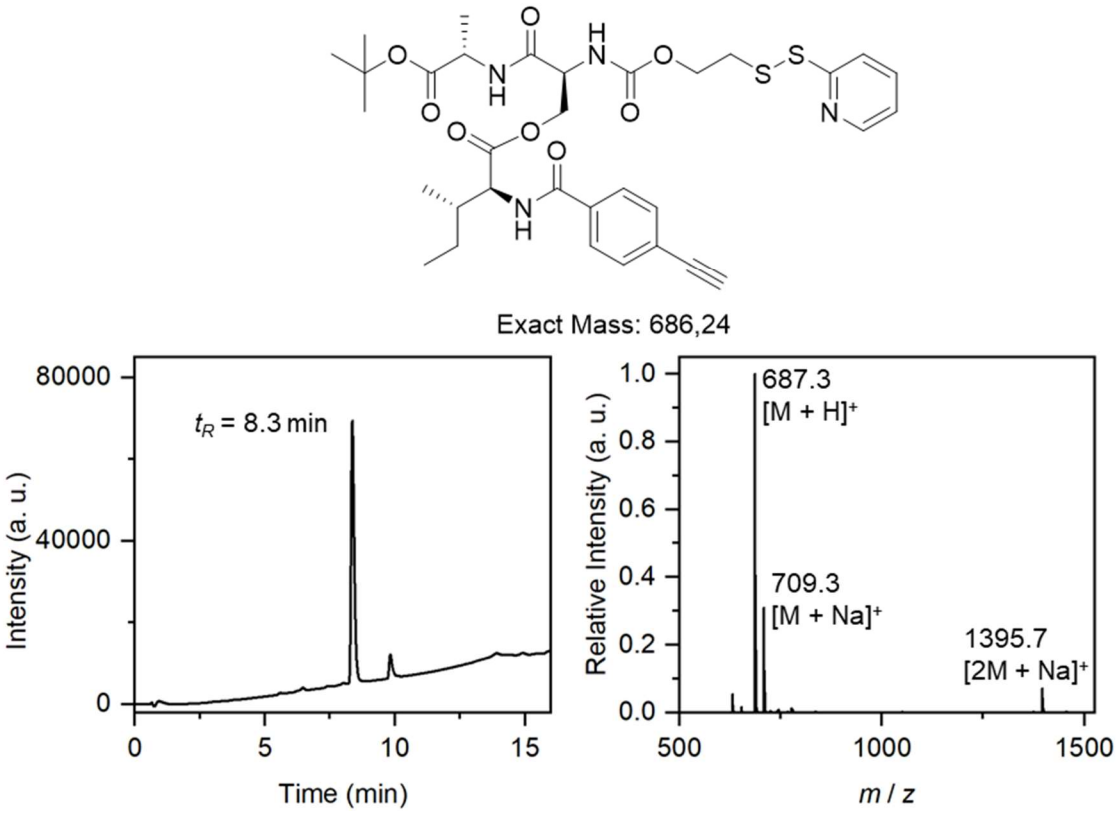

Figure 52: LC elugram (left, detection at 254 nm) and corresponding mass data (right) of JL22 (21).

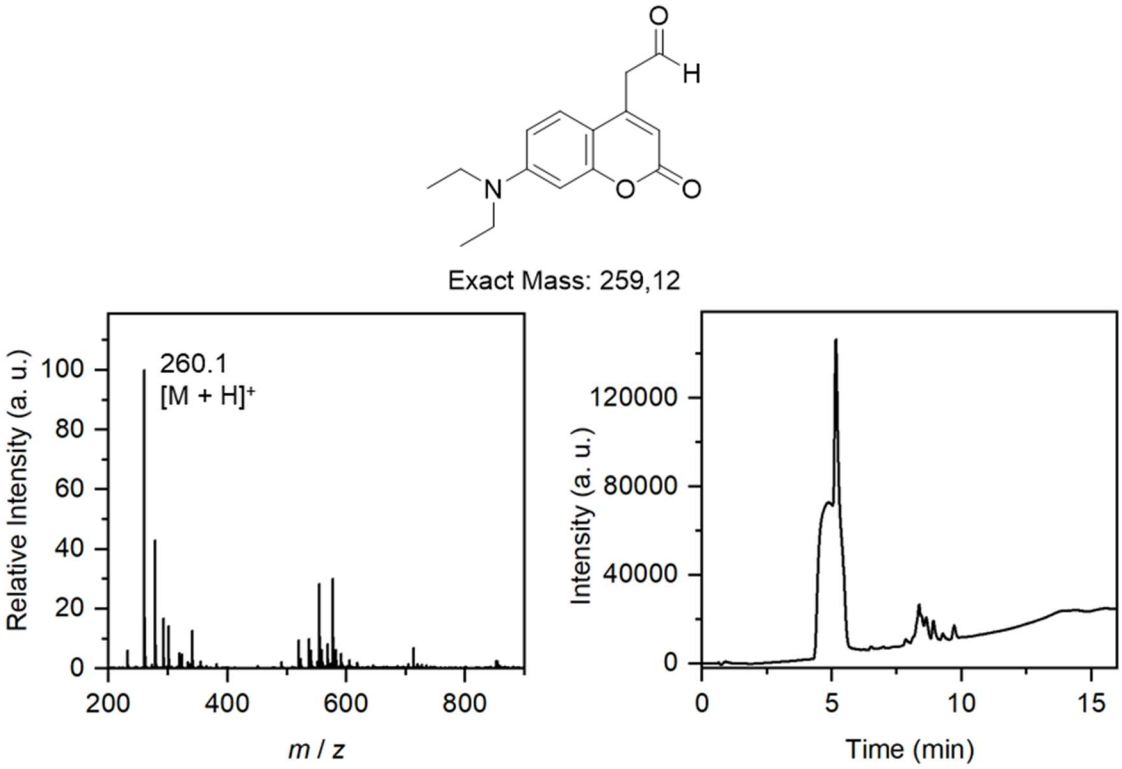

Figure 53: LC elugram (left, detection at 254 nm) and corresponding mass data (right) of JL24 (side product).

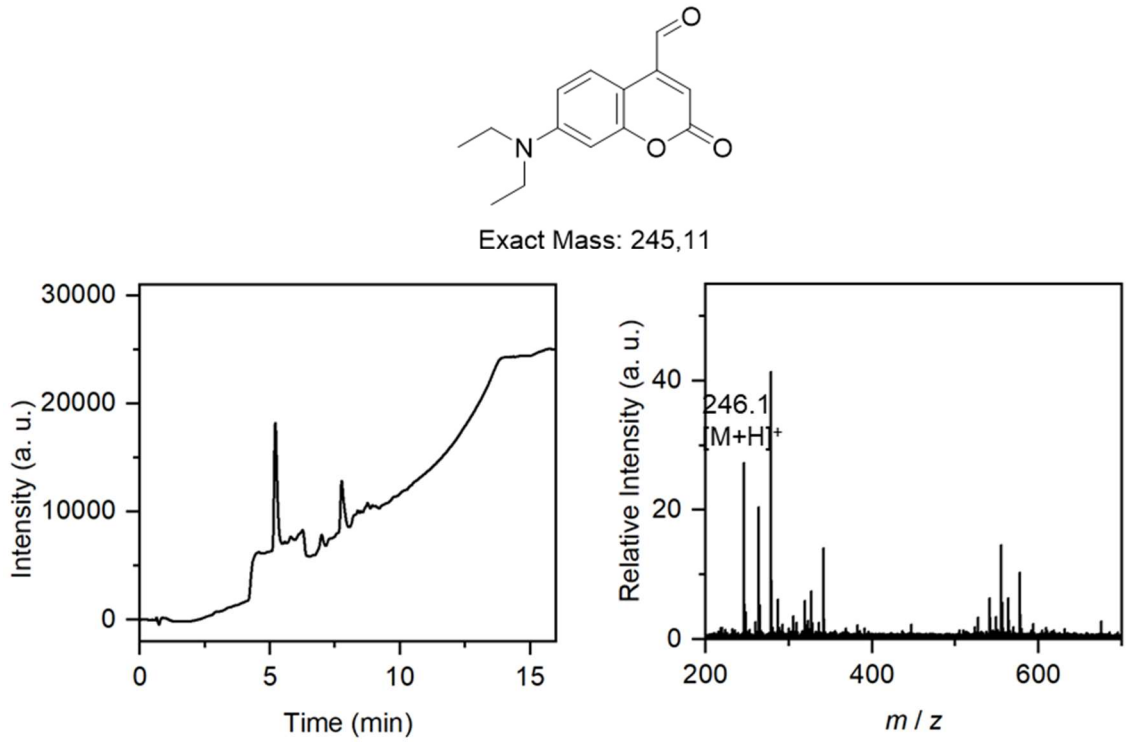

Figure 54: LC elugram (left, detection at 254 nm) and corresponding mass data (right) of JL29 (9, before workup).

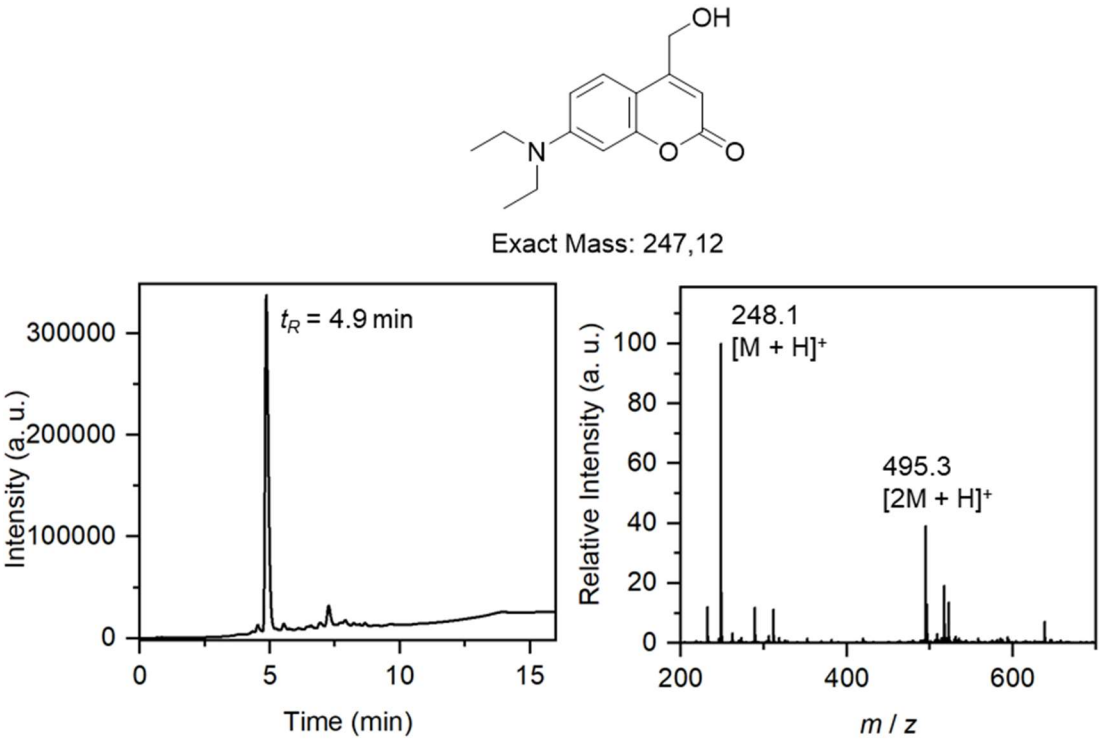

Figure 55: LC elugram (left, detection at 254 nm) and corresponding mass data (right) of JL30 (10).

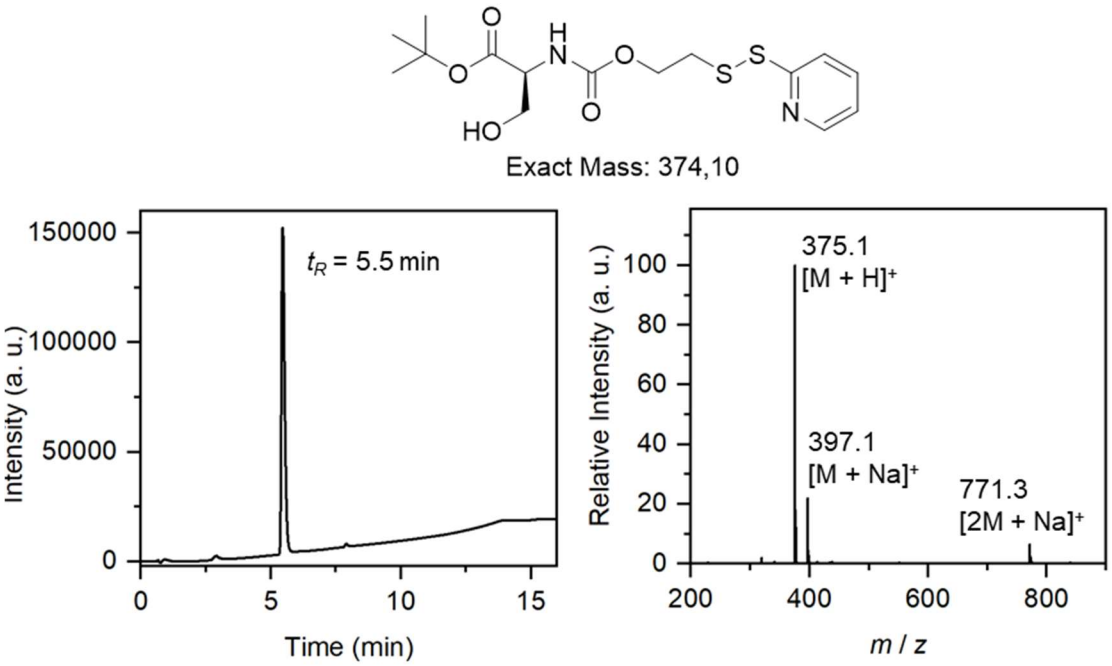

Figure 56: LC elugram (left, detection at 254 nm) and corresponding mass data (right) of JL42 (19).

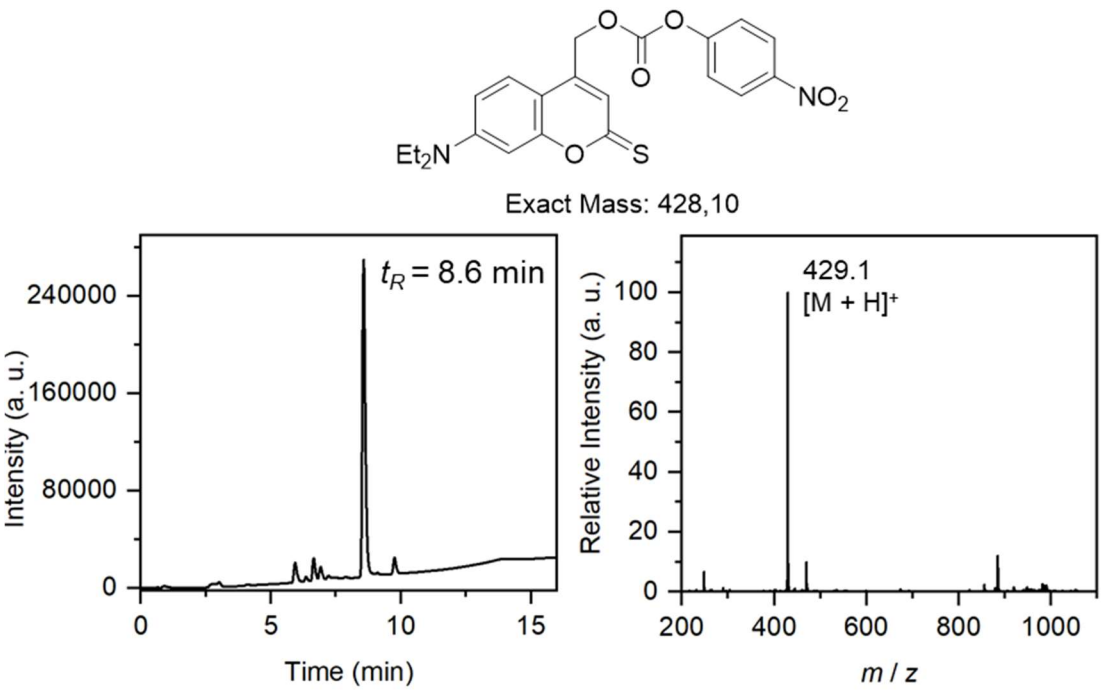

Figure 57: LC elugram (left, detection at 254 nm) and corresponding mass data (right) of JL47 (14, intermediate).

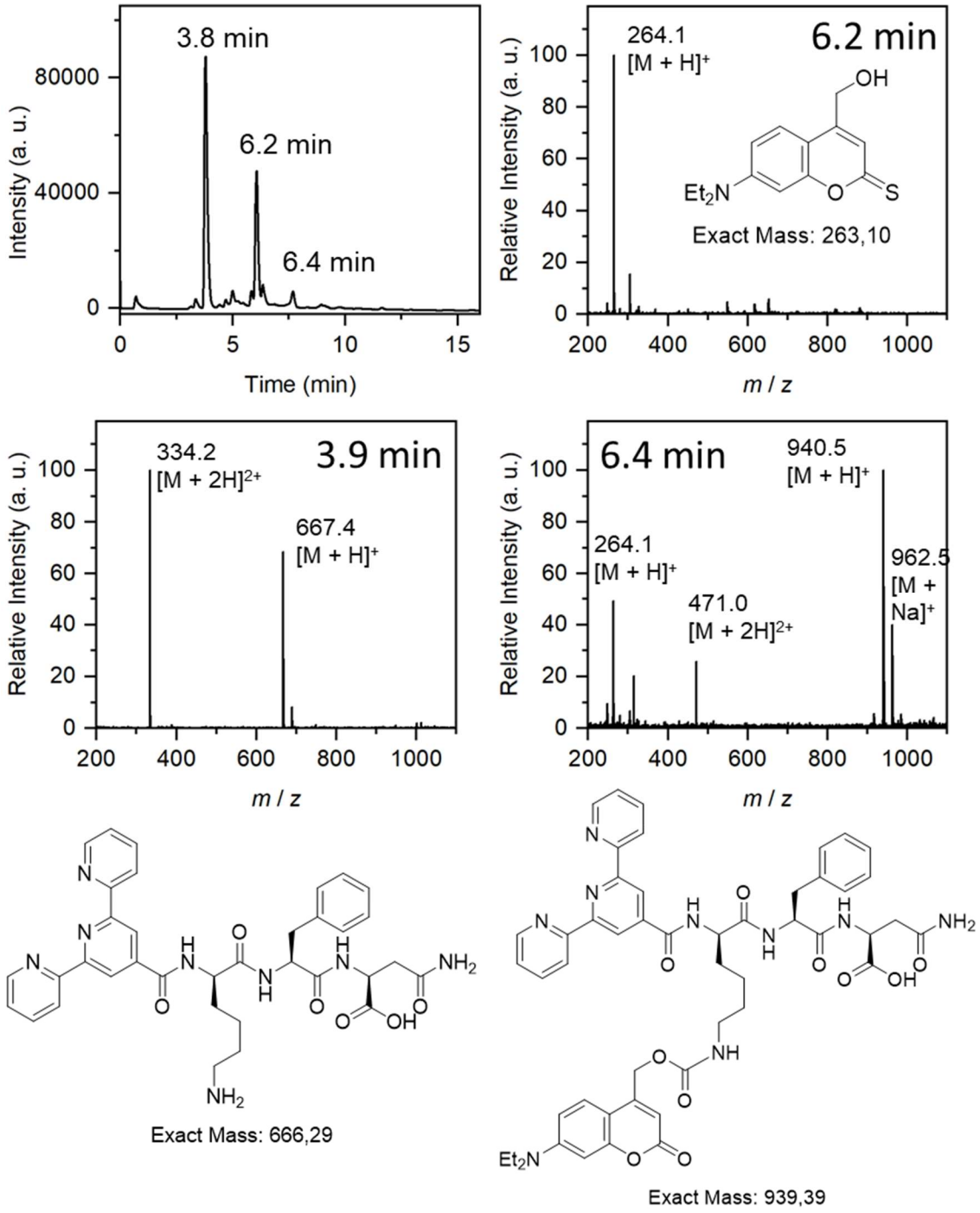

Figure 58: LCMS data of photoinduced degradation of JL47 (3). LC elugram (left, detection at 254 nm) and corresponding mass data (right) after 180 s irradiation with blue light (470 nm).

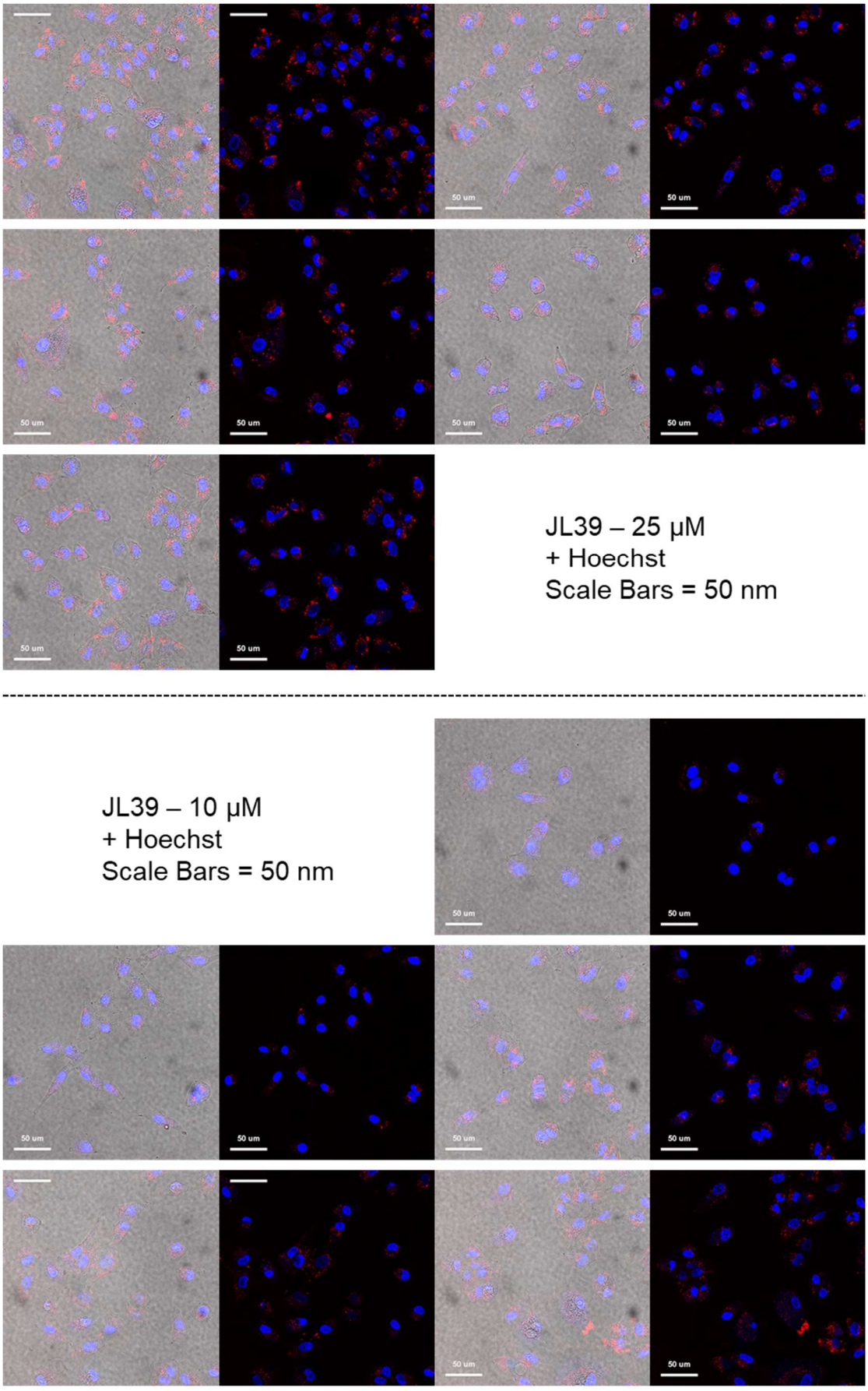

Figure 59: Confocal Images of A549 Cells treated with JL39 (26) and Hoechst Dye. Incubation for four hours, Concentrations of 10 and 25 µM, Scale bars = 50 µm.

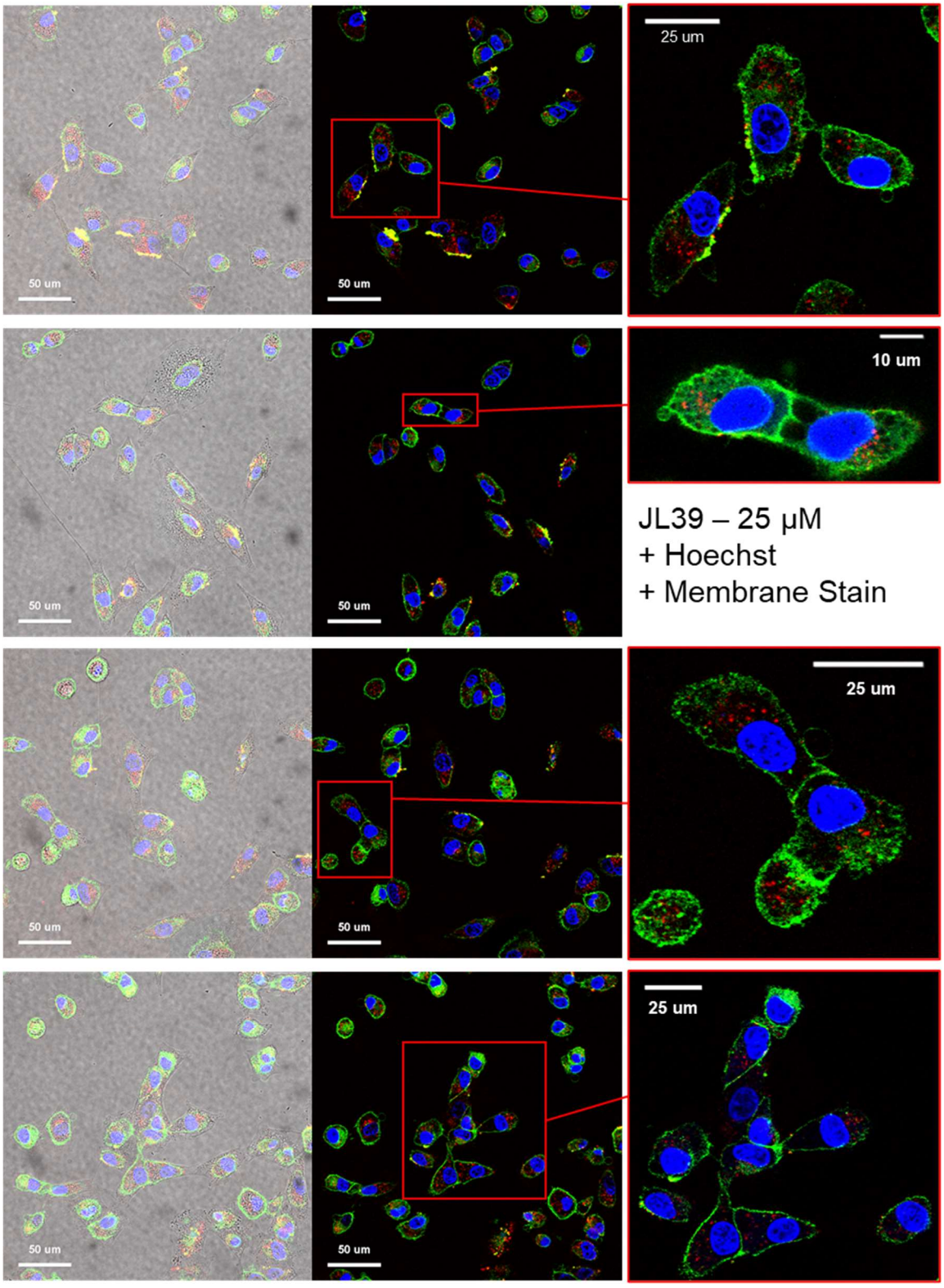

Figure 60: Confocal Images of A549 Cells treated with JL39 (26, 25 µM), Hoechst Dye and Membrane Stain. Incubation for four hours.

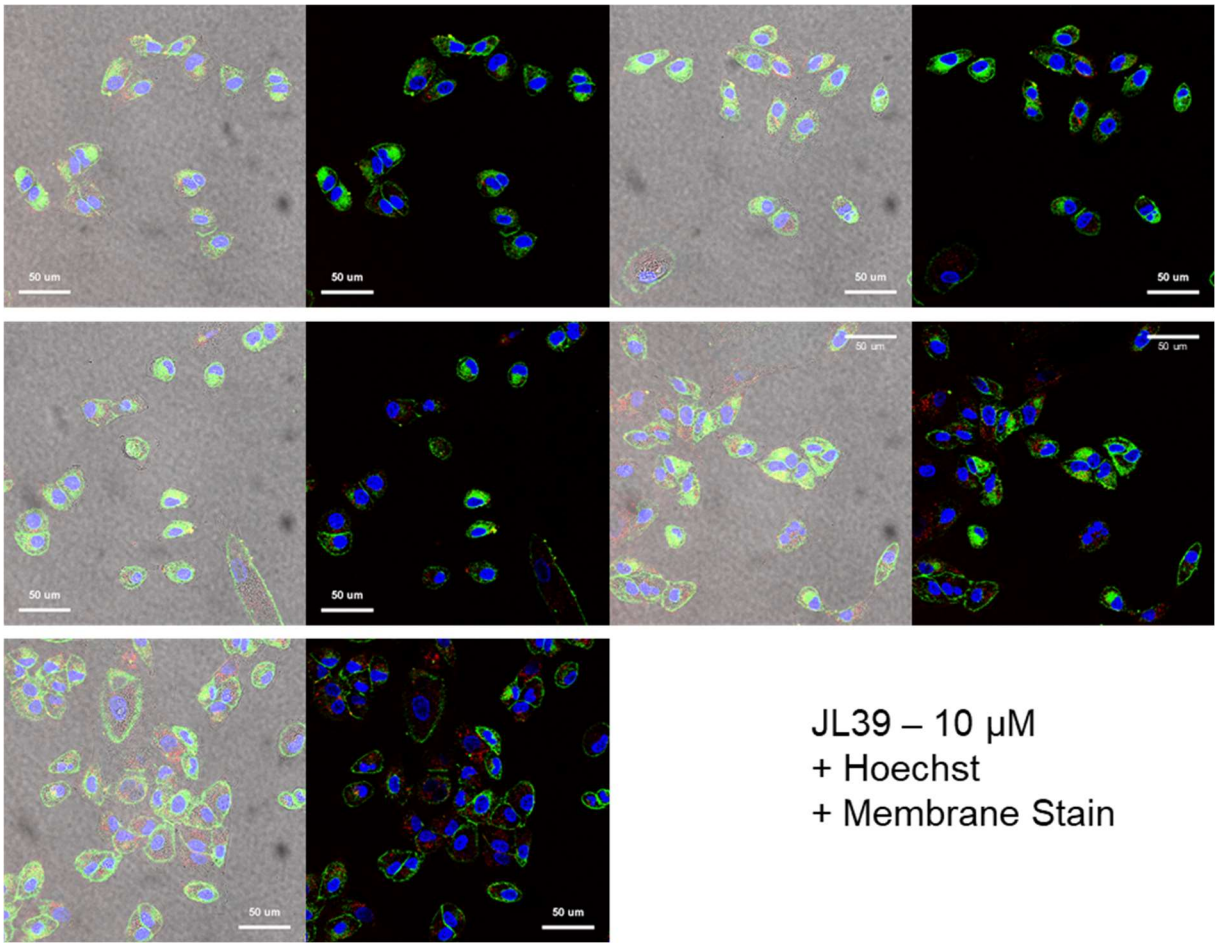

Figure 61: Confocal Images of A549 Cells treated with JL39 (26, 10 µM), Hoechst Dye and Membrane Stain. Incubation for four hours.

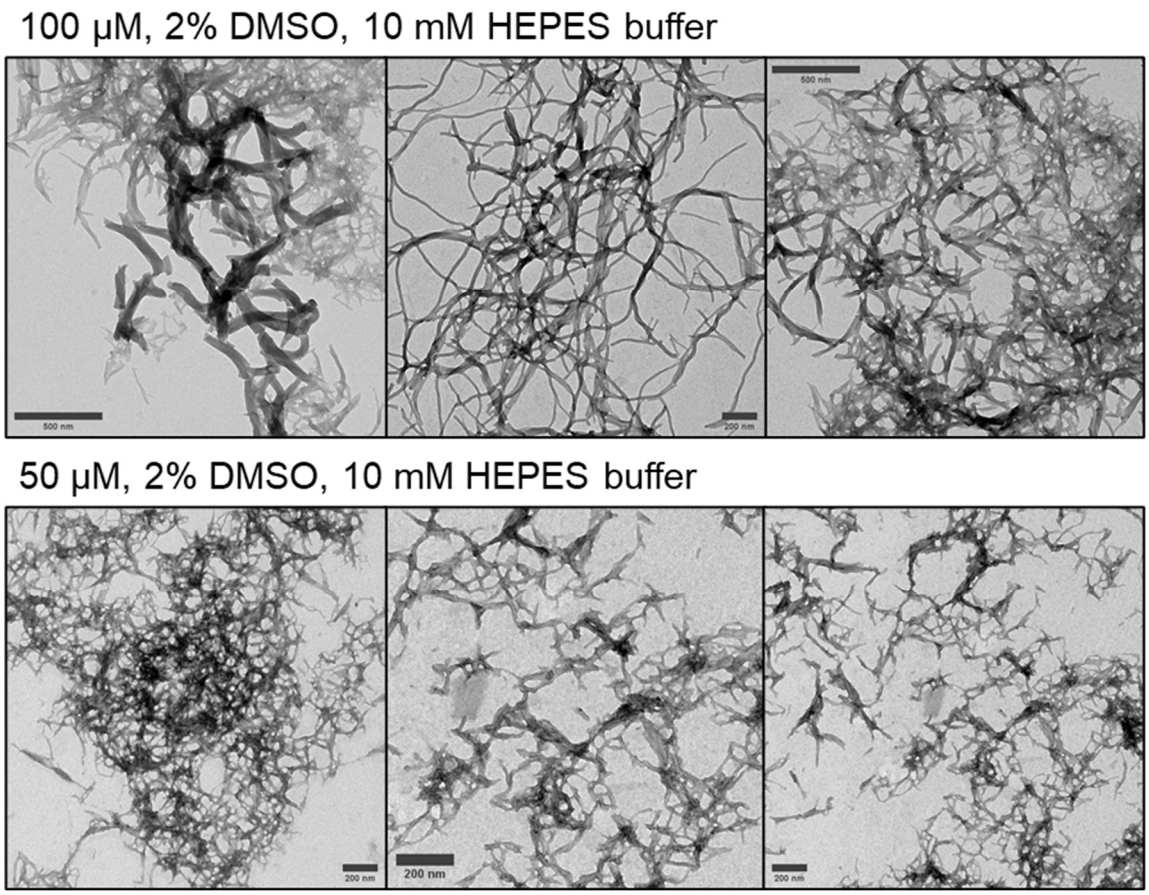

Figure 62: TEM images of JL35 (2). 2% DMSO content diluted with 10 mM HEPES buffer. Concentrations of 50 and 100 µM. Stained with Uranyl acetate.